Analysis of the heat transfer and flow in minichannel and microchannel heat sinks by single and two-phase mixture models

A thesis submitted for the degree of
Doctor of Philosophy
at the University of Leicester
by

Abdullah Masoud Ali

School of Engineering
University of Leicester
July 2022

Abstract

Analysis of the heat transfer and flow in minichannel and microchannel heat sinks by single and two-phase mixture models

Abdullah Masoud Ali

The continuous power increase and miniaturization of modern electronics requires increasingly effective thermal management systems. The thermo-hydraulic performance is investigated by a conjugate heat transfer and computational fluid dynamics model to investigate the optimum geometry and coolant composition in various microchannel heat sinks to enhance cooling. Firstly, a single-phase laminar nanofluid flow in microchannel heat sinks with a straight or twisted tape has been investigated. Swirl flow with the highest nanoparticle volume fraction was found to provide the lowest thermal resistance and contact temperature. Secondly, hydro-thermal performance-enhancing tape inserts were numerically tested featuring (i) radial gaps between the tape and the tube, (ii) tape twist with axial pitch distances of 0, L/2, or L/4, (iii) zero, one, or two 90-degree angular steps between consecutive tape segments, (iv) alternating clockwise and anti-clockwise consecutive twisted tape segments, and combinations of these features. The radial gaps produced both a hydraulic and thermal performance loss. All tape twist, angular steps, four L/4 alternating pitch consecutive helical tape and twist direction reversal combinations produced better thermal performance gains to hydraulic loss trade-offs than the baseline microchannel configuration with no tape. Thirdly, rectangular, twisted and zig-zag fins were inserted into a plain rectangular duct to enhance the cooling. The combinations of zig-zag fins and 3% Al_2O_3 nanofluid provided the best thermal performance. Finally, further research addressed and solved the inconsistent implementation of the two-phase mixture model for nanofluids in a minichannel heat sink to improve the heat prediction performance with respect to a single-phase approach, using appropriate physical modelling assumptions. By varying the volume fraction α_{nf} of the second phase between 2% and 50%, the two-phase mixture model predicted heat transfer coefficient, pressure drop, and second law efficiency values converging to the single-phase model ones at increasing α_{nf}.

Acknowledgements

Table of Contents

vi

Nomenclature

Symbols

A	Cross-sectional area	m^2
Cp	Constant pressure specific heat capacity	J/kg
D_h	Hydraulic diameter	m
$\dot{E}_x$	Exergy expenditure rate	W
$\dot{E}_{xd}$	Exergy destruction rate	W
f	Friction factor	
g	Gravity acceleration	m/s^2
h	Convection heat transfer coefficient	$W/m^2.K$
k	Thermal conductivity	W/m.K
L	Channel length	m
Nu	Nusselt number	
Nu_x	Local Nusselt number	
p	Pressure	Pa
Pp	Pumping power	W
P	Twisted tape pitch	
$\dot{q}$	Heat flux	W/m^2
$\dot{Q}$	Heat transfer rate	W
R	Total thermal resistance	W/K
Re	Reynolds number	
T	Temperature	K
u	Fluid velocity	m/s
V	Volume flow rate	m^3/s

Greek symbols

β	Velocity/temperature gradient field synergy angle	degrees
Δp	Pressure drop	Pa
η_{II}	Second law thermodynamic efficiency	
θ	Velocity/pressure gradient field synergy angle	degrees
μ	Viscosity	kg/m-s

ρ	Density	kg/m^3
ϕ	Volume fraction of the nanoparticles	
Φ	Second phase nanoparticle volume fraction	
ψ	Exergy flow	J/kg

Subscripts

bf	base fluid
f	fluid
in	inlet
m	mixture
nf	nanofluid
np	nanoparticles
out	outlet
s	solid
w	bottom wall heated surfaces

Abbreviations

2AD	two helices in alternating directions
2SD	two helices in the same direction
4AD	four helices in alternating directions
4SD	four helices in the same direction
G	tape with a gap
N	no tape
NG	tape without a gap
ST	straight tape
TT	twisted tape

Chapter 1: Introduction

1.1 Background

The thermal management of electronic devices is a significant challenge in producing efficient, high-powered energy systems (Korasikha et al., 2021). Effective cooling to decrease the heat flux from the electronic components is a serious concern for thermal engineers as the modern microelectronics industry has developed high power density devices that require an appropriate thermal management (Sadique et al., 2022). Numerous electronic components have recently produced more significant heat fluxes (Tullius et al., 2011). Miniaturisation has a visible effect on heat exchanger technology, by creating heat exchangers that are both efficient and compact (Sabbaghzadeh and Ebrahimi, 2007). It should be noted that traditional air cooling methods and ordinary fluids struggle to cope with the high heat flux produced by high power electronic chips (Tullius et al., 2011). Finned metal heat sinks cooled by a fan-drive airflow in open computer casings have served well the computer industry over many years but the heat flux from high power chips raises the base contact temperature of these heat sinks, creating a concern for the temperature-limited chips. Liquid-based computer chip heat sinks are increasingly popular in number-chrunching applications, such as high performance computing clusters or gaming computers. They typically consist of a small cross-flow heat exchanger on the chip top and a separate, larger fan-assisted liquid cooling unit, venting out of the computer casing. A small pump recirculates the liquid coolant between these two units. The unit in direct contact with the computer chip is referred to as a minichannel heat sink, or as a microchannel heat sink, depending on its size. The microchannel heat sink is an extremely small and advanced heat dissipating device, which is most appropriate for the thermal management of electronic components (Lakshminarayanan and Sriraam, 2014).

Microchannel heat sink structures have been improved and modified through several methods, such as by changing the microchannel material (Hung et al., 2012), changing the cross-section and shape of the channels (Alfaryjat et al., 2014), using double layers of channels instead of a single layer (Cheng, 2007), inserting several types of fins and plates (Chai et al., 2018, Chai et al., 2019, Bahiraei et al., 2019c) and by improving the working fluid (Mohammed Adham et al., 2013). Therefore, combining new channel structures and unconventional working fluids is a sensible line of research to boost the heat transfer rate in microchannel heat sinks.

Researchers have documented that cooling systems that use liquid coolants tend to work better than those that do not include liquid coolants in electronic applications (Saidur et al., 2011, Arani et al., 2017). Currently, conventional fluids such as water are popular coolants. Their low thermal conductivity compared to metals is a disadvantage in heat transfer applications (Sharma et al., 2013). Hence, developing a new generation of heat transfer fluids in numerous industrial applications is essential to boost the heat transfer performance. For this reason, several researchers have sought to improve the thermal properties of liquid coolants. These researchers recommend the addition of solid nanoparticles to ordinary fluids, such as engine oils, water and ethylene glycol to create a suspension of nanoparticles, which is commonly referred to as a nanofluid, resulting in improved thermal properties (Saini et al., 2016).

The number of numerical studies related to nanofluids has increased considerably in the last two decades (Seyf and Keshavarz, 2011, Rahimi-Gorji et al., 2015, Yan et al., 2019). Nanofluids can be modelled either with a single-phase model or with multiphase models (Sidik et al., 2016, Akbari et al., 2011, Ambreen and Kim, 2017, Kumar and Sarkar, 2019). In the single-phase approach, the suspension of nanoparticles in a base fluid is assumed to be homogeneous and thermal equilibrium is assumed between the nanoparticles and the base fluid. By this approach, the nanofluid is replaced by a single fluid of equivalent thermophysical properties to the ones of the suspension, determined from an experiment or by a physical model (Sidik et al., 2016). The single-phase model is simpler than other models and requires less time to run a numerical simulation.

Conversely, in the two-phase approach, nanoparticles and their base flow are divided into two separate phases. These phases move and interact according to a volume of fluid model (VOF), a mixture model, an Eulerian model, or a Discrete Phase model. Each model is distinct in the way it manages the mass, momentum, and energy conservation of each phase. The VOF model is designed to solve a single set of momentum equations for two or more immiscible fluids and tracks the volume fraction all over the domain by solving a continuity equation for the secondary phases (Moraveji and Ardehali, 2013). The mixture model solves one momentum and one energy equation for the mixture. This model determines the slip velocities of each phase algebraically and volume fraction of each phase (Ambreen et al., 2021). The Eulerian model solves separate continuity, momentum, and energy equations for each phase. The volume concentration of each phase is solved by integrating its volume concentration transport equation through the domain

and by imposing that the volume fractions summation is equal to unity (Akbari et al., 2011). In the Discrete phase model (DPM), the base fluid phase is treated as a continuum via solving the Navier-Stokes equations, whereas the nanoparticles that make up the dispersed phase are traced by the Lagrangian approach (Ambreen and Kim, 2017). The dispersed phase can exchange momentum, mass, and energy with the fluid phase. Notwithstanding these studies, significant knowledge gaps remain, which are exposed by the review of the literature within this thesis. For instance, many researchers reported that multiphase mixture models provided over-estimations of the heat transfer compared with single-phase models.

1.2 Classification of microchannels

Liquid cooled heat sinks typically feature a base that is in contact with a heat source and one or more channels through which the coolant flows, to remove the heat. Channels of different sizes are used, depending on the application, and naming conventions for channels of different size range are reported in Table 1.1, taken from Mehendale et al. (2000) and Kandlikar and Grande (2003). The channel categories are based on the channel hydraulic diameter D_h. This study adopts the naming convention by Mehendale et al. (2000).

Table 1.1 Classification of microchannels.

Mehendale et al. (2000)		Kandlikar and Grande (2003)	
Conventional channels	$D_h < 43$ mm	Conventional channels	$D_h < 46$ mm
Minichannels	$200\ \mu m < D_h < 3$ mm	Compact passages	1 mm $< D_h < 6$ mm
Microchannels	$10\ \mu m < D_h < 200\ \mu m$	Meso-channel	0.1 mm $< D_h < 1$ mm
Transitional channels	$0.1\ \mu m < D_h < 10\ \mu m$	Microchannels	$1\ \mu m < D_h < 100\ \mu m$

1.3 Research motivation

The microchannel heat sink is an effective solution for decreasing the contact temperature in a computer chip heat sink. Parallel microchannels are generally applied in micro heat exchangers because of their large contact surfaces with the liquid and the availability of a large mass of fluid to transfer heat away from the heat source. A geometrical structure with flow blockage, such as channels with finned internal walls, has a vital role in the flow distribution in the microchannels, which may well affect the heat and mass transfer efficiency. However, these heat exchangers typically exhibit a higher pressure drop as cost for their better thermal performance. Many studies address the design optimisation of the microchannel heat sink. Twisted tapes have been employed in large

channels with the aim of improving the overall thermal performance by means of changing axial flow into swirl flow. Thus, twisted tapes have inspired the current research to undertake additional studies on the thermo-hydraulic effects of inserting a single twisted tape in a circular microchannel heat sink running either water or nanofluid coolants. A computational investigation is presented on the thermal performance of a forced-convection circular microchannel heat sink with either no tape (MC-NT), a straight tape (MC-ST) or a twisted tape (MC-TT), cooled by an Al_2O_3 nanofluid with different volume fraction.

Twisted tape designers use various techniques in which the performance is significantly affected by the parametrisation and optimisation stages in the geometry design process. These include investigating an uninterrupted tape running through the entire channel length, interrupting the tape with axial gaps, adding tape pitch angle steps along its length, alternating between a clockwise and an anti-clockwise tape pitch along its length, varying the tape pitch, adding fringe cuts to the tape, using a twisted tape with centre wings on alternate axes, and using wire nails in the twisted tapes. Therefore, further research on hydro-thermal performance-enhancing tape inserts is pursued by numerically testing (i) radial gaps between the tape and the tube, (ii) tape twist with axial pitch distances of 0, L/2 or L/4, (iii) zero, one or two 90-degree angular steps between consecutive tape segments, (iv) alternating clockwise and anti-clockwise consecutive twisted tape segments, as well as combinations of these features to enhance a circular microchannel heat sink performance.

The performance of microchannel heat sinks with non-circular cross-sections, primarily rectangular microchannel heat sinks, has been studied extensively. Rectangular cross-sections in microchannel heat sinks are easier to fabricate and have larger wetted surfaces than circular cross-sections. Different researchers have used different approaches, such as fins and various coolants to analyse and optimise the geometrical parameter combinations that have resulted in the best performances for microchannel heat sinks. The combinations of rectangular cross-sections, fins and nanofluid encouraged further research to be conducted on the thermal and hydraulic performance of a forced convection microchannel heat sink that has no fins (MC-N) or has a rectangular (MC-R), twisted (MC-T) or zigzag (MC-Z) fin, cooled by an Al_2O_3 nanofluid with a volume fraction range 0 to 3%.

4

The creation and evaluation of engineering systems require an accurate prediction of their heat transfer and hydraulic characteristics. The thermal and hydraulic characteristics of heat exchangers using nanofluid can be numerically investigated by way of single-phase or two-phase flow approaches. Various authors documented over-estimations of the heat transfer with the two-phase mixture model approach in contrast to the single-phase approach (Mojarrad et al., 2013). Therefore, further research is carried out to review the implementation of the two-phase mixture model to a minichannel heat sink in order to improve the heat prediction performance with respect to a single-phase approach, using appropriate physical modelling assumptions. This may significantly contribute to the scientific community knowledge base by identifying how the two-phase mixture model can be used confidently and effectively to explore physical flows.

1.4 Aims and objectives

This research aims to investigate the optimum geometry and coolant composition in various microchannel heat sinks to enhance cooling. Several twisted tapes and fins were carefully designed and inserted in the virtual microchannels to produce a range of channel geometries and, at the same time, produce significant changes in the through flow pattern. This research further aims to review the implementation of the two-phase mixture model to simulate the nanofluid, towards obtaining consistent and reliable heat transfer predictions from the minichannel two-phase mixture model. Towards these aims, the following objectives are pursued:

- To enhance the heat transfer performance in a circular microchannel heat sink using twisted tapes and nanofluid.
- To enhance the heat transfer performance in a circular microchannel heat sink using several modified twisted tapes.
- To improve the heat transfer performance in a rectangular microchannel heat sink using various fins and nanofluid.
- To define and use a physically consistent implementation of the two-phase mixture model for the heat transfer of nanofluids in minichannel heat sinks.

1.5 Research novelty

The main contributions from the research can be summarised as follows:

1. The thermo-hydraulic effects of inserting a single twisted tape in a circular microchannel heat sink running either water or nanofluid coolants were investigated. It is shown that swirl flow and nanofluid features can be combined to decrease the microchannel thermal resistance and reduce the contact temperature at the base of the heat sink, for a heat flux input representative of a microprocessor core.

2. The hydro-thermal performance-enhancing tape inserts were numerically tested featuring (i) radial gaps between the tape and the tube, (ii) tape twist with axial pitch distances of 0, L/2 or L/4, (iii) zero, one or two 90-degree angular steps between consecutive tape segments, (iv) alternating clockwise and anti-clockwise consecutive twisted tape segments, and combinations of these features.

3. The thermo-hydraulic effects of a forced convection microchannel heat sink that has no fins or has a rectangular, twisted, or zigzag fin, cooled by either water or nanofluid were investigated. The intent is to combine the increased surface area and the vertical motion due to the fins with the increased thermal conductivity of the working fluid, leading to a decreased thermal resistance of the microchannel and a decreased contact temperature of the heat sink base.

4. Past researchers reported over-predictions of heat transfer rate when using the two-phase mixture model. This research addresses and solves this key shortcoming, enabling reliable and physically sound predictions of microchannel nanoflows, using the two-phase mixture model. This method has provided the protocol for using the two-phase mixture model within appropriate volume fraction bounds. This higher fidelity method, unconstrained by the uniform particle distribution assumption of the single-phase approach, can now be used with confidence to explore more complex minichannel geometries and resolve localised concentrations of nanoparticles, exploring their effect on the thermal and mass transport characteristics.

1.6 Thesis outline

This thesis is organised into seven chapters.

Chapter 1: Introduces the background, the classification of microchannels, the motivation, the main aims, the objectives of this work and the research novelty.

Chapter 2: Methodology

This chapter presents the governing equations, nanofluid model, boundary conditions, data reduction, second law efficiency, and field synergy analysis.

Chapter 3: Thermo-hydraulic performance of a circular microchannel heat sink using swirl flow and nanofluid.

This journal paper demonstrates the effects of the first attempt at applying a twisted tape to a circular microchannel heat sink running Al_2O_3 nanofluid coolant. This technology is expected to potentially reduce the contact temperature of microprocessors, thereby improving their longevity or enabling higher power density microprocessor designs by maintaining the chips within acceptable operational temperature limits.

Chapter 4: Numerical analysis on the thermal performance of microchannel heat sinks with Al_2O_3 nanofluid and various fins.

This journal paper is the first paper showing the combined effect of three different tape design parameters (twist axial pitch, tape segmentation, and twist direction) on the thermal and hydrodynamic performance of a microchannel heat sink.

Chapter 5: The thermo-hydraulic performance of a rectangular microchannel heat sin with fins and a nanofluid.

This journal paper is the first paper to present the combined effect of three different fin designs (rectangular, twisted, and zig-zag) and of a nanofluid coolant on the thermal and hydrodynamic performance of a microchannel heat sink.

Chapter 6: A novel physically consistent application of the mixture model for modelling nanofluid conjugate heat transfer in minichannel heat sinks.

Past researchers reported over-predictions of heat transfer rate when using the two-phase mixture model. This paper investigates, addresses, and solves this key shortcoming, enabling reliable and physically sound predictions of microchannel nanoflows, using the

two-phase mixture model. This method is unconstrained by the uniform particle distribution assumption of the single-phase approach.

Chapter 7: Conclusions and directions for further work.

1.7 List of publications

1. **Ali, A.M**., Rona, A., Kadhim, H.T., Angelino, M. and Gao, S., 2021. Thermo-hydraulic performance of a circular microchannel heat sink using swirl flow and nanofluid. Applied Thermal Engineering, 191, p.116817. https://doi.org/10.1016/j.applthermaleng.2021.116817.

2. **Ali, A.M**., Rona, A. and Angelino, M., 2022. Numerical investigation of various twisted tapes enhancing a circular microchannel heat sink performance. International Journal of Heat and Fluid Flow, 98, p.109065. https://doi.org/10.1016/j.ijheatfluidflow.2022.109065.

3. **Ali, A.M**., Angelino, M. and Rona, A., 2021. Numerical analysis on the thermal performance of microchannel heat sinks with Al_2O_3 nanofluid and various fins. Applied Thermal Engineering, p.117458. https://doi.org/10.1016/j.applthermaleng.2021.117458.

4. **Ali, A. M**., Angelino, M. and Rona, A. 2022. Physically consistent implementation of the mixture model for modelling nanofluid conjugate heat transfer in minichannel heat sinks. applied sciences, 12, 7011. https://doi.org/10.3390/app12147011.

1.8 Authorship contribution

Abdullah Masoud Ali: Conceptualization, Data curation, Formal analysis, Methodology, Software, Validation, Visualization, Writing – original draft.

Chapter 2: Methodology

2.1 Mathematical formulation

A numerical analysis of the laminar nanofluid forced convection in the microchannel and minichannel heat sinks is performed. A constant heat flux is applied at the bottom plate of the heat sink. The conjugate heat transfer through the heat sink walls and through the coolant flow is evaluated numerically by means of coupling the Laplace equation.

$$\nabla^2 T_s = 0 \qquad (2.1)$$

which models the distribution of temperature T_s through the solid walls, with the time-averaged Navier-Stokes equations, which model the coolant (Ali et al., 2021b). The coolant is represented as a Newtonian fluid using either a single-phase approach or the two-phase mixture model approach.

2.1.1 Single-phase approach

By the single-phase approach, the nanofluid is modelled as a homogeneous Newtonian fluid. The continuity, momentum and energy equations are solved numerically in line with the assumptions shown below:

1. The flow is three-dimensional, laminar, Newtonian, steady, and incompressible.
2. The flow is steady, temperature dependent, and the flow velocity is uniform at the inlet.
3. The heat sink radiative heat transfer is negligible compared to that by conduction and convection.

The fluid flow governing equations are: (Ambreen and Kim, 2017):

$$\nabla \cdot (\rho_{nf} \vec{u}_{nf}) = 0 \qquad (2.2)$$

$$\nabla \cdot (\rho_{nf} \vec{u}_i \vec{u}_i) = -\nabla p_{nf} + \mu_{nf} \nabla^2 \vec{u}_{nf} + \rho_{nf} \vec{g} \qquad (2.3)$$

$$\rho_{nf} \vec{u}_{nf} \cdot \nabla T_f = \nabla \cdot (k_{nf} \nabla T_f) \qquad (2.4)$$

where ρ_{nf}, μ_{nf}, k_{nf}, $\vec{u}_{nf}$, p_{nf}, $\vec{g}$, and T_{nf} are the nanofluid density, nanofluid molecular viscosity, nanofluid thermal conductivity, the velocity vector, the absolute pressure, the gravitational acceleration in the negative x_2 direction, and the absolute temperature of the nanofluid, respectively.

the flow governing equations reduce to the incompressible scalar transport equations in Cartesian orthogonal coordinates x_i (Cheng, 2007).

$$\frac{\partial \phi}{\partial t} + \frac{\partial}{\partial x_j}\left(\rho_{nf} u_i \, \phi\right) = \frac{\partial}{\partial x_j}\left(\Gamma \frac{\partial \phi}{\partial x_j}\right) + \text{S} \tag{2.5}$$

where $\phi = \left(1, u_i, T_{nf}\right)^T$, $\Gamma = \left(0, \mu_{nf}, \mu_{nf}/Pr_{nf}\right)^T$, and $S = \left[0, -\frac{\partial p_{nf}}{\partial x_i}, 0\right]^T$ are the vectors of transported flow properties, of the diffusion terms, and of the source terms. $Pr_{nf} = \mu_{nf} Cp_{nf}/k_{nf}$ is the Prandtl number. u_i, p_{nf} are the velocity vector and the absolute pressure. Superscript T denotes the vector transpose.

2.1.2 Multiphase mixture model

This model represents the flow by two phases, the first phase is water, and the second phase is a homogeneous Newtonian fluid, the properties of which are equivalent to the ones of a suspension of nanoparticles in water. In this second phase, the coupling between the motion of the nanoparticle and the fluid motion surrounding them is assumed to be strong, so that the nanoparticles move with their neighboring fluid in the second phase. Each phase has its own velocity vector field. The first and second phases are immiscible and the second phase is modelled as spherical bubbles dispersed in the first phase continuum, in a bubbly flow regime (Manjrekar and Dudukovic, 2019). The portion of space occupied by the second phase bubbles at any spatial location is defined by the volume fraction. The first phase moves the second phase by way of a drag force and the second phase affects the first phase because of a reduction in the first mean momentum. The coolant flow is modelled as a two-phase mixture based on the following assumptions:

1. The flow is steady, laminar, incompressible, as well as three-dimensional.

2. The second phase comprises spherical bubbles of prescribed uniform size (Silva et al., 2015).
3. All of the phases share a single pressure (Sidik et al., 2017).
4. The working fluid thermal properties are volume fraction dependent (Sidik et al., 2017).
5. Gravitational effects are modelled, and radiative heat transfer is disregarded (ANSYS, 2017).
6. The volume fraction of nanoparticles in the mixture is sufficiently low so that collision and heat conduction by contact between particles are negligible (Silva et al., 2015).
7. The diameter of the nanoparticles is smaller than the diameter of the bubbles so that the nanoparticles are uniformly dispersed in the second phase (Mirmasoumi

10

and Behzadmehr, 2008), so that the volume fraction Φ of the nanoparticles in the second phase has one average value and that the spherical shape of the bubbles is unaffected by the presence of the nanoparticles in it.

8. The diameter of the bubbles is smaller than the minichannel hydraulic diameter so that a local equilibrium is established over short spatial length scales (Silva et al., 2015).

The continuity equation in relation to the mixture is:

$$\nabla \cdot (\rho_m \vec{u}_m) = 0 \tag{2.6}$$

where $\vec{u}_m$ is the mass-averaged mixture velocity

$$\vec{u}_m = \frac{\alpha_{bf} \rho_{bf} \vec{u}_{bf} + \alpha_{nf} \rho_{nf} \vec{u}_{nf}}{\rho_m} \tag{2.7}$$

and ρ_m is the mixture density

$$\rho_m = \alpha_{bf} \rho_{bf} + \alpha_{nf} \rho_{nf} \tag{2.8}$$

The momentum equation for the mixture can be shown as:

$$\nabla \cdot (\rho_m \vec{u}_m \vec{u}_m) = -\nabla p + \mu_m \nabla^2 \vec{u}_m + \rho_m \vec{g} + \nabla \cdot (\alpha_{bf} \rho_{bf} \vec{u}_{dr,bf} \vec{u}_{dr,bf} \tag{2.9}$$
$$+ \alpha_{nf} \rho_{nf} \vec{u}_{dr,nf} \vec{u}_{dr,nf})$$

The molecular viscosity of the mixture μ_m is

$$\mu_m = \alpha_{bf} \mu_{bf} + \alpha_{nf} \mu_{nf} \tag{2.10}$$

where μ_{bf} and μ_{nf} are the molecular viscosities of the first and of the second phases, respectively.

The drift velocity of the second phase $\vec{v}_{dr,nf}$ is defined as the phase dispersion velocity relative to the mixture velocity:

$$\vec{u}_{dr,nf} = \vec{u}_{nf\,bf} - \vec{u}_m \tag{2.11}$$

$$\vec{u}_{nf\,bf} = \frac{(\rho_{nf} - \rho_m)d_{nf}^2}{18\mu_m f_{drag}} \vec{a} \tag{2.12}$$

where d_{nf} is the uniform diameter of the second phase bubbles. The drag coefficient f_D is evaluated according to Naumann and Schiller (1935) as

$$f_D = \begin{cases} 1 + 0.15 Re_{nf}^{0.687} & Re_p \leq 1000 \\ 0.0183 Re_{nf} & Re_p > 1000 \end{cases} \tag{2.13}$$

where $\vec{a}$ is the second phase bubble acceleration

$$\vec{a} = \vec{g} - (\vec{u}_m \cdot \nabla)\vec{u}_m \tag{2.14}$$

Using a length scale analysis, Buongiorno (2005) shows that the effect of gravity and of drag on nanoparticles is insignificant. Whereas nanoparticles have a size of order 1 nm, the second phase bubbles that model their presence in the two-phase mixture model have size of order 100 nm. The larger scale of these bubbles, compared with that of the nanoparticles, enables the estimation of gravitational and drag effects on the bubble motion, albeit the length scale analysis suggests these effects are small. This limits the application of this two-phase model to larger-sized bubbles, above 80 nm, as gravity and drag estimates become progressively smaller and numerically more difficult to account for in the flow force-momentum balance with smaller bubble sizes.

Due to their small size, the nanofluid particles are assumed to be in thermal equilibrium within each second phase bubble and the temperature field is assumed to be smooth across phase boundaries. This enables defining a single temperature field for the mixture that is governed by the following scalar transport equation:

$$\nabla \cdot (\alpha_{bf}\rho_{bf}Cp_{bf}\vec{u}_{bf} + \alpha_{nf}\rho_{nf}Cp_{nf}\vec{u}_{nf})T_f = \nabla \cdot (k_m \nabla T_f) \tag{2.15}$$

where T_f is the mixture temperature, Cp_{bf} is the constant pressure specific heat capacity of the first phase, Cp_{nf} is the constant pressure specific heat capacity of the second phase, and k_m is the mixture thermal conductivity

$$k_m = \alpha_{bf}k_{bf} + \alpha_{nf}k_{nf} \tag{2.16}$$

where k_{bf} is the thermal conductivity of the first phase and k_{nf} is the thermal conductivity of the second phase.

The two-phase mixture model does not track the motion of individual particles and is therefore unable to model particle agglomeration by particle surface attraction, for

instance by chemical bonding. Likewise, it is unable to model particle sedimentation, which entails the mechanical locking of particles onto one another. Still, by equation (2.14), the accelerations due to flow path curvature and due to gravity on the second phase are accounted for. This, in principles, enables the model to represent phase stratification (but not particle sedimentation), due to gravity, and phase segregation (but not particle agglomeration), due to flow path curvature, both of which are not representable by the single-phase approach.

2.2 Nanofluid model

This study uses Al_2O_3 nanoparticles suspended in water at three different volume fraction concentrations of 1%, 2% and 3%; a similar volume fraction range is used by Murali Krishna et al. (2021) in a circular micro-channel heat sink. The thermal and physical properties of water and Al_2O_3 nanoparticles are displayed in Table 2.1. These properties are used to determine the thermal properties of the equivalent single-phase fluid in the computational fluid dynamics simulation in Chapter 3: and Chapter 5:. Two alternative approaches are used to define a suspension of Al_2O_3 nanoparticles in water at the nanoparticle module fraction ϕ of 1% in Chapter 6:. In the single-phase approach, the nanofluid is simulated by one homogeneous fluid of equivalent thermal and physical properties. The two-phase approach uses water as the first phase and a homogeneous fluid of equivalent thermal and physical properties as the second phase. The new thermal and physical properties of the second phase are defined in Setup/ Materials/ Create/Edit Materials in FLUENT. In the two-phase approach, this work uses the seven combinations of second phase volume fraction α_{nf} and of second phase Al_2O_3 nanoparticle volume concentration Φ, listed in Table 2.2. Each combination provides the same 1% Al_2O_3 nanoparticle volume fraction mixture ϕ.

Table 2.1 The thermo-physical properties of water at 20°C (Rogers and Mayhew, 1995) and of nanoparticles (Saba et al., 2018).

	ρ (kg/m^3)	C_P (J/kg·K)	k (W/m·K)	μ (N·s/m^2)	Diameter of nanoparticles (nm)
Water	998.2	4183	0.603	0.001002	-
Al_2O_3	3970	765	40	-	15

The thermophysical properties of the equivalent homogeneous fluid are evaluated as follows:

The density of the equivalent homogeneous fluid is (Xuan and Roetzel, 2000):

$$\rho_{nf} = (1 - \phi)\rho_{bf} + \phi\rho_{np} \tag{2.17}$$

The equivalent homogeneous fluid specific heat capacity is (Xuan and Roetzel, 2000):

$$Cp_{nf} = (1 - \phi)Cp_{bf} + \phi Cp_{np} \tag{2.18}$$

The thermal conductivity of the equivalent homogeneous fluid is (Xuan and Roetzel, 2000):

$$k_{nf} = k_{bf}\frac{k_{np} + 2k_{bf} - 2\phi(k_{bf} - k_{np})}{k_{np} + 2k_{bf} + \phi(k_{bf} - k_{np})} \tag{2.19}$$

The effective dynamic viscosity of the equivalent homogeneous fluid is (Ali et al., 2021b):

$$\mu_{nf} = \mu_{bf}(123\phi^2 + 7.3\phi + 1) \tag{2.20}$$

In the two-phase mixture model, Φ from Table 2.2 replaces ϕ in equations (2.17)-(2.20) to evaluate the second phase thermophysical properties.

Table 2.2 Combinations of second phase volume fraction and of second phase nanoparticle volume fraction giving the same ϕ =1% Al_2O_3 nanofluid mixture.

Second phase volume fraction α_{nf}	0.5	0.2	0.1	0.08	0.06	0.04	0.02
Second phase Al_2O_3 nanoparticle volume fraction Φ	0.02	0.05	0.1	0.125	0.1667	0.25	0.5

2.3 Boundary conditions

To solve the governing equations in sections 2.1.1 and 2.1.2 the following time-invariant conditions are imposed uniformly at each computational domain boundary:

1. Minichannel inlet first and second phases

   $u_1 = u_{in}, u_2 = u_3 = 0$ for fluid $T_f = T_{in}$

   for solid $\frac{\partial T_s}{\partial x_1} = 0$

2. Minichannel outlet first and second phases

   $p_f = p_{out} = 1$ atm   for fluid $\frac{\partial T_f}{\partial x_1} = 0$

   for solid $\frac{\partial T_s}{\partial x_1} = 0$

3. The top wall $\qquad$ solid $\frac{\partial T_s}{\partial x_2} = 0$

4. Right and left walls   (symmetry) $\qquad$ solid $\frac{\partial T_s}{\partial x_3} = 0$

5. Base wall $\qquad$ $-k_s \frac{\partial T_s}{\partial x_2} = \dot{q}_2$

6. Inner walls $\quad u_1 = u_2 = u_3 = 0 \qquad$ $-k_s \frac{\partial T_s}{\partial x_n} = -k_f \frac{\partial T_f}{\partial x_n}$
(fluid/solid surface)

where n, k_f and k_s are, respectively, the coordinate normal to the wall, the working fluid thermal conductivity, and the solid wall thermal conductivity. In the single-phase approach $k_f = k_{nf}$ and in the two-phase approach $k_f = k_m$.

2.4 Numerical solver

The three-dimensional computational domain for all minichannel and microchannel heat sinks. A two-dimensional computational domain for a horizontal backward-facing step. The conjugate heat transfer problem is solved numerically using the commercial software FLUENT version 19.5, by ANSYS Inc., Canonsburg, PA, USA. The flow is defined either as constant property, incompressible, laminar and single-phase or a constant property, incompressible, laminar and two-phase mixture. ANSYS FLUENT 19.5 was used to solve numerically the three-dimensional conjugate heat transfer model defined by the heat and mass transport governing equations and boundary conditions of the previous section. The numerical solver setup in FLUENT for Single-phase and Multiphase mixture models are shown in Table 2.3 and Table 2.4, respectively (Li et al., 2020). Thermal coupling at the fluid-solid boundaries was achieved by using the predicted wall temperature from the flow solver as the boundary condition for the Laplace equation and the heat flux vector prediction from the Laplace equation solver as the boundary condition for the flow solver, iterating to convergence. This approach is reported in Radenac et al. (2014) as being the most robust one according to Giles' stability analysis (Giles, 1997). The double-precision steady pressure-based Coupled flow solver of Multiphase mixture model is used with the PRESTO! scheme for pressure, with the second-order upwind method for the momentum and energy equations, and with the QUICK scheme for the volume fraction equation (Li et al., 2020). The hybrid initialisation of ANSYS FLUENT 19.5 provides the interior flow conditions and the temperature distribution in the solid domain portion at the start of the computation. The implicit scheme iterates the solution with a Courant number limit of 40, an explicit relaxation

factor of 0.5 for momentum and pressure, and under-relaxation factors of 0.1 and 0.4 for the slip velocity and the volume fraction, respectively (ANSYS, 2018). Multi-grid acceleration is implemented for the volume fraction with a flexible cycle, which is limited to two sweeps, 30 fine relaxation levels, and 50 coarse relaxation levels, these values as default in FLUENT. The solution was deemed converged when the residuals for the continuity, momentum and energy equations fell below 1×10^{-6} (Ghani et al., 2017b). The computational cost of each simulation shown in Table 2.5 on a 3.2 GHz sixteen core shared memory computer cluster.

Table 2.3 The numerical solver setup in FLUENT for the single-phase model.

General	Time: Steady Gravity: On Y=(m/s2): -9.81		
Models	Energy: On Viscous: Laminar		
Materials	Solid: Heat sink material Liquid: Water		
Boundary Conditions	Velocity-Inlet	Momentum	Velocity Specification Method: Magnitude, Normal to Boundary Velocity Magnitude (u_{in})
		Thermal	Temperature (T_{in})
	Pressure-Outlet	p_{out} = 1 atm	
	Walls	Thermal	Base wall: Heat flux ($\dot{q}_2$) Symmetry: Heat flux (0) The top wall: Heat flux (0)
Mesh Interfaces	Reference Values	Compute From: Inlet	
Methods	Scheme: SIMPLE Pressure: Second Order Momentum: Second Order Upwind) Energy: Second Order Upwind		
Controls	Default		
Monitors	Residual	continuity: 1×10^{-6} velocity: 1×10^{-6} energy: 1×10^{-6}	
Initialization	Hybrid Initialization		

Table 2.4 The numerical solver setup in FLUENT for the multiphase mixture model.

General	Time: Steady Gravity: On Y=(m/s2):-9.81		
Models	Multiphase	Models	Mixture Mixture Parameters: Slip Velocity Number of Phases: 2
		Phases	Primary phase: Water Secondary phase: Nanofluid
		Phase interaction	Drag Coefficient: schiller-naumann Slip Velocity: manninen-et-al
	Energy: On Viscous: Laminar		
Materials	Solid: Heat sink materiel Liquid: Water Liquid: Nanofluid		
Boundary Conditions	Velocity-Inlet	Momentum inlet first and second phases	Velocity Specification Method: Magnitude, Normal to Boundary Velocity Magnitude (u_{in})
		Thermal	Temperature (T_{in})
	Pressure-Outlet first and second phases	$p_{out} = 1$ atm	
	Walls	Thermal	Base wall: Heat flux ($\dot{q}_2$) Symmetry: Heat flux (0) The top wall: Heat flux (0)
Mesh Interfaces	Reference Values	Compute From: Inlet	
Methods	Scheme: Coupled Pressure: PRESTO! Momentum: Second Order Upwind Volume Fraction: Quick Energy: Second Order Upwind		
Controls	Flow Courant Number: 40		
	Explicit relaxation factor	Momentum: 0.5 Pressure: 0.5	
	Under-relaxation factors	Slip Velocity: 0.1 Volume Fraction: 0.4	
Monitors	Residual	Continuity: 1×10^{-6} Velocity: 1×10^{-6} Energy: 1×10^{-7}	
Initialization	Hybrid Initialization		

Table 2.5 The computation cost of the simulation.

	Wall time
Microchannel heat sink using twisted tape	02:00 hours
Microchannel heat sink using various twisted tapes	02:30 hours
Microchannel heat sink using various fins	02:30 hours
Minichannel heat sink using mixture model	30 minutes

2.5 Data reduction

The thermal performance of the microchannel heat sink is assessed via conventional heat transfer quantities. The convection heat transfer coefficient h of the microchannel heat sink and its average h_{avr} is (Bahiraei and Heshmatian, 2017):

$$h_{avr} = \frac{\dot{q}_2}{T_{max} - T_m} \tag{2.21}$$

In equation (2.21), T_{max} is the average bottom wall temperature and $\dot{q}_2$ is the heat flux vector normal to the bottom wall, into the wall, from an external heat source.

$$T_m = \frac{T_{in} + T_{out}}{2} \tag{2.22}$$

In equation (2.22), T_{out} is the outlet temperature of the fluid leaving the microchannel heat sink.

The local Nusselt number Nu_x and the average Nusselt number Nu are defined as (Ghasemi et al., 2017).

$$Nu_x = \frac{D_h \left(\partial T_f / \partial x_n \right)}{T_{max} - T_m} \tag{2.23}$$

and

$$Nu = \frac{h_{avr} D_h}{k_f} \tag{2.24}$$

The total thermal resistance is defined as (Ghasemi et al., 2017):

$$R_{Total} = \frac{T_{max} - T_{in}}{\dot{q}_2} \tag{2.25}$$

The friction factor f of each individual microchannel tube is given by (Ghasemi et al., 2017):

$$f = \frac{2D_h \Delta p}{\rho_f u_{in}^2 L} \qquad (2.26)$$

where

$$\Delta p = p_{in} - p_{out} \qquad (2.27)$$

is the pressure drop of the working fluid between the inlet and the outlet (Bahiraei et al., 2019b). The pumping power supplied to the microchannel heat sink is given by (Bahiraei et al., 2019b) as.

$$P_p = \Delta p . V \qquad (2.28)$$

where V is the volume flow rate.

The cooling performance of each microchannel design is examined to assess whether adding a swirl in the flow is beneficial or otherwise. A Figure of Merit (FoM) is used to calculate the overall thermo-hydraulic performance by comparing the change in the average Nusselt number to that in the friction factor (Bahiraei et al., 2019c). This is evaluated as

$$FoM = \frac{Nu/Nu_0}{(f/f_0)^{1/3}} \qquad (2.29)$$

where subscript 0 denotes the microchannel configuration of Figure 3.1(b) with no tape, Figure 4.1 (d) with no tape and Figure 5.1 (d).

2.6 The second law efficiency analysis of the minichannel heat sink flow

The second law efficiency evaluates the quality of the thermodynamic process performed by a heat sink. It does so by considering the irreversibility of the cooling process. The primary sources of irreversibility are the temperature drop in the heat that is transported and the friction losses in the working fluid. One method to determine the magnitudes of these irreversibilities is evaluating the steady flow exergy balance (Cengel, 2010b), using the inlet flow temperature and the outflow pressure of the working fluid as the reference dead state. Figure 2.1 shows the control-volume two-dimensional schematic of a heat sink with a steady through flow and a constant heat flux from the bottom. The

exergy destruction rate ($\dot{E}_{xd}$) from the exergy balance through the dashed line control volume is (Ali et al., 2021a):
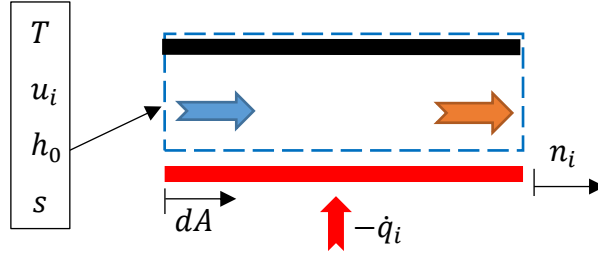

Figure 2.1: The control-volume two-dimensional schematic of a minichannel heat sink.

$$\dot{E}_{xd} = -\iint_{base} \left(1 - \frac{T_r}{T}\right) \dot{q}_i n_i \, dA - \iint_{inlet} \rho_{nf} \psi u_i n_i \, dA - \iint_{outlet} \rho_{nf} \psi u_i n_i \, dA \tag{2.30}$$

where T_r is the dead state reference temperature, which is equal to the inlet temperature T_{in}, T is the temperature at the control volume surface, $\dot{q}_i$ is the heat flux vector, which is defined positive outwards from the control volume, n_i is the control volume boundary normal unit vector, which is positive outwards, u_i is the working fluid velocity, and ψ is the flow exergy. The latter is defined as

$$\psi = (h_0 - h_{0r}) - T_r(s - s_r) \tag{2.31}$$

where h_0, $h_{0r}, s \text{ and } s_r$ are the specific stagnation enthalpy, the specific stagnation enthalpy at T_r, the specific entropy, and the specific entropy at T_r, respectively. The contribution to the flow exergy owing to gravity is disregarded, as the inlet and the outlet of the minichannel are horizontally aligend (Ali et al., 2021b). The constant property incompressible flow assumption in the single-phase and two-phase mixture models enables restating equation (2.31) as

$$\psi = Cp_{nf} \left(T_0 + \frac{u_i^2}{2Cp_{nf}} - T_{0r} - \frac{u_i^2}{2Cp_{nf}} - T_r \ln\left(\frac{T}{T_r}\right)\right) \tag{2.32}$$

where Cp_{nf} is evaluated from equation (2.18) using $\phi = 1\%$ for all simulations.

The rate of exergy expended ($\dot{E}_x$) through the minichannel cooling process is the sum of the total reversible work rate potential of the heat supplied through the base, as identified in Liu et al. (2018a), plus the reversible work rate potential of the coolant supplied to the inlet, as identified in Ali et al. (2021a). This gives

$$\dot{E}_x = -\iint_{base} \left(1 - \frac{T_r}{T}\right) \dot{q}_i n_i \, dA - \iint_{inlet} \rho_{nf} \psi u_i n_i \, dA \qquad (2.32)$$

In equations (2.30) and (2.32), ρ_{nf} is the density of the working fluid evaluated by equations (2.17) with $\phi = 1\%$.

By combining the exergy destruction rate and the rate of exergy expended, the second law efficiency of the minchannel heat sink is determined as (Ali et al., 2021b).

$$\eta_{II} = (1 - \frac{\dot{E}_{xd}}{\dot{E}_x}) \qquad (2.33)$$

2.7 Field synergy analysis of the microchannel heat sink flow

A microchannel heat sink removes heat at a target rate by a dominant convective heat transfer mode at the expense of mechanical pumping power input. A high heat removal rate and a low mechanical pumping power requirement are desirable. Field synergy provides figures of merit for the quality of these processes.

A steady, incompressible, neutrally buoyant flow moves according to the force-momentum balance

$$\rho u_j \frac{\partial u_i}{\partial x_j} = -\frac{\partial p}{\partial x_i} + \mu \frac{\partial^2 u_i}{\partial x_j^2} \qquad (2.34)$$

Its kinetic energy transport equation is obtained by the scalar product of the force-momentum balance with the velocity vector u_i. This provides the scalar equation

$$\rho u_j \frac{\partial}{\partial x_j} \frac{u_i^2}{2} - \mu u_i \frac{\partial^2 u_i}{\partial x_j^2} = -u_i \frac{\partial p}{\partial x_i} \qquad (2.35)$$

The right-hand term can be interpreted as the work rate per unit volume performed by the pressure field onto the flow to transport the kinetic energy per unit volume against the action of the viscous stresses, the left-hand terms. Let (Liu et al., 2019)

$$\theta = \arccos\left(\frac{u_i\left(-\frac{\partial p}{\partial x_i}\right)}{|u_i|\left|\frac{\partial p}{\partial x_i}\right|}\right) \qquad (2.36)$$

The work rate per unit volume becomes $|u_i| \left| \frac{\partial p}{\partial x_i} \right| \cos \theta$. Integrating over the microchannel domain volume occupied by fluid gives the work rate input required for moving the flow through the microchannel

$$-\dot{W} = \iiint |u_i| \left| \frac{\partial p}{\partial x_i} \right| \cos \theta \ dx_i = (\cos \bar{\theta}) \iiint |u_i| \left| \frac{\partial p}{\partial x_i} \right| dx_i \tag{2.37}$$

where

$$\bar{\theta} = \arccos \frac{\iiint |u_i| \left| \frac{\partial p}{\partial x_i} \right| \cos \theta \ dx_i}{\iiint |u_i| \left| \frac{\partial p}{\partial x_i} \right| dx_i} \tag{2.38}$$

The weighted volume average $\bar{\theta}$ expresses the field compatibility between the pressure gradient and the flow velocity. The highest work rate input requirement occurs for $\bar{\theta} \to 0$, so $\bar{\theta} \to -\pi/2$ is desirable for reducing the external pumping power requirement.

Similar arguments can be developed based on the steady heat transport and diffusion equation for a constant property incompressible fluid

$$\rho C_p u_i \frac{\partial T}{\partial x_i} = k \frac{\partial^2 T}{\partial x_i^2} \tag{2.39}$$

Let (Liu et al., 2019)

$$\beta = \arccos \left(\frac{u_i \frac{\partial T}{\partial x_i}}{|u_i| \left| \frac{\partial T}{\partial x_i} \right|} \right) \tag{2.40}$$

The convective heat transfer rate per unit volume becomes $|u_i| \left| \frac{\partial T}{\partial x_i} \right| \cos \beta$. Integrating over the microchannel domain volume occupied by fluid gives the convective heat rate output from the microchannel

$$\dot{Q} = \rho C_p \iiint |u_i| \left| \frac{\partial T}{\partial x_i} \right| \cos \beta \ dx_i = \rho C_p (\cos \bar{\beta}) \iiint |u_i| \left| \frac{\partial T}{\partial x_i} \right| dx_i \tag{2.41}$$

where

$$\bar{\beta} = \arccos \frac{\iiint |u_i| \left|\frac{\partial T}{\partial x_i}\right| \cos \beta \ dx_i}{\iiint |u_i| \left|\frac{\partial T}{\partial x_i}\right| dx_i} \tag{2.42}$$

The weighted volume average $\bar{\beta}$ expresses the field compatibility between the temperature gradient and the flow velocity. The highest convective heat sink rate occurs for $\bar{\beta} \to 0$, so $\bar{\beta} \to 0$ is desirable for maximising the rate of heat removal by the microchannel.

Chapter 3: Thermo-hydraulic performance of a circular microchannel heat sink using swirl flow and nanofluid

3.1 Introduction

A sustained demand for electronics with greater power density for everyday use as well as for specialist applications, such as for High Performance Computing (HPC), requires heat sinks capable of extracting greater heat loads while keeping the electronic equipment at temperatures sufficiently low so as not to compromise their service life. Traditional cooling methods and ordinary fluids struggle to remove high heat flux from the more demanding electronic chips. Therefore, new approaches and working fluids delivering high-thermal performance are required to provide high efficiency and reliability (Sharma et al., 2013). Microchannel heat sinks with an air convection fin array are still widely used, but this technology is seen as having limited performance growth capacity to meet the higher heat flux dissipation demand from the more performing electronic components (Tullius et al., 2011). Therefore, liquid-cooled microchannel heat sinks are gradually replacing air-cooled heat sinks to accommodate the high power density electronic designs and keep the temperature in the electronic component low. Microchannel heat sinks have been improved and modified by trying serval techniques, such as changing the material of the channel walls, altering the cross-section and shape of the channels, using two layers of channels instead of a single layer, inserting various types of plates and ribs, and using nanofluid instead of ordinary fluid. Heat sink walls have been improved and modified through the use of different materials, such as aluminium and copper (Hung et al., 2012). Other materials were also investigated, such as stainless steel (Peng et al., 1994a), glass (Koşar, 2010), and bronze (Gamrat et al., 2005). However, no significant change was found in the thermal performance by changing the material used to form small channels, only becoming significant as the channels became larger (Adham et al., 2013). Some authors reported issues related to the contact surface between the electronic component and heat sink, which were solved by fabricating the heat sink from a combination of different materials (Adham et al., 2013).

Many researchers reported that the cooling systems with coolants modified by chemical additives have better performance than without additives in electronic applications (Arani et al., 2017). While other researchers attempted to improve the thermal properties of the working fluid, these investigations found that adding solid nanoparticles

to ordinary fluid, such as water, engine oils and ethylene glycol, to form a so-called Nanofluid produces a coolant with better thermal properties (Saini et al., 2016). The thermal properties of the nanoparticles play a key role in the high thermal performance of the nanofluid, by affecting the nanofluid thermal diffusivity, its friction factor, its convection heat transfer, and the nanoparticle migration inside the nanofluid (Vajjha et al., 2010, Ashrafmansouri and Nasr Esfahany, 2014, Bahiraei, 2016). Past investigations with a nanofluid have often reported a significant enhancement of the heat transfer in cooling systems (Vajjha et al., 2010). This prompted the testing of nanofluid coolants in many types of systems, such as plate heat exchangers, double-pipe heat exchangers, shell and tube heat exchangers, minichannels and microchannel heat exchangers (Bahiraei et al., 2018).

Various authors have reported that using a nanofluid instead of water increases the heat transfer rate of heat sinks. Thermal performance enhancements of the order of 8% were achieved by adding to the base flow nanoparticles of CuO by Al-Rashed et al. (2016), of SiO_2 by Hashemi et al. (2012), and of Cu by Abbassi and Aghanajafi (2006). Korpyś et al. (2012) tested Al_2O_3 and CuO nanofluids for cooling a microprocessor. In this case, pure water was found to provide adequate cooling and there was no need for using a nanofluid.

The geometry of the cross-section of a cooling channel has a significant effect on the heat transfer characteristics of a microchannel heat sink. Comparisons among circular, hexagonal, and rhombus-shaped cross-sections in Alfaryjat et al. (2014), trapezoidal, triangular, and rectangular cross-sections in Gunnasegaran et al. (2010), and rectangular and circular cross-sections in Ghasemi et al. (2017) and in Mohd-Ghazali et al. (2019) indicate a heat transfer performance advantage by the more polygonal sections. In laminar flow, this typically attracts a pressure drop penalty with respect to a circular pipe. For the case of re-entrant channels, which are parallel grooves cut into a flat surface, Deng et al. (2015) found that an Ω-shaped re-entrant microchannel could provide a 39% higher Nusselt number and a 22% lower thermal resistance than a square one.

Layering multiple liquid blocks has been explored, either with single-phase coolant or with nanofluid, for enhancing the heat transfer performance of micro-channel heat sinks. Thermal resistance reductions of 50% and 30% were reported by Cheng (2007) and by Wei and Joshi (2003), respectively, by using two layers compared to single-layer

microchannels. Some of this thermal performance advantage is retained were the two-layer geometry is used with nanofluid of Al_2O_3, as in Hung and Yan (2012b), of carbon (MWCNT) or metal oxides, as in Sarlak et al. (2019), and of Al_2O_3-Cu, a hybrid nanofluid, as in, Mashayekhi et al. (2018), in laminar flow. Adding the nanoparticles often increases the effective viscosity of the working fluid, resulting in a higher pressure drop over the channel length, as reported in some of these studies.

Laminar flow in microchannels does not feature the natural mixing that characterises turbulent pipe flows (Taliaferro et al., 2016, Angelino et al., 2019) and geometric features that induce such mixing may aid the transport of heat away from the channel walls. In microchannels, various flow trips have been tested, such as Y-shaped bifurcations in ribs of five different shapes in Chai et al. (2016) and sinusoidal cavities and ribs in Ghani et al. (2017a). The longer and wider Y bifurcations, the elliptical ribs, and the cavities of 0.15 ratio of amplitude to the cavity length in combination with 0.3 ratios of rib width to the channel width and 0.5 ratios of rib length to the cavity length were found to improve the heat transport performance compared to a channel of uniform rectangular cross-section. A related technique for better distributing flow coolant is using secondary oblique channels, to increase the heat transfer surface, in combination with ribs, to direct the flow through these channels, as in Ghani et al. (2017b) and in Bahiraei et al. (2019b). Ghani et al. (2017b) showed that it is possible this way to achieve better heat transfer as well as a lower pressure drop than with a ribbed micro-channel. Bahiraei et al. (2019b) showed that using graphene-silver hybrid nanofluid benefits the heat transfer performance of this type of geometry. Ghani et al. (2017b) showed that it is possible this way to achieve better heat transfer as well as a lower pressure drop than with a ribbed micro-channel. Bahiraei et al. (2019b) showed that using graphene-silver hybrid nanofluid benefits the heat transfer performance of this type of geometry. Khodabandeh et al. (2019) combined the use of trips and layering, using ribs and sinusoidal flow passages arranged in two layers. The proposed design with ribs showed a much higher heat transfer and causes a sharp increase in the pressure drop compared to the microchannel heat sink without ribs. Different designs where concurrent transfer rate gains and pressure losses are present are often compared based on a Figure of Merit (Bahiraei et al., 2019c), which is the ratio of the percentage gain in heat transfer rate over the percentage increase in the pumping power required. Further insight into the quality of the mass and heat transport can be gained by considering the irreversibility in the cooling process, quantified by entropy generation

(Bejan, 2013, Bejan, 1996, Balaji et al., 2007), exergy destruction (Liu et al., 2018a), and the second law efficiency. The field synergy principle Liu et al. (2019) gives an additional quality metric of the heat and mass transport processes.

Twisted tapes have been used in large channels to improve heat transfer performance by changing the axial flow into swirl flow. Swirl can decrease the thermal resistance in the heat exchanger by increasing the velocity of the flow near the channel wall. Swirl can be induced in channels using a variety of inserts that, by improving the heat transfer performance, can reduce the size of the heat exchangers (Hosseinnejad et al., 2019). One of such inserts is a twisted tape, which is easy to produce and use. Improvements in the heat transfer coefficient by inserting a twisted tape are documented by Sundar and Sharma (2010), in turbulent channel flow with both pure water and 0.5% volume Al_2O_3 nanofluid, and in laminar and turbulent channels by Akbari et al. (2017), who explored the effect of tape twist pitch, width, and nanoparticle concentration. Fitting two or three parallel running twisted tapes, either along the channel full length or regularly spaced, was reported by Eiamsa-ard et al. (2010) to perform thermally better than a single twisted tape, but at a 23% higher friction factor, a trend confirmed by Liu et al. (2018b) over the Reynolds number range 40 to 1050 in oil flow.

To date, no investigation has been performed on the thermo-hydraulic effects of inserting a single twisted tape in a circular microchannel heat sink running either single-phase or nanofluid coolants. Addressing this knowledge gap, a numerical investigation is herein presented on the thermal performance of a forced-convection circular microchannel heat sink with either no tape (MC-NT), a straight tape (MC-ST), or a twisted tape (MC-TT), over the Reynolds number range $100 \leq Re \leq 350$, cooled by Al_2O_3 nanofluid at volume fraction concentrations $\phi = 0$, 1, 2 and 3%. The intent is to combine swirl flow, which previous work has shown to enhance near-wall heat transport in larger channels, with the greater thermal conductivity provided by the nanofluid, in a microchannel. It is shown that these two features can be combined to decrease the microchannel thermal resistance and reduce the contact temperature at the base of the heat sink, for a heat flux input representative of a microprocessor core.

3.2 Geometry and boundary conditions

This research uses a generalized geometry of a microchannel heat sink. It is made up of a prism with four evenly spaced circular microchannels running parallel to one another,

through which the nanofluid flows. Table 3.2 shows the dimensions of the circular microchannel heat sink and the twisted tape used in this study. As the majority of modern integrated circuit chips are made of silicon, a microchannel heat sinks also made in silicon is considered, in order to decrease the thermal stress between the chip and heat sink. In principles, the microchannel can be fabricated from a silicon blank by boring the passages and then fitting and CO_2 welding the tapes, thermally formed from plane strips. Alternatively, the geometry could be produced in copper to a near-finished shape, by three-dimensional printing technologies known as metal binder jetting process and metal powder bed fusion in copper and other metals.

The Reynolds number ranges from 100 to 350 and the inlet temperature T_{in} of the working fluid is fixed at 298 K. A constant heat flux of 100 W/cm^2 was prescribed at the bottom wall The Reynolds number at the inlet of the microchannel heat sink is:

$$R_e = \frac{\rho_{nf} \cdot u_{in} \cdot D_{h_{NT}}}{\mu_{nf}} \tag{2.7}$$

$$D_{h_{TT}} = D - \frac{4A}{P} = D - \frac{4\,ab}{2(a+b)} = D - \frac{2\,ab}{a+b} \tag{2.8}$$

where A is the tape cross-section area, P its perimeter, and a and b are the width and thickness of the tape, respectively.

Table 3.1 The thermo-physical properties of silicon (Wang et al., 2011).

Material	ρ (kg m^{-3})	Cp (J/kg. K)	k (W/m. K)
Silicon	2330	710	148

Table 3.2 Dimensions of the circular microchannel heat sink, in mm.

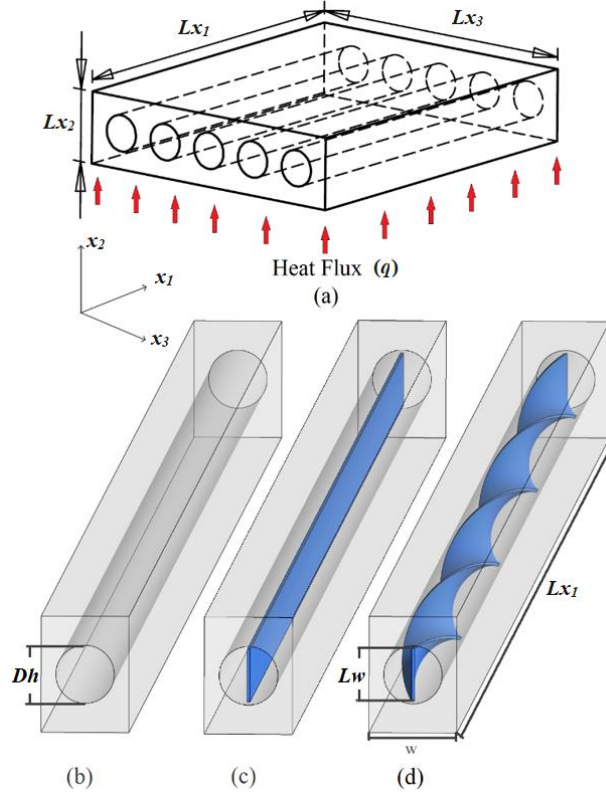| Lx_1	Lx_2	Lx_3	Dh_{NT}	Dh_{TT}	W	Lt	Lw	Twisted tape thickness
10	0.4	10	0.2	0.18	0.3	10	0.16	0.01

Figure 3.1 Schematic of the circular microchannel heat sink. (b) The normal microchannel heat sink without twisted tape (MC-NT), (c) The microchannel heat sink with a straight tape (MC-ST) and (d) The microchannel heat sink with a twisted tape (MC-TT).

3.3 Grid independence

A numerical mesh dependence study was performed to identify a numerical mesh size that provides acceptably low variations in the results with further mesh refinement. In this paper, a hexahedral mesh is used because it typically provides better accuracy and a shorter solution time than tetrahedral or mixed element meshes in domains with a simple prismatic geometry (Viceconti et al., 1998). The quality of the mesh was evaluated by examining several grid sizes to ensure the computational results are substantially mesh-independent. In this test, the MC-TT with water at the Reynolds number of 250 was tested for mesh dependence by progressively increasing the number of elements. Figure 3.3 (a and b) shows the predicted average bottom wall temperature and the pressure drop as a function of the number of elements. This figure shows no significant change in the average bottom wall temperature and the pressure drop by increasing the number of elements from 3M to 4.3M. Therefore, the grid with 3,545,805 cells is used for modelling circular microchannel heat sink without and with twisted tape. Figure 3.3 shows the structure of the mesh that was used.
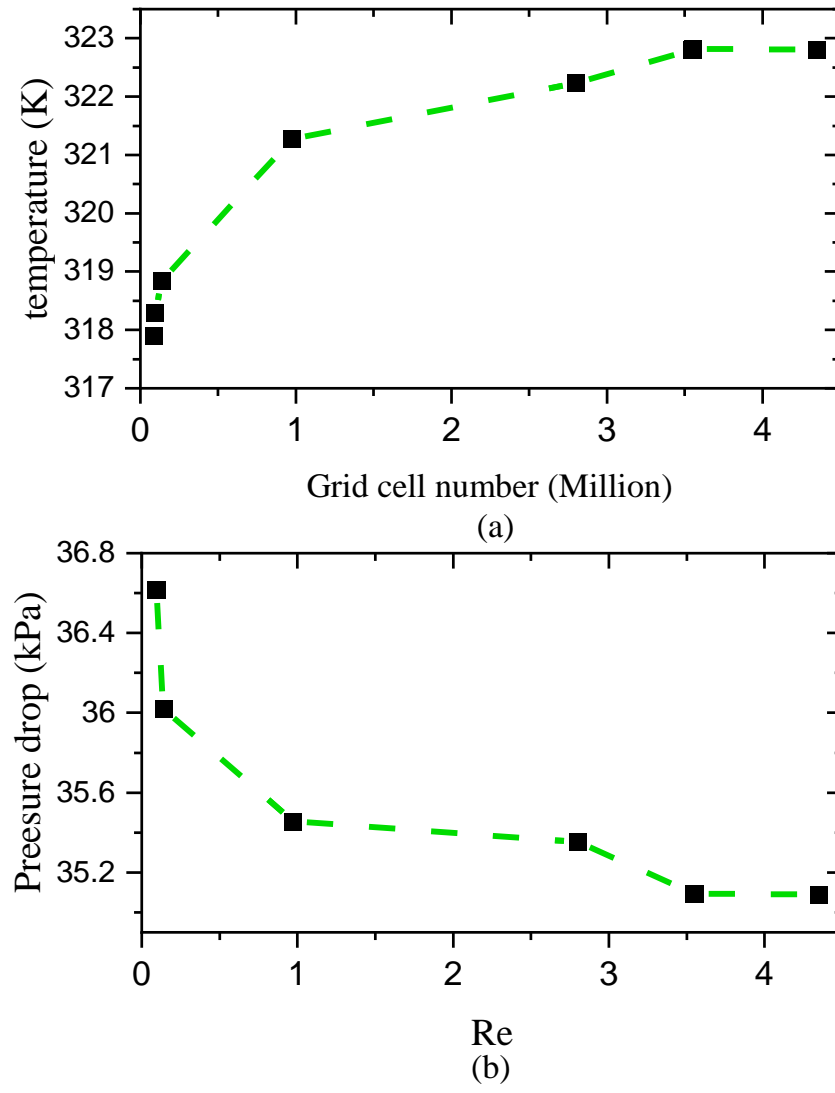
(a)

(b)

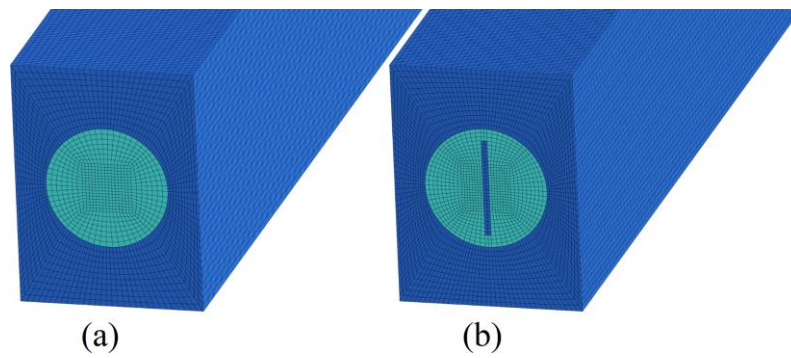Figure 3.2 Grid dependence test at $Re = 250$: (a) Average bottom wall temperature, (b) Pressure drop.

Figure 3.3 Three-dimensional mesh structure of (a) MC-NT and (b) MC-TT.

3.4 Model validation

To assess the accuracy of the numerical predictions, Figure 3.4(a) compares the friction factor of MC-NT against the Darcy friction factor for a fully developed laminar flow in a straight pipe of circular cross-section, evaluated from the Hagen-Poiseuille law (Cengel, 2010b). The Darcy friction factor is calculated from $f = 64\,Re^{-1}$ (Cengel, 2010b). This formula is only applicable to the hydrodynamically fully developed region. Therefore, the entry length $L_h \cong 0.05 Re D_h$ is estimated in order to find the hydrodynamic entrance region (Cengel, 2010b). Figure 3.4 (a) shows that there is an excellent agreement between the Darcy friction factor from the Hagen-Poiseuille law and that predicted from the numerical model, as the two curves overlap. The current study gives confidence that the model can satisfactorily predict the hydraulic head loss through the microchannel. In addition, Figure 3.4 (b) displays the local Nusselt number for MC-NT compared with the one obtained by the Shah correlation (Narendran et al., 2020) of equation (2.30). The results in Figure 3.4 (b) show that the current result is in reasonably good agreement with the Shah correlation, with a maximum deviation of 6.9%.

$$Nu = \begin{cases} 1.953(RePr\dfrac{D_h}{x})^{1/3} & (RePr\dfrac{D_h}{x}) \geq 33.3 \\ 4.364 + 0.0722(RePr\dfrac{D_h}{x}) & (RePr\dfrac{D_h}{x}) < 33.3 \end{cases} \qquad (2.30)$$
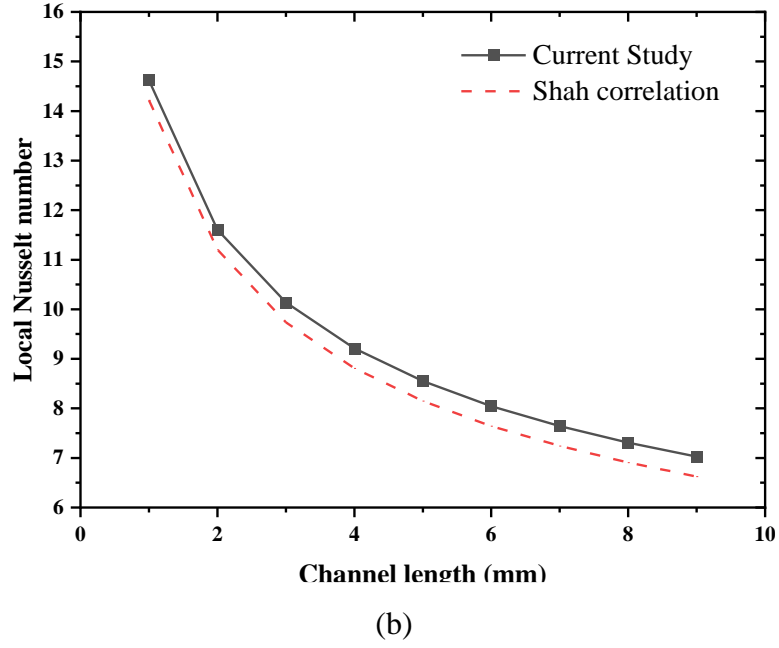

(a)

(b)
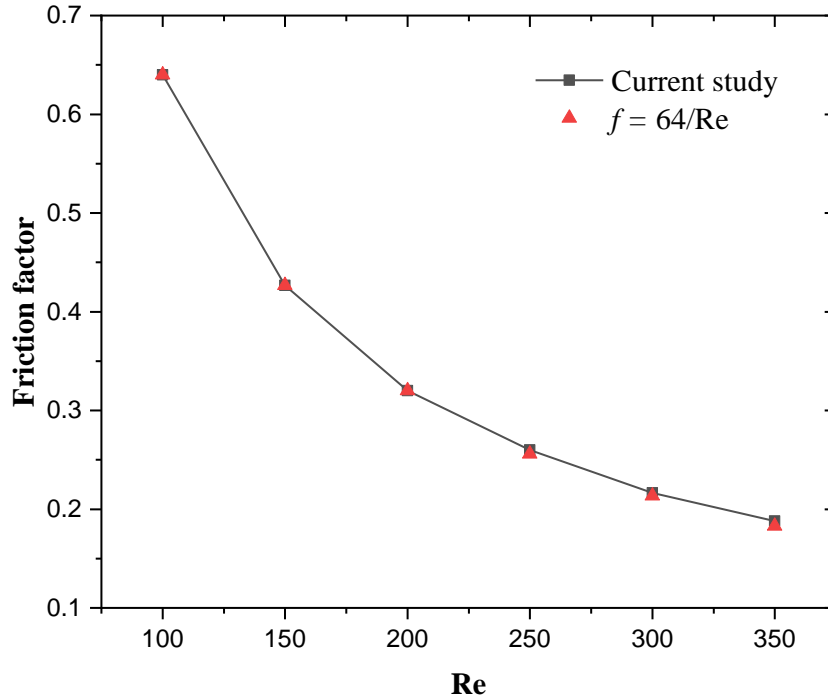
Figure 3.4 Validation of (a) friction factor and (b) local Nusselt number of MC-NT.

3.5 Results and Discussion

This section describes the thermal performance of the circular microchannel heat sink with twisted tape (MC-TT) compared to that of a circular microchannel heat sink without twisted tape (MC-NT).

3.5.1 Effects of twisted tape on the microchannel heat sink temperature

Figure 3.5 shows the temperature distributions on the bottom surface and on the inner wall of MC-NT, MC-ST and MC-TT. These were evaluated at Re=250 using water as a working fluid. The surface temperature distribution is displayed in colour iso-levels, with red associated to 343 K and blue to 305 K. The transparency of Figure 3.5 allows viewing the temperature distribution on both surfaces in the same image. Figure 3.5 shows that both the bottom and the inner wall surface temperatures decrease by inserting a straight tape and then further decreases in the temperature are achieved by twisting the tape. Specifically, MC-NT microchannel has the highest wall surface temperature at the channel entry (in cyan) and exit (in red), both on the microchannel floor and on the pipe wall. The tape insert has the effect of visibly reducing these surface temperatures, which, in the case of the straight tape, reduce to below 310 K (in light blue) at entry and to about 333 K (in yellow) at exit. Further temperature reductions to 305 K at entry and to 326 K at exit are obtained with the twisted tape insert. This is because the twisted tape creates swirl, which can help to mix the fluid and increase the flow velocity near to the wall, as shown in Figure 3.10.
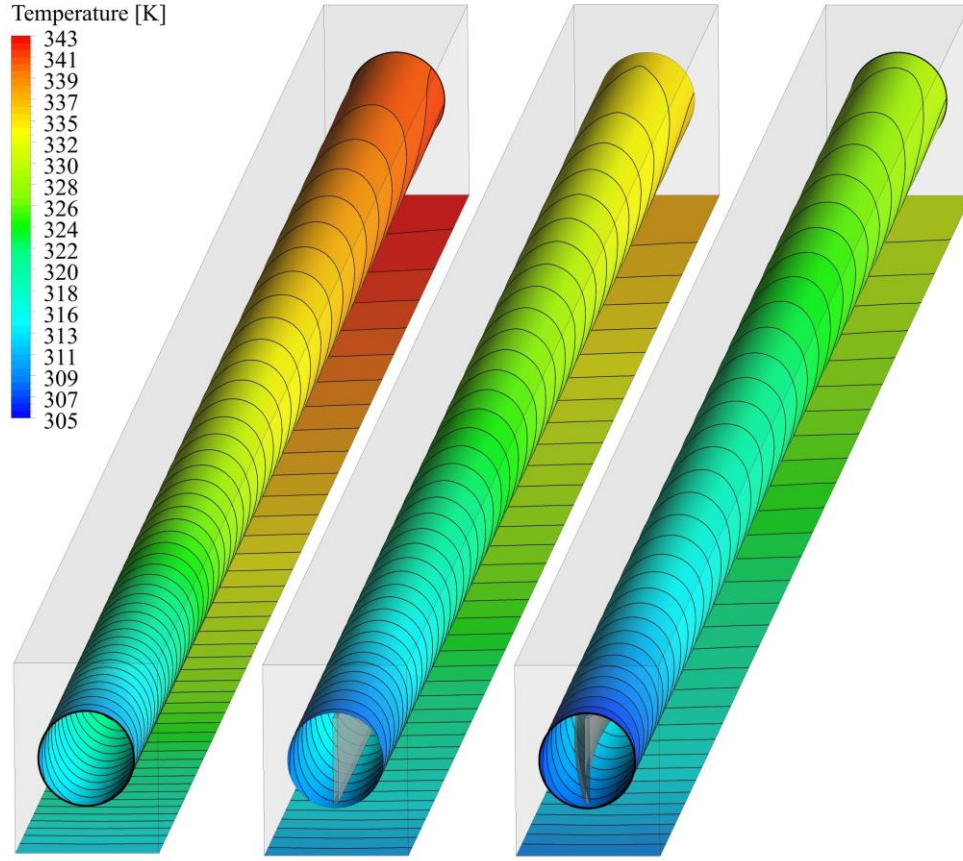
32

Figure 3.5 Temperature colour iso-levels on the heated surface and inner wall at $Re = 250$ and $\phi = 0$ of MC-NT (left), MC-ST (centre), and MC-TT (right).

Figure 3.6 shows the temperature distribution at Reynolds numbers between 100 to 350 and using water as the working fluid of MC-TT, which is the best performing configuration identified in Figure 3.5. The results show that the cooling performance is improved by increasing the Reynolds number and the best cooling performance within the range used is reached at the Reynolds number of 350. This improvement is achieved by a reduction in the convection thermal resistance. Moreover, the effect of increasing the volume concentration of Al_2O_3 nanoparticles was investigated via modelling the same configurations with $\phi = 0, 1, 2,$ and 3%. The result shows that both bottom and an inner wall surfaces temperature decrease by adding more nanoparticles and the best cooling performance within the range used is achieved at $\phi = 3\%$. This enhancement is due to the Al_2O_3 nanoparticles having lower heat capacity and higher thermal conductivity compared to pure water, according to equation (2.4) and equation (2.5), respectively. Lower heat capacity means that the fluid will cool down and warm up quickly as it takes less energy

to change its temperature (Halliday et al., 2013). Higher thermal conductivity means the fluid will have a higher ability to transfer or conduct heat (Choi and Eastman, 1995).
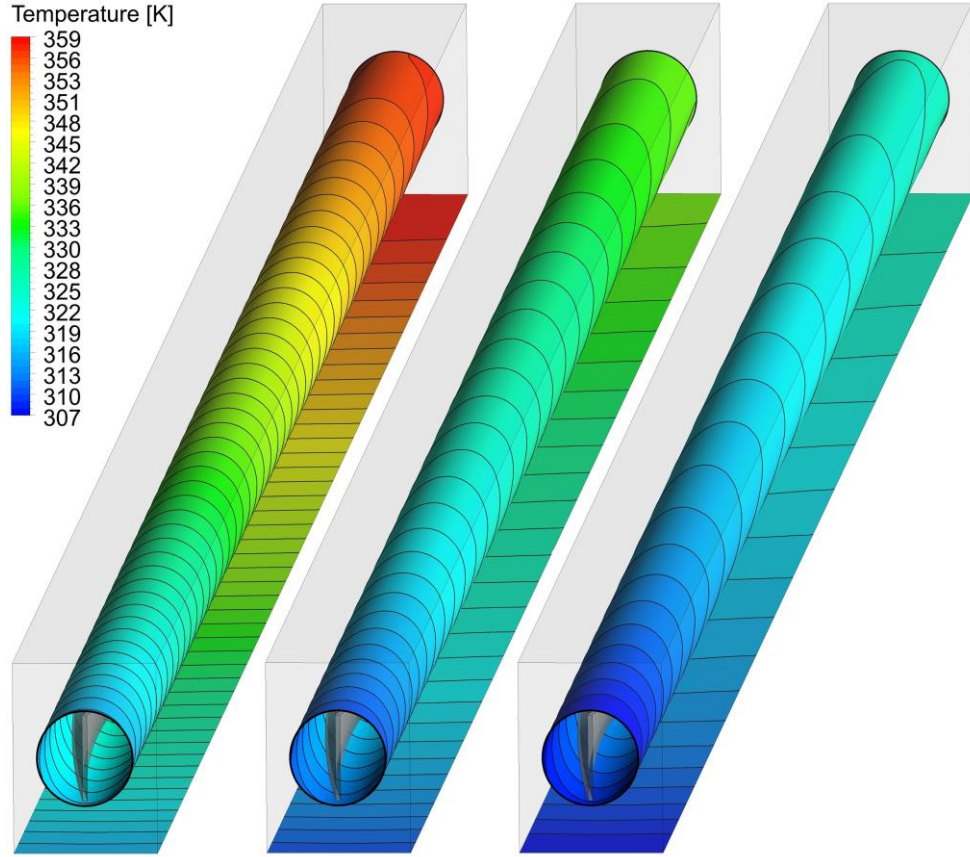

Figure 3.6 Temperature colour iso-levels on the heated surface and inner wall of MC-TT at $\phi = 0$. $Re =$100 (left), 200 (centre) and 350 (right).

Figure 3.7 presents the temperature distribution at four cross-sections in the x_1 plane at the Reynolds number of 300 and $\phi = 0\%$ of Al_2O_3 in MC-NT, MC-ST and MC-TT. The tape produces a band of elevated temperature that runs through the channel axis, flanked by two semi-circular areas of cooler flow. The elevated temperature band denotes the temperature of the solid tape. It is noted that the temperature of the tape increases from inlet to outlet, indicating axial heat transfer by conduction along the tape from the channel outlet to the inlet cooler inflow. In terms of the temperature distribution through the full x_1 planes, Figure 3.7 shows that the highest temperature occurs in MC-NT case. Conversely, the MC-TT shows the lowest temperature followed by MC-ST at the same Reynolds number. This improvement is attributed to the swirl flow induced by the twisted tape, which generates the secondary flow shown in Figure 3.10. This secondary flow helps to increase the velocity of the fluid near the channel wall and helps to reduce the thermal resistance. The Reynolds number dependence of the best cooling performance

configuration MC-TT is investigated next. Figure 3.8 shows the temperature distribution along four cross-sections in the x_1 plane, at Reynolds numbers between 100 to 350, using pure water as the working fluid in MC-TT. The results show that the temperature at the four cross-sections decreases by increasing the Reynolds number. The best cooling performance is achieved at the Reynolds number of 350.
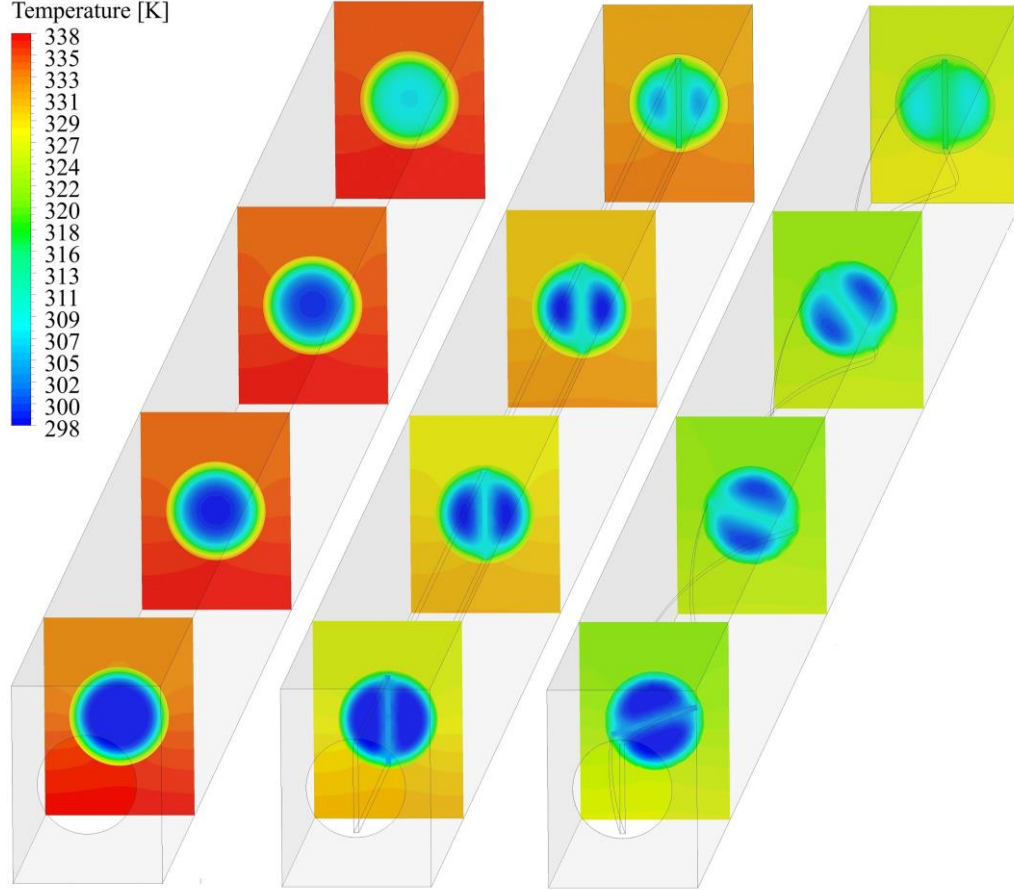

Figure 3.7 Colour iso-levels of temperature distributions for different cross-sections at $Re = 300$ and $\phi = 0$ of MC-NT (left), MC-ST (centre) and MC-TT (right).
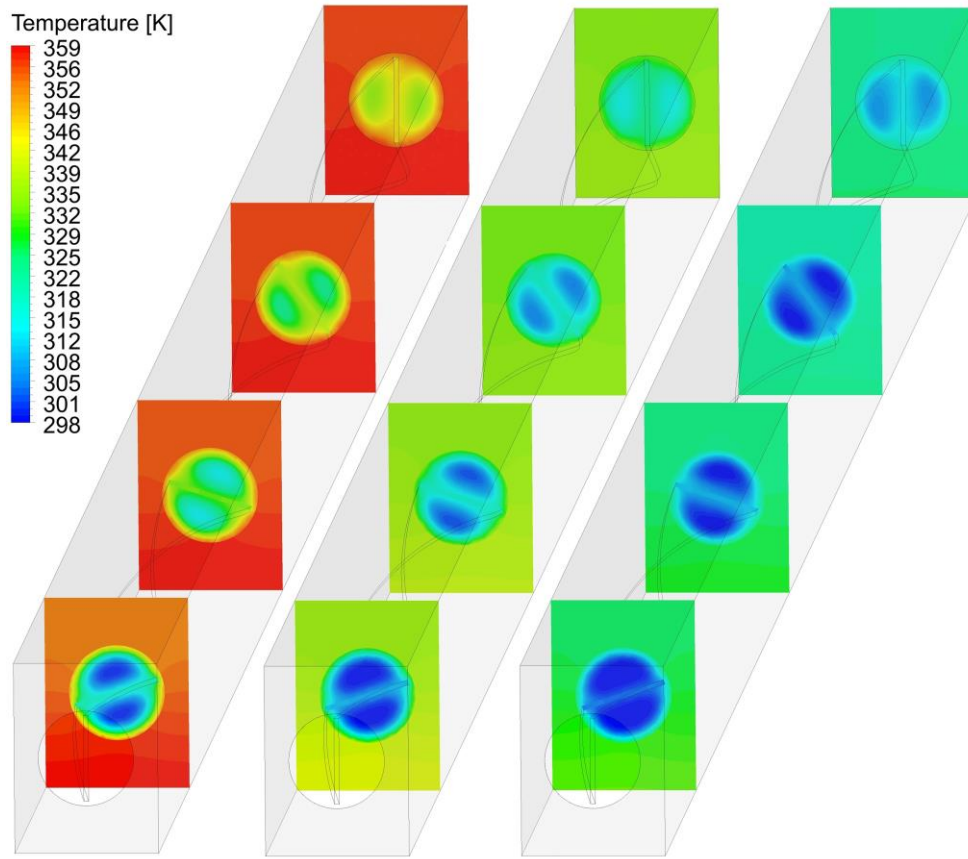
Figure 3.8 Colour iso-levels of temperature distributions for different cross-sections of MC-TT at $\phi = 0$. $Re = 100$ (left), 200 (centre) and 350 (right).

3.5.2 Effects of twisted tape on the flow pattern

Figure 3.9 shows the streamlines along MC-NT, MC-ST, and MC-TT at the Reynolds number of 350, with pure water as the working fluid. The streamlines are coloured by the flow velocity magnitude. Figure 3.9 shows that the streamlines through MC-NT and MC-ST follow almost the same path but the velocity magnitude through MC-ST is higher than through MC-NT. Adding the straight tape increases the flow blockage, by the growing boundary layers over the tape faces. This blockage generates higher axial velocity maxima away from the wall, to conserve the inlet volumetric flow rate. The streamlines along MC-TT change in direction and in velocity magnitude in comparison to MC-NT and MC-ST. The streamlines along MC-TT indicate a change from axial flow to swirl flow (vortex motion). The idea of inserting the twisted tape is to the increase in the microchannel heat sink internal wet surface area and generate swirl flow. These features are expected to be useful for enhancing the cooling performance of MC-TT compared to MC-NT and to MC-ST. However, inserting the twisted tape produces the highest flow resistance in comparison with MC-NT and MC-ST. This resistance raises both the pressure drop through the channel and the pumping power, as it will be presented later. The Reynolds

number dependence of the streamline pattern was investigated over the range of $100 \leq Re \leq 350$. These numerical results, omitted for brevity, indicated that changing Reynolds number gives substantially the same twisting streamline pattern, with the velocity along the streamline changing proportionally to the Reynolds number. The best cooling performance with strong swirl flow is achieved at the Reynolds number of 350, which provides the largest transport of heat by convection. The effect of increasing the volume concentration of Al_2O_3 nanoparticles was examined by modelling the same configurations with $\phi = 0, 1, 2,$ and 3%. These results, also omitted for brevity, indicate that the velocity magnitude marginally increases by adding more nanoparticles and that the highest velocity magnitude is reached at $\phi = 3\%$.
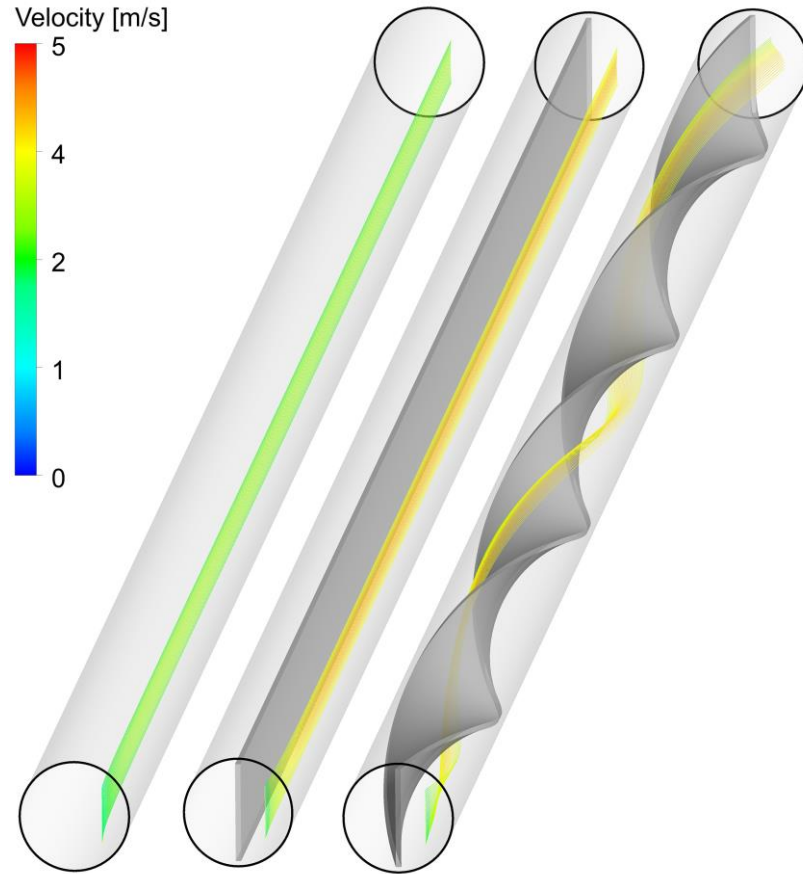
Figure 3.9 Streamlines at $Re = 350$ and $\phi = 0$ through MC-NT (left), MC-ST (centre) and MC-TT (right).

Figure 3.10 shows the velocity magnitude distributions by colour iso-levels on the x_1 plane 5 mm from the inlet of MC-NT, MC-ST and MC-TT. The black vectors in Figure 3.10 denote the in-plane velocity. The working fluid is pure water at the Reynolds number of 350. It is observed in this figure that the flow velocity is larger adjacent to the inner

wall for both MC-ST and MC-TT compared with MC-NT. The reason for this phenomenon is that the swirl flow made via the twisted tape helps the heat and mass transfer from the near-wall region to the centre of the tube, as discussed in the context of Figure 3.9. This swirl flow produces a secondary flow motion, which generates heat convection in the vertical and transverse directions. This provides higher homogeneous heating of the working fluid along the channel cross-section area compared to MC-ST.

Figure 3.11 shows the corresponding distributions of in-plane velocity magnitude in MC-TT at Reynolds numbers between 100 to 300 with $\phi = 3\%$ of Al_2O_3 nanoparticles. The results show that both the velocity magnitude and the in-plane velocity magnitude increase with increasing the Reynolds number. This increase in flow velocity is expected to decrease the thermal resistance by providing more convection near the walls of the microchannel MC-TT. The highest flow velocity is predicted at the Reynolds number of 350. The effect of increasing the volume concentration of Al_2O_3 nanoparticles was explored by modelling the same configurations with $\phi = 0$, 1, 2, and 3%. The numerical result predicted marginally higher flow velocity magnitude and in-plane velocity magnitude by adding more nanoparticles to the working fluid
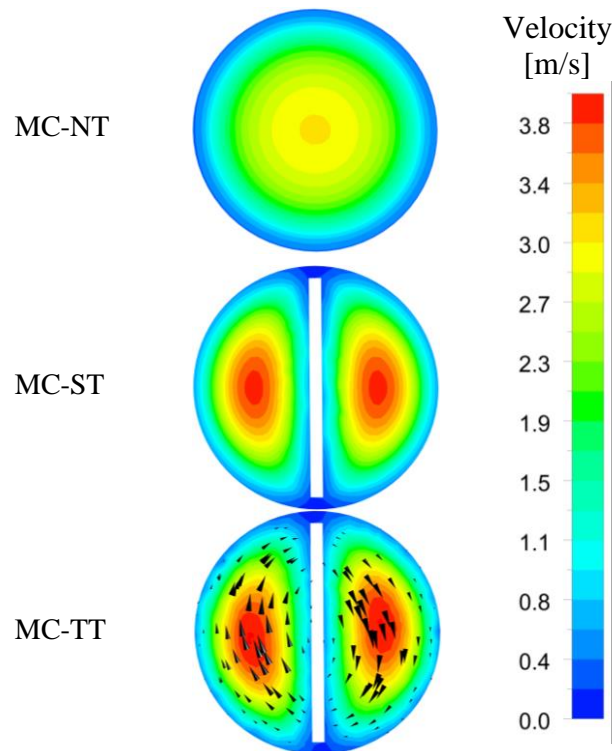

Figure 3.10 Colour iso-levels of velocity magnitude and in-plane velocity vectors at $Re = 350$ and $\phi = 0$ of MC-NT, MC-ST, and MC-TT in the $x_1 = 5$ mm plane, viewed from the inlet.
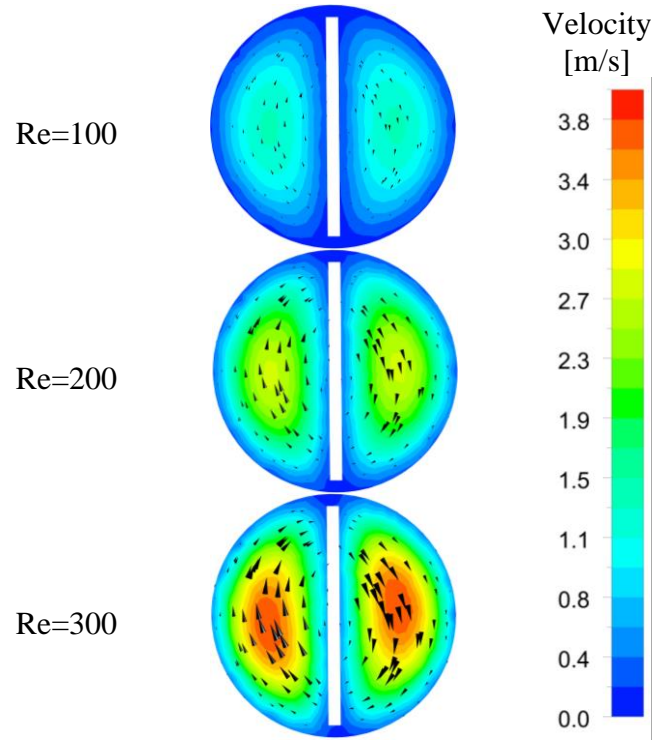
Figure 3.11 Colour iso-levels of velocity magnitude and in-plane velocity vectors at ϕ =3% of MC-TT at $Re = 100$, 200 and 300 in the $x_1 = 5$ mm plane, viewed from the inlet.

3.5.3 Effects of twisted tape on thermal characteristics

Figure 3.12 shows the change in the Nusselt number with Reynolds number in the MC-TT, MC-ST, and MC-NT with $\phi = 0$, 1, 2, and 3% of Al_2O_3 nanoparticles. The Reynolds number ranges from 100 to 350. There is a significant increase in the Nusselt number for the MC-TT compared to MC-NT. The straight tape offers a better thermal performance as compared to MC-NT, in particular at lower Reynolds numbers, where the performance gain is greater. This can perhaps be attributed to the axial heat transport by conduction along the tape, which at lower Reynolds numbers helps to bring heat from near the channel outflow to near the channel inflow. At the lower Reynolds numbers, the outflow coolant temperature is higher, as shown in Figure 3.7, due to the longer residence time of the coolant through the channel. Therefore, near the outlet, the temperature difference with the surrounding walls is more modest and this is not conducive to good heat transfer to the working fluid. At these conditions, it is advantageous to transport heat close to the inlet, where the lower coolant temperature gives a comparatively greater heat transfer rate. This is consistent with the trend shown in Figure 3.12 at $Re = 100$, where the Nusselt number of the MC-ST is well above that of MC-NT. At higher Reynolds numbers, the temperature difference between the inlet and the outlet of the coolant is more modest, and so are the benefits of moving heat towards the channel inlet, by conduction

through the tape, reduce. This is shown by the lower difference in Nusselt number between MC-ST and MC-NT at increasing Reynolds numbers in Figure 3.12. The addition of a twisted tape insert is beneficial in further increasing the thermal performance of the microchannel.

The Nusselt number was also found to increase by increasing both the Reynolds number and the volume concentration of the nanoparticles. The Nusselt number of MC-ST is observed in Figure 3.12 to exhibit a different trend compared to MC-NT and MC-TT and this is consistent with the average bottom wall temperature of MC-ST having a different trend compared to MC-NT and MC-TT, as seen in Figure 3.14. The effect of increasing the volume concentration of Al_2O_3 nanoparticles was evaluated by modelling the same configurations with $\phi = 0, 1, 2,$ and 3%. A useful increase in Nusselt number is achieved by increasing the volume concentration of nanofluid. Adding an excess loading of nanoparticles into the fluid can increase its viscosity, which can have a negative result on heat transfer (Wongcharee and Eiamsa-ard, 2012). This effect was not observed in the current study, due to the volume concentrations of the nanoparticles used is lower than the concentrations at which this negative result was observed in (Wongcharee and Eiamsa-ard, 2012). The biggest improvement in Nusselt number, compared to MC-NT, was 39.73%, obtained with the MC-TT at $\phi =$ 3% and Reynolds number of 350.
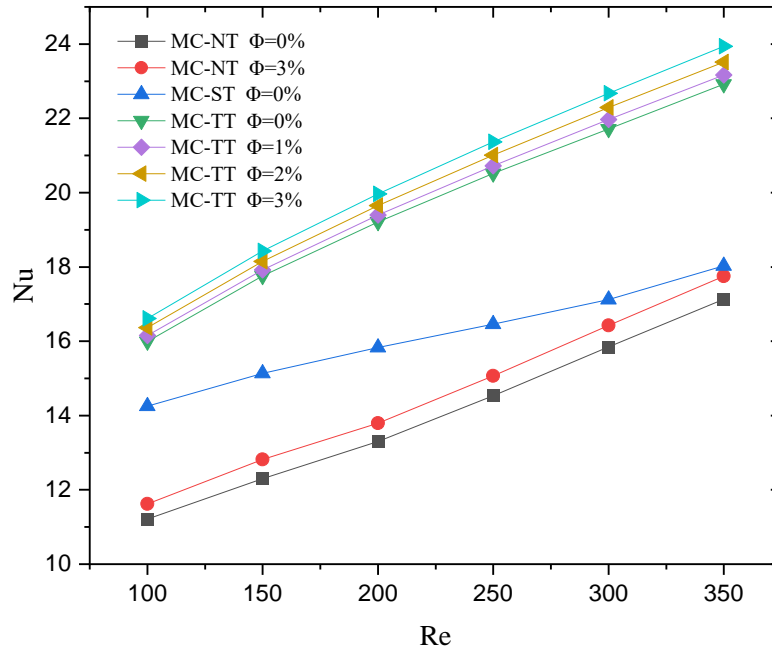

Figure 3.12 Nusselt number as a function of Reynolds number for MC-TT, MC-ST and MC-NT at different concentrations of Al_2O_3 nanoparticles.

Another way of expressing the heat transfer performance of different configurations is by evaluating the thermal resistance. Figure 3.13 illustrates the total thermal resistance as a function of Reynolds number for MC-TT, MC-ST, and MC-NT at ϕ = 0, 1, 2, and 3% of Al_2O_3 nanoparticles. These numerical results show that the total thermal resistance is lower in MC-TT compared to the one in MC-NT, because of the increase in thermal transport between the channel wall and the fluid. This improvement is due to an increase in wetted wall surface area and due to the generation of secondary flow by the twisted tape, as seen by Figure 3.10. The friction factor with swirl flow is greater than that for axial flow. The total thermal resistance decreases by increasing the Reynolds number. The greatest decrease in total thermal resistance is predicted at a Reynolds number of 350 and is 37.54% less than in the MC-NT configuration.
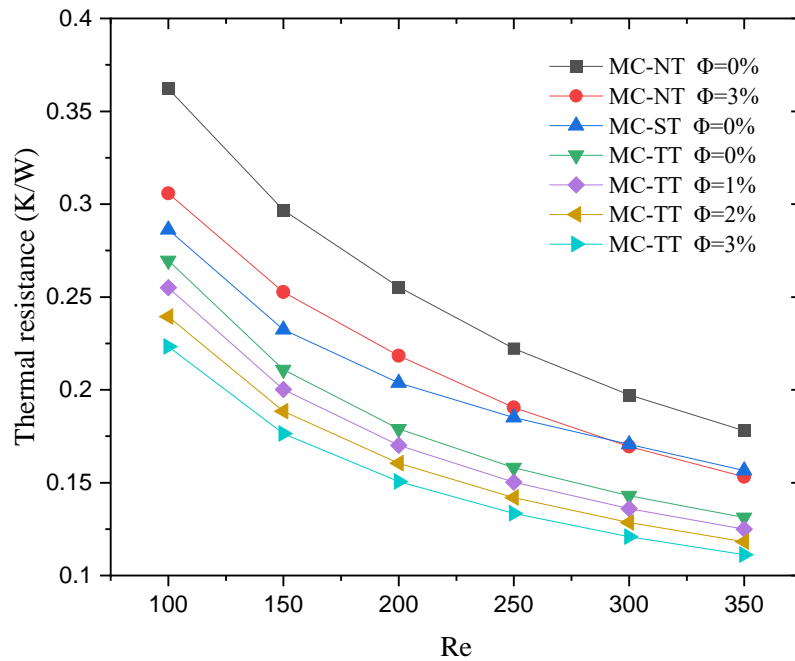
Figure 3.13 Total thermal resistance as a function of Reynolds number for MC-NT, MC-ST, and MC-TT at different concentrations of Al_2O_3 nanoparticles.

The bottom wall temperature has a particular significance for assessing the thermal performance of the microchannel heat sink, for applications to micro-electronic devices. For any given heat transfer rate input load to the heat sink, the lowest interface wall temperature is desirable for preserving the life of the electrical components. Figure 3.14 shows the difference between the average bottom wall temperature and the inlet temperature of MC-TT, MC-ST and MC-NT at various states. Figure 3.14 shows that the average bottom wall temperature decreases by increasing the Reynolds number in all cases. Moreover, inserting the straight tape gives a lower bottom wall temperature than

MC-NT at the same Reynolds number. Using a twisted tape in the MC-TT configuration is predicted to further reduce the bottom wall temperature, compared to MC-ST. Increasing the volume concentrations of the nanoparticles at the same Reynolds number is shown to produce lower bottom wall temperatures than by using pure water in all configurations. This agrees with the finding in Figure 3.12, where an increase in the Nusselt number is reported by increasing the volume concentration of nanoparticles over the range ϕ = 1, 2 and 3% of Al_2O_3 nanoparticles. The lowest average bottom wall temperatures for a given coolant inflow temperature are achieved in the MC-TT and MC-ST under the condition of Reynolds number of 350 and ϕ = 3% of Al_2O_3 nanoparticles. These temperatures are 10.5 °C and 3.35 °C lower than with the MC-NT, modelled at the same conditions.
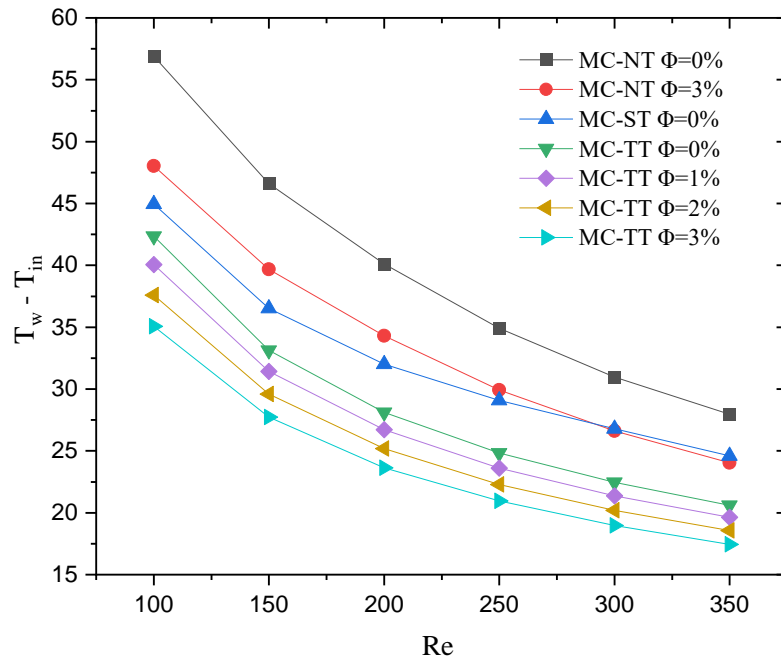
Figure 3.14 Average bottom wall temperature of MC-TT, MC-ST, and MC-NT at different values of Reynolds number Re and of nanoparticle volume fraction ϕ.

3.5.4 Effects of twisted tape on hydraulic characteristics

Figure 3.15 and Figure 3.16 show the changes in the pressure drop and in the pumping power with Reynolds number for MC-TT, MC-ST and MC-NT. The effect of using pure water and ϕ = 1, 2 and 3% of Al_2O_3 nanoparticles are also documented. The MC-TT exhibits the highest pressure drop compared to MC-NT and MC-ST. This high pressure drop causes a correspondingly high pumping power demand, as shown in Figure 3.15. This high pressure drop is a consequence of the higher flow resistance due to the reduction in the hydraulic diameter D_h from inserting the tape and due to greater blockage from

twisting the tape. Specifically, the bulk motion of the fluid flow in x_1, driven by the pressure drop Δp, is turned into swirl flow moving about the twisting tape and this generates secondary flow motion. It is interesting to observe that, over the Reynolds number range $100 \leq Re \leq 350$, the solid blockage contribution due to the tape, represented by the pressure drop difference between MC-ST and MC-NT, is larger than that due to the tape twist, represented by the pressure drop difference between MC-TT and MC-ST. Introducing twist in the tape appears to produce a modest additional penalty in pressure drop, according to Figure 3.15, while delivering appreciable thermal performance gains, according to Figure 3.12. Consequently, the pumping power required by configuration MC-TT is only marginally higher than that required by configuration MC-ST but well above that of the microchannel with no tape, as shown by Figure 3.16. Figure 3.16 shows that, with $\phi = 0\%$ and at the Reynolds number of 350, the predicted pressure drop of MC-TT increases by 100.29% with respect to Δp MC-NT. This pressure drop is comparable with the one reported in other studies that used twisted tapes inserted in large channels. Yadav and Padalkar (2012) reported an increase in pressure drop of between 203 to 623% when they applied a full twisted tape compared to the same geometry without twisted tape.

Figure 3.15 and Figure 3.16 also show that the pressure drop and the pumping power increase using nanofluids compared to using pure water, with the losses being higher at higher nanoparticle volume concentrations. This increase in pressure drop and pumping power is due to the increased density and viscosity of the nanofluids, according to equations (2.3) and (2.6). A similar trend was observed by Mashayekhi et al. (2018) in their numerical study using hybrid Al_2O_3-CuO nanofluids with 0 to 2% volume concentrations. The MC-TT with Al_2O_3 nanofluids at a volume concentration of $\phi = 3\%$ was found to give the highest pressure drop and pumping power requirement, the predicted pressure drop and pumping power of MC-TT increase by 47.74% and 66.27% for Δp and P_p MC-NT at the Reynolds number of 350 and $\phi = 0\%$, respectively. A similar trend was observed by Mashayekhi et al. (2018) in their numerical study using hybrid Al_2O_3-CuO nanofluids with 0 to 2% volume concentrations. The MC-TT with Al_2O_3 nanofluids at a volume concentration of $\phi = 3\%$ was found to give the highest pressure drop and pumping power requirement, the predicted pressure drop and pumping power of MC-TT increase by 47.74% and 66.27% for Δp and P_p MC-NT at the Reynolds number of 350 and $\phi = 0\%$, respectively.

Figure 3.15 Pressure drop as a function of Reynolds number for MC-TT, MC-ST, and MC-NT at different concentrations of Al₂O₃ nanoparticles.
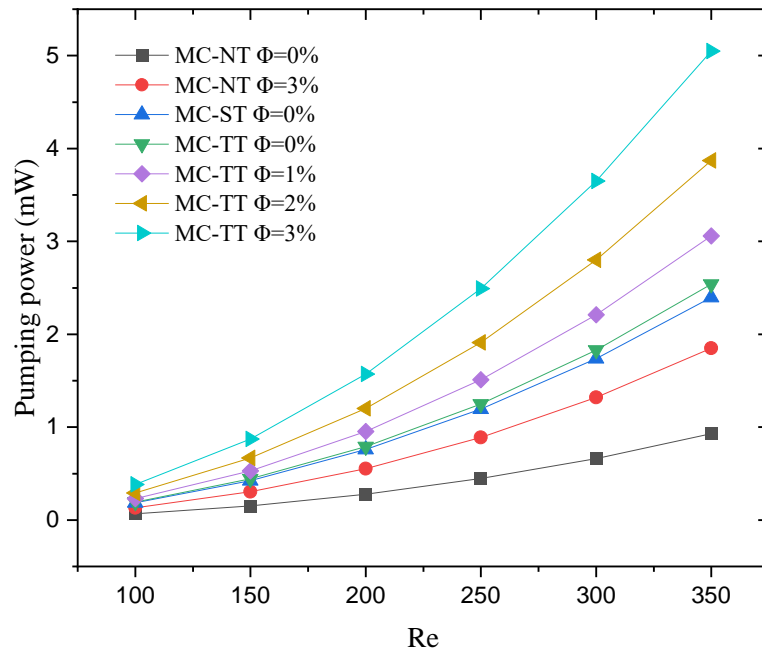
Figure 3.16 Pumping power as a function of Reynolds number for MC-TT, MC-ST, and MC-NT at different concentrations of Al₂O₃ nanoparticles.

Another way of evaluating the hydraulic performance at different configurations is through the friction factor f. Figure 3.17 shows the friction factor computed from the MC-TT, MC-ST, and MC-NT configurations. Consistently with Figure 3.15 and Figure 3.16, MC-TT has the highest friction factor compared to MC-NT and MC-ST. This is consistent

with Figure 3.15 since the friction factor is a non-dimensional form of pressure drop. It represents the loss in flow kinetic energy by friction and by the secondary flows induced by the twisted tape. Conversely, MC-NT has the smallest friction factor among all configurations tested at the same conditions, which is due to its smallest wetted wall surface area and mainly in axial (x_1) flow. Figure 3.17 shows that the friction factor decreases by increasing the Reynolds number and this trend is almost consistent for all configurations. Moreover, the numerical results in this instance predicted that the MC-TT with nanofluids showed a higher friction factor compared to pure water due to the increase in viscosity and density of the working fluid at higher nanoparticle concentrations, according to equations (2.3) and (2.6). Under the condition of $\phi = 0\%$ and Reynolds number of 100, the friction factor with MC-TT and with MC-ST is 81.08% and 78.92% higher than with MC-NT, respectively.
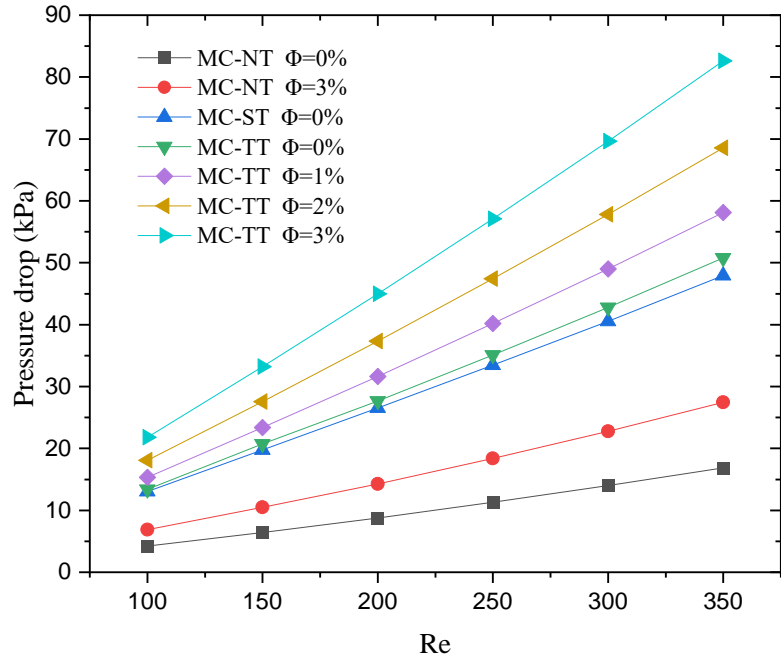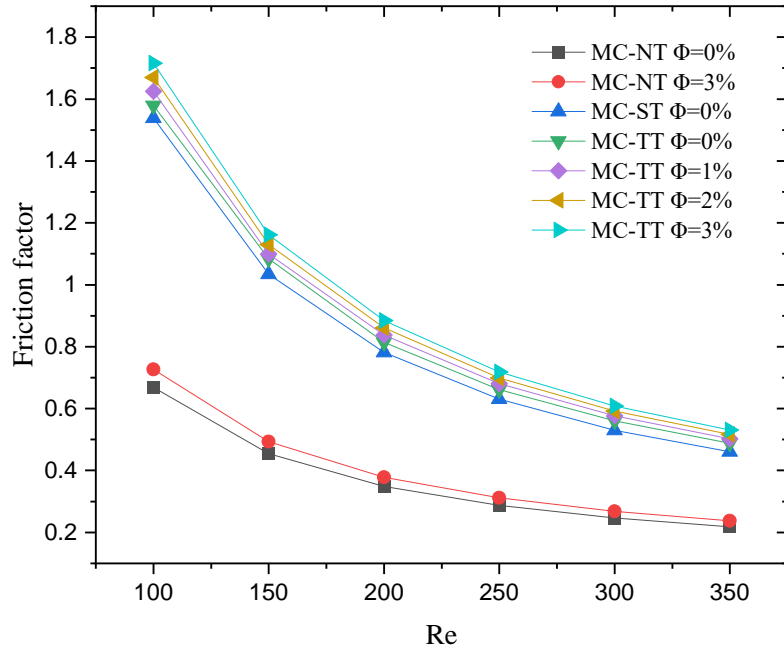

Figure 3.17 Friction factor as a function of Reynolds number for MC-NT, MC-ST, and MC-TT at different concentrations of Al_2O_3 nanoparticles.

Figure 3.18 aggregates the Figure of Merit (FoM) from MC-NT, MC-ST and MC-TT modelled at different Reynolds numbers and with different nanoparticle concentrations. FoM is referenced to the performance of MC-NT modelled with pure water at each Reynolds number. The results show that all FoM values for MC-TT are above one. This means that the microchannel with the twisted tape provides a better thermal performance at the same flow resistance cost. This higher FoM points towards the MC-TT having the potential for better energy efficiency. Figure 3.18 shows that FoM for MC-TT increases

45

by increasing the Reynolds number up to a Reynolds number of 200, after which it decreases due to more friction. Therefore, the best FoM for MC-TT is achieved at the Reynolds number of 200. Moreover, a marginally higher FoM is achieved by adding more nanoparticles to the nanofluids. Conversely, MC-ST has a FoM lower than one, which means the straight tape gives more flow resistance penalty than heat convection gain to the microchannel heat sink, which results in more friction and more pressure drop, according to Figure 3.15 and Figure 3.17.
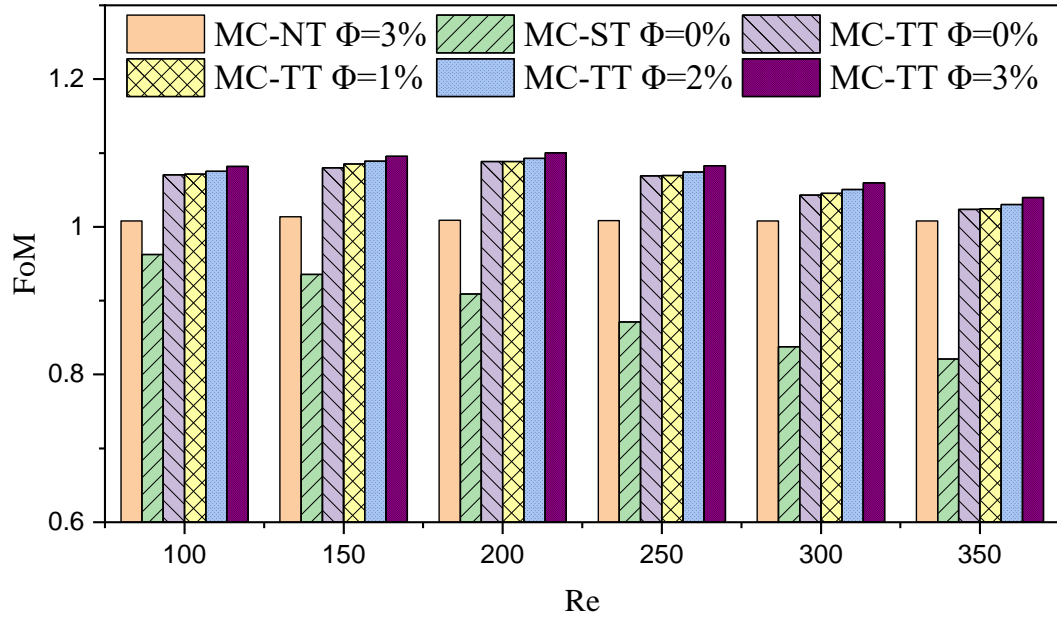
Figure 3.18 The FoM of MC-NT, MC-ST and MC-TT, modelled at different Reynolds numbers and with different nanoparticle volume fractions.

3.5.5 Exergy and field synergy characteristics of the microchannel heat sink

Figure 3.19 shows the rate of exergy destruction through the microchannel over the Reynolds number range 100 to 350. All microchannels show a downwards trend in exergy destruction rate with increasing Reynolds number, driven by the lowering of the microchannel base temperature at increasing Reynolds number. Specifically, lowering T reduces $\left(1 - \frac{T_r}{T}\right)$ in Equation 2.19 and hence $\dot{E}_{xd}$. This appears to be the leading term in evaluating the exergy destruction rate, with only a second-order contribution from Equation 2.20 that accounts for the exergy inflow transported by fluid. The microchannel with the twisted tape at the highest Reynolds number is the configuration that achieves the least rate of exergy destruction, by its lowest base wall temperature.
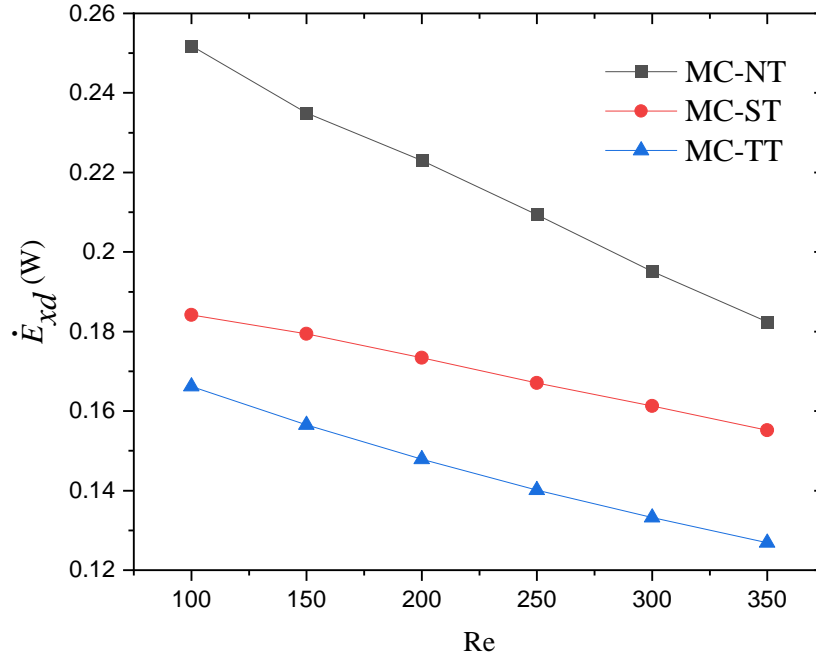
Figure 3.19 The exergy destruction rate for MC-NT, MC-ST and MC-TT at $\phi = 0\%$.

Figure 3.20 shows the exergy expenditure rate and the trends for all three microchannels are non-monotone. The rate of exergy supplied by the heated base reduces with reducing base temperature, since lower grade heat is supplied at this reduced temperature. This generates a reducing trend in exergy expenditure at Reynolds numbers below 200 for all three microchannels. Frictional losses are thought to be responsible for a subsequent rise in exergy expenditure rate at higher Reynolds numbers, which is more pronounced in the simulations with the microchannel with straight and twisted tapes, as shown by the steeper positive gradients of $d\dot{E}_x/dRe$ of these configurations than with the circular microchannel with no tape. Still, over the Reynolds number range explored in this work, the exergy expenditure rates of the microchannels with tape remain below that of the baseline geometry without tape.
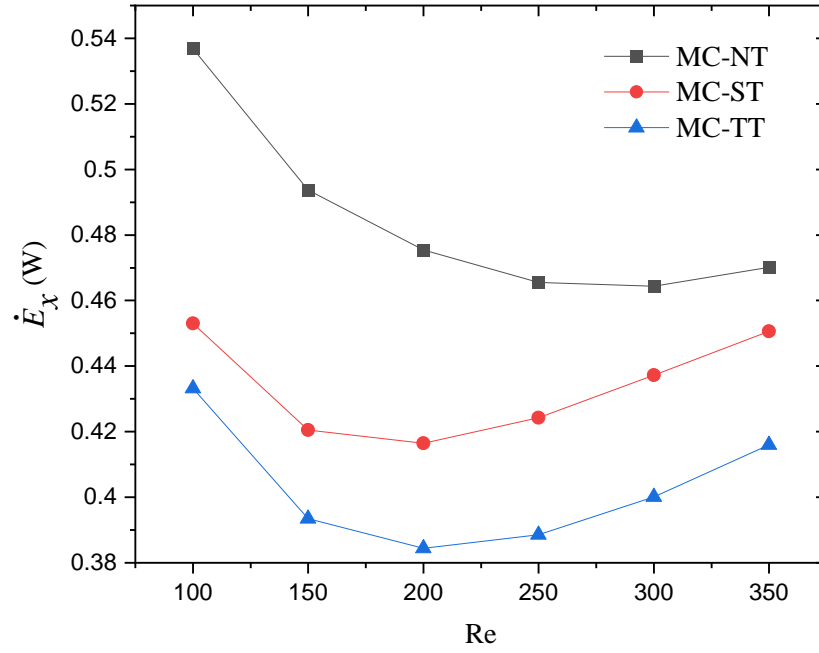
Figure 3.20 The exergy expenditure rate for MC-NT, MC-ST and MC-TT at $\phi = 0\%$.

The compound effect of the exergy expenditure and destruction rates is evaluated in terms of the second law efficiency η_{II} in Figure 3.21. Inserting a tape in the circular microchannel gives a second law efficiency gain of up to 7% with a straight tape and of up to 10% with a twisted tape. Over the range $100 \leq Re \leq 200$, the microchannels with twisted tape deliver η_{II} values around 60% and these are to the ones from a circular microchannel with fins modelled in Liu et al. (2019), notwithstanding a different definition of $\dot{E}_x$ used in Liu et al. (2019). Above $Re \sim 200$, the microchannels with twisted tape are predicted to enable higher values of η_{II} to be reached, approaching 70% for the microchannel with the twisted tape. It is possible that this gain can be ascribed to the twisted tape generating an orderly secondary flow with a dominant clockwise motion, which may be as effective in convecting heat away from the wetted walls and towards the middle of the microchannel as alternative turbulence-generator-like features, but with less viscous dissipation.
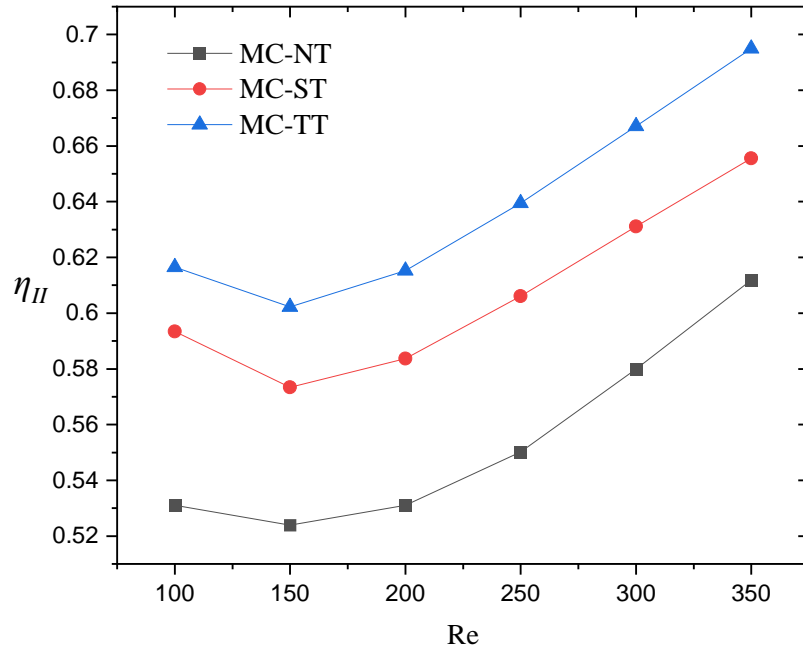
Figure 3.21 The second law efficiency for MC-NT, MC-ST and MC-TT at $\phi = 0\%$.

Figure 3.22 shows that the volume averaged synergy angle $\bar{\theta}$ for the microchannels without tape and with a straight tape is below approximately 7 degrees. These straight channels are characterised by a nearly axial flow that is aligned with the axial pressure gradient, from inlet to outlet. This alignment maximised the work rate performed per unit volume by the imposed axial pressure field on the flow, according to Equation 2.24. The inlet length in these microchannels, where the wall boundary layer develops, is probably the only region of divergence between the near-wall velocity vector and the axial pressure gradient. The straight tape divides the inflow cross-section, providing two separate channels of lower hydraulic diameter. This would reduce the inlet length over which the boundary layer grows and is consistent with the straight tape microchannel $\bar{\theta}$ being lower than the corresponding value without a tape, indicating a more axial flow. The twisted tape induces a bulk clockwise rotation so that the velocity vector diverges from the dominant axial pressure gradient. This increases $\bar{\theta}$ with respect to the other two geometries, indicating that less work being expended to generate this flow motion.
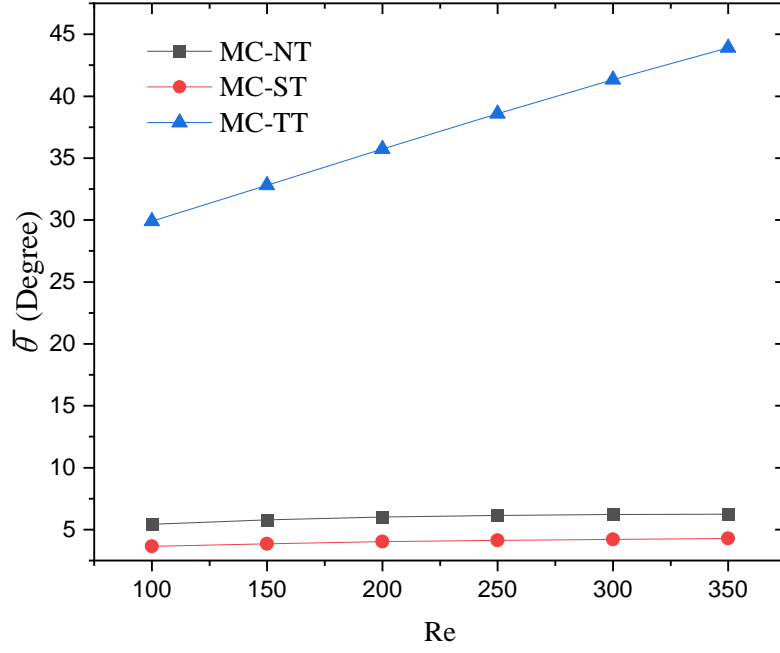
Figure 3.22 The synergy angle $\bar{\theta}$ MC-NT, MC-ST and MC-TT at $\phi = 0\%$.

There is modest synergy between the velocity vector and the temperature gradient field, as shown in Figure 3.23, where the volume-averaged synergy angle between these two vector fields is approximately 89 degrees, for all microchannel configurations. The desirable condition of $\bar{\beta} \rightarrow 0$ is not achieved, mainly due to the inlet heat flux vector $\dot{q}_2$ being imposed normal to the bulk flow axial direction. The range covered by the $\bar{\beta}$ angle from the different microchannel configurations is relatively modest, $89° \leq \bar{\beta} \leq 90°$. The $\bar{\beta}$ synergy angle for the microchannel with no tape ranges between $89.5°$ and $89.7°$ and it is in good agreement with $\beta \simeq 89.6°$ predicted in Liu et al. (2019) for a similar circular microchannel configuration over the wider Reynolds number range $200 \leq Re \leq 1500$. The new predictions extend to lower Reynolds numbers and show a decreasing trend for $\bar{\beta}$, indicating the possible onset of an operational regime that is more favourable to the synergy between the temperature gradient and the velocity fields.
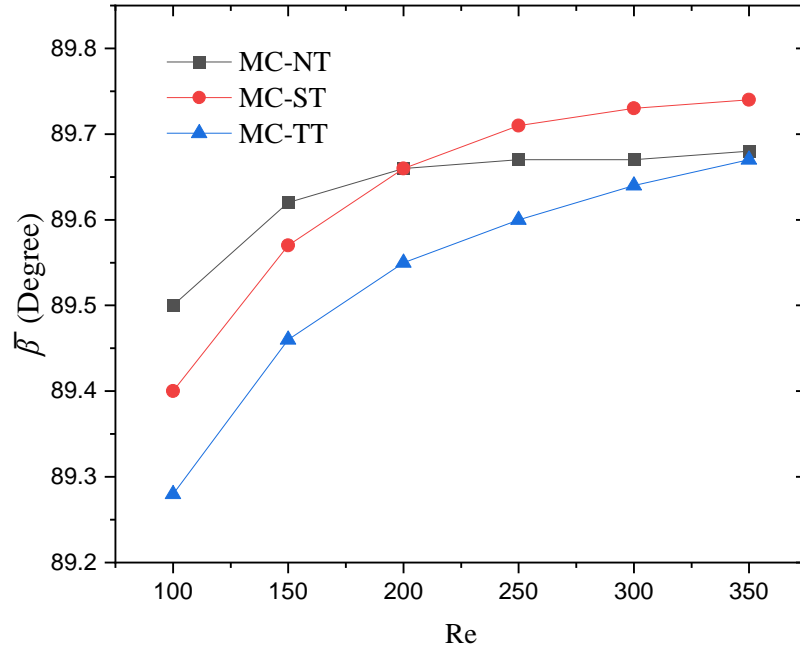
Figure 3.23 The synergy angle $\bar{\beta}$ MC-NT, MC-ST and MC-TT at $\phi = 0\%$.

3.6 Conclusions

The benefits of using a twisted tape to enhance the heat transfer performance in industrial heat exchanger pipe banks prompted the first numerical investigation on whether this technique can be adapted to microchannels. This work has made the first attempt at applying twisted tape inserts to a circular microchannel heat sink running Al_2O_3 nanofluid coolant.

A purpose-built numerical model of a generic heat exchanger was formulated and validated, which allowed the thermo-hydraulic performance of the system to be explored in some detail. A three-dimensional single-phase flow model was used, covering the Reynolds number range $100 \leq Re \leq 350$ at volume fractions of $\phi = 0$, 1, 2 and 3% of Al_2O_3 nanoparticles.

Within the range of microchannel geometry and flow parameters explored in this study, the twisted-tape configuration run at the Reynolds number of 350 and with $\phi = 3\%$ of Al_2O_3 nanoparticles achieved an average bottom wall temperature 10.5 K below that of the equivalent circular microchannel without tape running pure water at the same Reynolds number. Such decrement in temperature is attractive for heat sink type implementations in modern multi-core liquid-cooled computer clusters. It provides additional power growth capacity for computer chips and/or additional margin against overheating. Both elements enable more capable and longer lifespan electronics.

Using a straight tape also lowers the average bottom wall temperature compared to the equivalent circular microchannel without a tape, but to a less extent than with a twisted tape. This provides evidence of two processes concurring to the performance of the tape, which are heat conduction along the tape, which assists with heating the cold coolant inflow near the inlet, and enhanced heat convection by the coolant flow rotating about the microchannel axis, that adds an azimuthal velocity component and provides higher velocity magnitude on approach to the wall. The induced swirl is orderly and rotationally one-handed, potentially dissipating less kinetic energy than flow trips or turbulators that typically generate a more varied vorticity field. This is consistent with the lower exergy expenditure and destruction rates associated to this geometry, compared to the other modelled configurations, which enable the twisted tape microchannel to remove heat at a higher second law efficiency η_{II}.

The new microchannel twisted tape design at the Reynolds number of 350 has a clear thermal performance advantage over the microchannel with no tape, with a 40% higher Nusselt number and a 37% lower thermal resistance. It incurs in double the pressure loss of the channel with no tape and the balance between thermal performance gain and friction loss provided by the Figure of Merit indicates the twisted tape being best performing at the Reynolds number of 200 with 3% of Al_2O_3 nanoparticles. Most of the performance advantage appears to come from the geometry rather than from the use of the nanoparticles.

The thermal performance advantage from using a tape in a microchannel heat sink is comparable to that from other known shape modifications, such as polygonal cross-section, Y fins, and cross-channels. The orderly clockwise motion and a judicious lumen to cross-section perimeter ratio can deliver modest pumping power requirements to the microchannel with tape compared to some of these documented designs, which is an advantage. However, as the tape bisects the circular cross-section, the two narrower passages can become obstructed by any clog half of the size of what would clog the channel without tape, which is a disadvantage.

This work is therefore of practical use, as it has provided proof of concept for the application of twisted tapes to microchannel heat sinks. It has also shed light on the heat and mass transfer mechanisms underpinning this performance, which can be exploited for investigating more sophisticated and performing microchannel heat exchangers.

Chapter 4: Numerical investigation of various twisted tapes enhancing a circular microchannel heat sink performance

4.1 Introduction

Many micro-devices, such biomedical and micro-electronic circuits, chemical reactors, and micro-electro-mechanical systems, produce heat as they operate (Alfaryjat et al., 2019). Therefore, suitable cooling processes are essential to running these micro-devices. Dissipating the high heat flux through these devices is a technological challenge that has motivated the development of different technical solutions, such as jet impingement cooling, spray cooling, micro heat pipes, thermoelectric coolers, and microchannel heat sinks (Kandlikar and Bapat, 2007). The research community is currently active in exploring means for improving the cooling performance of microchannel heat sinks. These are liquid cooled heat sinks that have several parallel channels to provide a large contact area between the heat sink surface and the coolant that runs through them. Kandlikar and Grande (2003) termed the heat sinks with channel hydraulic diameters ranging between 10 μm and 200 μm as microchannel heat sinks. Microchannel heat sinks can provide effective cooling in challenging, high heat flux dissipation problems from the electronics industry, for medical, energy, nuclear, military and defence, automotive and aerospace applications. Examples include high power laser diode arrays, microelectronic devices, refrigeration and cryogenic systems, catalytic reactors, solar cells, and fuel cells (Deng et al., 2021).

An array of microchannel cooling passages can be carved into a matrix made from a thermally conducting material. How the matrix material choice affects the overall thermal performance was explored by testing heat sinks made in copper (Kleiner et al., 1995), aluminium (Choquette et al., 1996), bronze (Gamrat et al., 2005), silicon (Zhimin and Fah, 1997), stainless steel (Peng et al., 1994b), and glass (Koşar, 2010). The matrix material choice was observed to be more significant in channels of larger height. Sub-millimetre lower high channels, for which the overall thermal performance is less sensitive to the matrix material choice, often use silicon as opposed to aluminium or copper. Silicon provides a lighter heat sink, which is desirable in light-weight electronic applications. The flow and heat transport through microchannel passages depends on the coolant type. The performance of various coolants has been studied, including that of water, methanol (Peng et al., 1994b), other refrigerants (Zhuan and Wang, 2013), and of nanofluids (Mohammed

et al., 2011a). Gaseous coolants, including air (Kleiner et al., 1995), argon, helium, nitrogen (Harley et al., 1995), and ammonia (Adham et al., 2012), were also used. The most used coolants are water and air, owing to their low cost and wide availability. Liquid coolants are a useful alternative to gaseous coolants in applications where gaseous coolants are unable to meet the cooling demand.

The performance of microchannel heat sinks is documented at laminar and turbulent flow conditions. A few studies made use of both types of flow conditions (Tunc and Bayazitoglu, 2002). The studies that exploited laminar flow conditions feature more in the literature. Their popularity is due to the flow through the narrow bore channels being most often naturally laminar. The channels are also short, so that turbulence is unable to develop over the short channel length (Mohammed Adham et al., 2013). Microchannel heat sinks have the potential to dissipate heat well (Jang and Choi, 2006), to provide a nearly uniform heated wall temperature distribution (Deng et al., 2021), they can be easy to implement (Bhandari and Prajapati, 2021), and can have a low power consumption. This potential is not achieved in typical microchannel heat sinks with a parallel and straight layout, which can feature high power consumption, a large temperature gradient, and poor heated wall temperature uniformity. Hence, the hydrothermal performance of conventional microchannel heat sinks must be improved. It is possible to achieve this by shape and structural optimisations of the microchannel, for instance, by using different microchannel cross-sectional shapes (Wang et al., 2016, Jing and He, 2019, Barba et al., 2006), groove and fins on the channel wall (Chai et al., 2018, Chai et al., 2019, Ali et al., 2021a), a vortex generator (Awais and Bhuiyan, 2018, Lu and Zhai, 2019, Wu and Tao, 2008), or a biomimetic tree-like design (Jing et al., 2020, Mondal et al., 2014).

Wang et al. (2016) studied numerically the effect of the channel cross-section shape on the microchannel heat sink thermal performance. They modelled channel cross-sections in the shape of a rectangle, of a triangle, and of a trapezium. Their numerical predictions show that the rectangular cross-section provides the highest thermal performance, while the triangular cross-section provides the lowest one, among the three shapes. Ali et al. (2021a) performed conjugate heat transfer simulations of microchannel heat sinks using discrete finite-volumes. They evaluated the effects of twisted and zigzag fin inserts into a plain rectangular microchannel. They determined that the twisted fin improved the cooling efficiency, whilst the zigzag fin delivered the best thermal performance. Wu and Tao (2008) numerically examined the thermal characteristics of a

rectangular microchannel that featured a longitudinal vortex generator. They reported that the longitudinal vortex generator was able to enhance the thermal performance of this type of heat sink. Chen and Cheng (2005) investigated microchannel heat sinks with biomimetic tree-like shapes. Their study identified tree-shaped channels able to boost the thermal performance, mainly due to a coolant perfusion effect into the solid matrix that is provided by the channel tree-like network, which mimics blood perfusion in a biological tissue. Alternative approaches to changing the coolant path through a rectangular cross-section microchannel is by making the path wavy (Mohammed et al., 2011b) or by tapering the channel (Hung and Yan, 2012a). These changes improve the overall thermal performance or lower the heat sink thermal resistance. However, it was observed that these enhancements come at the cost of a higher pumping power.

Larger flow devices, such as industrial heat exchangers, have been modelled and tested with swirl flow generators inserted in their pipes. Swirl flow generators are passive devices that enhance flow mixing at a low pressure drop cost, to improve the heat transfer rate. Twisted tapes have been used as swirl generators in heat exchangers (Alam and Kim, 2018). As the coolant is driven past a twisted tape, the tape imparts a swirl motion to the coolant. This induced swirl velocity disturbs the thermal boundary layer over the coolant channel walls and promotes flow mixing. This results in a higher heat transfer coefficient than in a circular channel without any twisted tape (Ponnada et al., 2019). The interest by the research community in this concept is evidenced in the reviews on it from Deng et al. (2021), Webb et al. (2005), Manglik and Bergles (2003), and Varun et al. (2016). Several variants to having a single, uninterrupted tape running through the full channel length have been explored, such interrupting the tape with axial gaps, adding tape pitch angle steps along its length, alternating between a clockwise and an anti-clockwise tape pitch along its length, varying the tape pitch, adding fringe cuts to the tape, using a twisted tape with centre wings on alternate axes, and using wire nails in the twisted tapes.

He et al. (2018) documented the effect of inserting a twisted tape on the friction factor and on the heat transfer of cross-flow air heaters. Their study confirmed that the flow swirl increases the heat transfer compared to a purely axial flow, at the cost of a higher the pressure drop in the resulting turbulent flow. Eiamsa-Ard et al. (2015) examined the trade-off between the heat transfer gain and the pressure loss from running between one and three twisted tapes in a corkscrew pattern through a pipe. Their experiment shows that one twisted tape filament in a corkscrew pattern gives the best trade-off. The use of

multiple twisted tapes to improve the heat transfer in a pipe was studied experimentally by Eiamsa-ard (2010), Bhuiya et al. (2013) and Singh et al. (2016). Their research shows that the friction factor and the Nusselt number both increase as the number of twisted tapes increases.

Eiamsa-ard and Promvonge (2010) considered configurations in which the tape twist axis coincides with the pipe axis. They explored the effect of tape pitch distance, of alternating clockwise and anti-clockwise contiguous tape segments, and of adding tape pitch angle steps of 30, 60, and 90 degrees between contiguous segments. The 90 degrees step gave the best heat transfer enhancement. Abolarin et al. (2019) independently confirmed that the heat transfer increases by increasing the step angle, for the twist angle steps 0, 30, and 60 degrees. Ali et al. (2021b) applied the continuous tape configuration (0 degrees twist angle step) with a pitch distance $P = L/2$, shown in Figure 4.1(c), to a silicon microchannel. They reported a 37% lower thermal resistance compared to the microchannel without tape, at the cost of 66% more pumping power.

To enhance the performance of pipe heat exchangers, Tusar et al. (2019), Guo et al. (2011) and Khoshvaght-Aliabadi and Feizabadi (2020) used twisted tapes with a gap between the tape and the pipe wall, while Bazdidi-Tehrani et al. (2020) and Eiamsa-ard et al. (2010) also used tapes in contact with the pipe wall. Both configurations are reported to give a higher thermal performance at some pressure drop penalty compared to having no tape. However, no investigation has been found that provides a direct comparison between a twisted tape pipe inset with and without pipe wall clearance, in a microchannel heat sink. This investigation aims to address this knowledge gap first.

Then, this investigation provides additional contributions to the field by detailing the combined effects of pitch distance and twist direction reversal in the 90 degrees pitch step angle configuration Eiamsa-ard and Promvonge (2010) found being the most conducive to heat transfer. Specifically, this research examines the effect of (i) inserting a single twisted tape in a circular microchannel heat sink with and without a gap between the tape and the channel wall, for the pitch distances $P = 0$, $P = L/2$ and $P = L/4$, as shown in Figure 4.1 (e and f) and (ii) inserting head to tail two or four twisted tape segments of individual pitch distance $P = L/4$ with a tape pitch angle step of 90° as shown in Figure 4.1 (g-j).

These forced-convection microchannel heat sink configurations are modelled over the Reynolds number range $100 \leq Re \leq 500$, based on the channel hydraulic diameter and the 298 K coolant water entry temperature. The numerical predictions for the thermal and the hydraulic performance are referenced to the baseline configuration of the forced-convection microchannel heat sink with no tape (MC-NT) from Ali et al. (2021b).

4.2 Geometry and boundary conditions

Figure 4.1 (a) shows the representation of a square-base heat sink with circular microchannels running through it, parallel to one another, in which the cooling water flows, evenly heated from below. In this case, 33 parallel circular tubes run through a silicon wafer of square base, along x_1. For clarity, seven out of the 33 tubes are diagrammatically shown in Figure 4.1 (a). The 33 tubes make up an array of tubes in x_3, out of which only one tube is modelled, to reduce the complexity of the simulation. The temperature field is imposed symmetric between adjacent tubes at the cross-sectional planes shown by the dashed lines in Figure 4.1 (a). Different tape inserts are modelled in the microchannel, as Figure 4.1 (d-j) illustrates. The microchannel with no tape (MC-N) is modified by adding a tape with radial gaps along its long edges (MC-G) or a tape with no gap (MC-NG), as shown in Figure 4.1 (d-f), respectively. Other arrangements in Figure 4.1 (g-j) show tape inserts having a pitch distance of P=L/4 and a $90^{°}$ pitch angle step between consecutive tape segments. These arrangements produce two helices in the same direction (MC-NG-4P-2SD) or four helices in the same clockwise direction (MC-NG-4P-4SD) or two helices in opposing directions (MC-NG-4P-2AD), or four helices in alternating directions (MC-NG-4P-4AD). Table 4.1 lists the main dimensions of the microchannel heat sink and of the tape.

As most modern integrated circuit chips are made by silicon, a microchannel heat sink created in silicon is also considered here. In theory, the heat sink block could be laminated on top of a microprocessor, the lamination process enabling the construction of the channels by stratification. The tape insert could be fabricated by heating and twisting a silicon plain sheet, then seating the tape by CO_2 laser welding (Ali et al., 2021b). Alternatively, a heat sink in copper or other metals could be printed using either metal binder jetting or metal powder bed fusion, which are near-net shape manufacturing methods (Ali et al., 2021b).

57

Table 4.2 lists the thermo-physical properties of the solid and fluid domains. The Reynolds number is between 100 and 500, the inlet temperature T_{in} of the working fluid is fixed at 298 K, and the heat flux input is 100 W/cm^2. The Reynolds number at the inlet of the microchannel heat sink is defined as:

$$\text{Re} = \frac{\rho_f \cdot u_{in} \cdot D_h}{k_f} \tag{4.1}$$

$$D_h = D - \frac{4A}{P} = D - \frac{4\,ab}{2(a+b)} = D - \frac{2\,ab}{a+b} \tag{4.2}$$

In equation (4.2), A is the tape cross-section area, P its perimeter, and a and b are the width and thickness of the tape. If there is no tape, $D_h = D$.

Table 4.1 Dimensions of the circular microchannel heat sink, in mm.

Lx_1	Lx_2	Lx_3	Dh_N	Dh_G	Dh_{NG}	W	Lw	Twisted tape thickness
10	0.4	10	0.2	0.181	0.18	0.3	0.18	0.01

Table 4.2 The thermo-physical properties of silicon (Wang et al., 2011), and water.

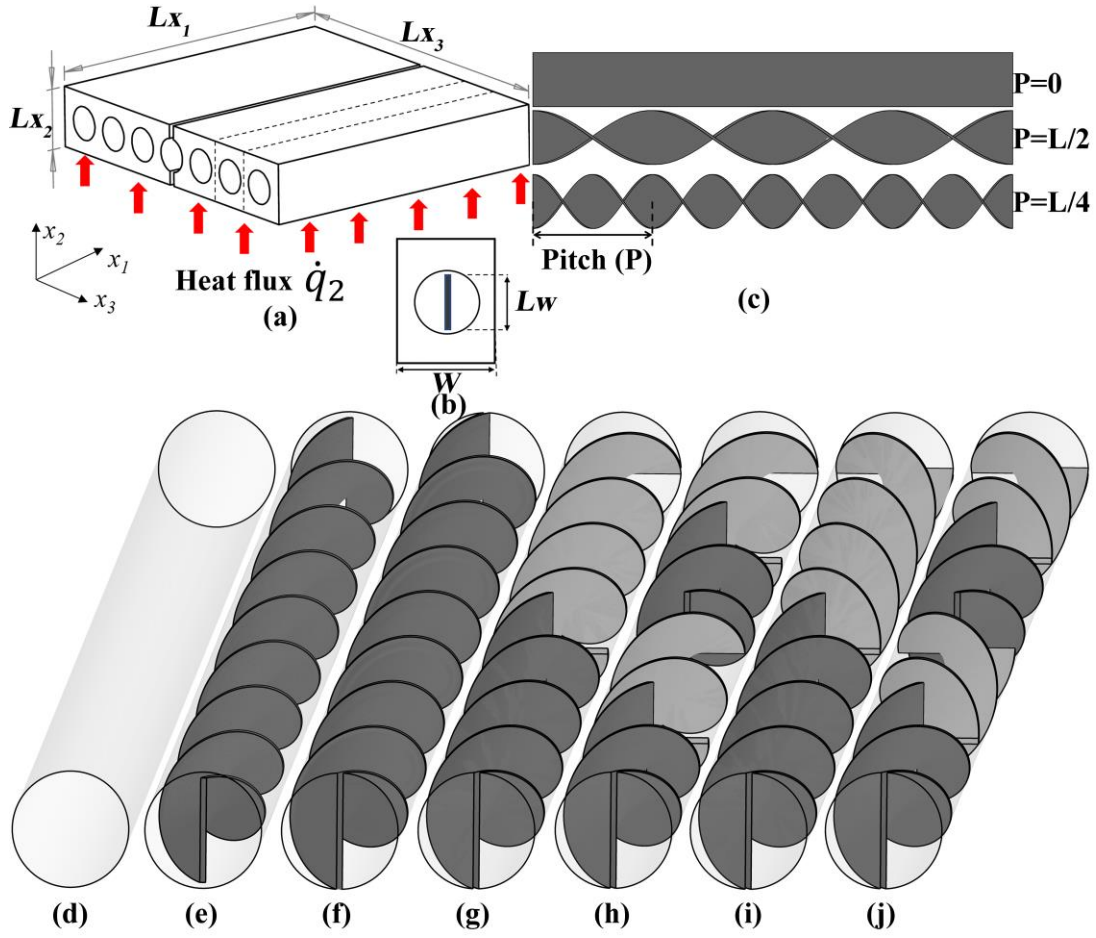| Material	ρ (kg m^{-3})	Cp (J/kg. K)	k (W/m. K)	μ (N $\cdot$ s/m^2)
Silicon	2330	710	148	-
Water	998.2	4182	0.6	0.001003

Figure 4.1(a) Isometric view of the circular microchannel heat sink wafer, (b) Pitch distance (c) Front view of the microchannel, (d) No tape (MC-N), (e) Tape with radial gaps (MC-G-P=L/4), (f) Tape without any radial gap (MC-NG-P=L/4), (g) Two helices in the same direction (MC-NG-4P-2SD), (h) Four helices in the same direction (MC-NG-4P-4SD), (i) Two helices in alternating directions (MC-NG-4P-2AD), (j) Four helices in alternating directions (MC-NG-4P-4AD).

4.3 Grid independence

The sensitivity of the predictions to the spatial discretization of the computational domain is assessed based on the average bottom wall temperature and on the pressure drop across the microchannel. These parameters are selected as these are often key technical specifications in heat sink product sheets. In this study, a coarse mesh is progressively refined until these two parameters display an appreciable mesh independence. A hexahedral mesh is used because it provides greater accuracy and less simulation time than tetrahedral or mixed element meshes (Cengel, 2010a). Accommodating the tape twist in a structured mesh topology required some alteration to the baseline mesh without any tape. Therefore, the mesh convergence assessment was performed both with and without a twisted tape, specifically for the configurations MC-N, MC-G-P=L/4, MC-NG-P=L/4 and MC-NG-4P-4SD of Figure 4.1, with water at Re = 300. Figure 4.2 displays (a) the

predicted average bottom wall temperature and (b) the pressure drop of the working fluid between the inlet and the outlet, against the number of elements. This figure displays no notable change either in the average bottom wall temperature or in the pressure drop as the number of elements is increased beyond 4.6 million. Hence, a mesh size of 4.6 million cells is selected for modelling all the cases. Figure 4.3 shows the mesh topology for two of these cases.
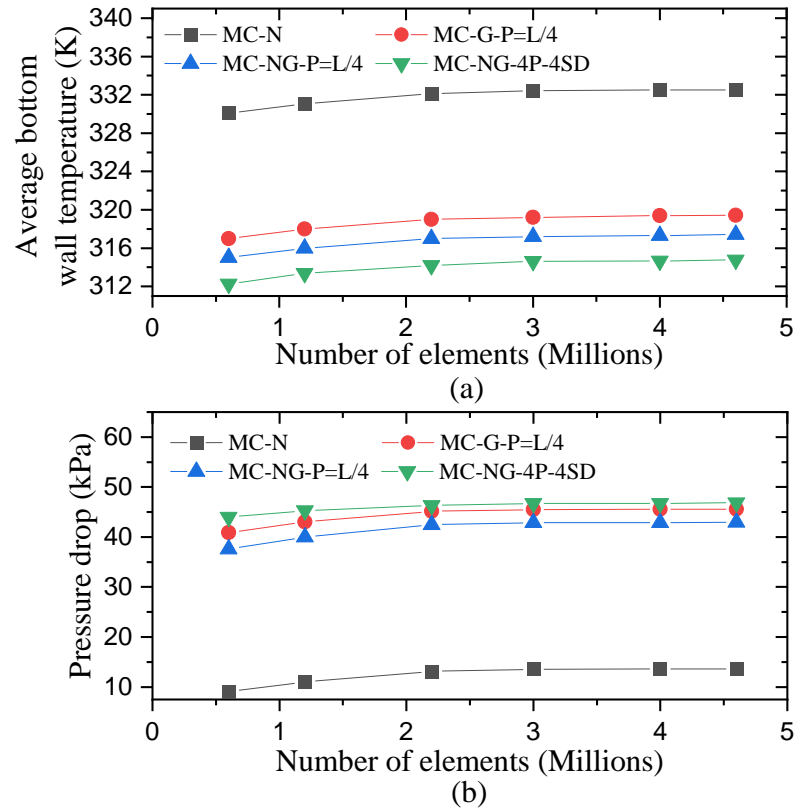

(a)

(b)

Figure 4.2 Grid independence test results. (a) Microchannel average bottom wall temperature and (b) pressure drop across the microchannel.
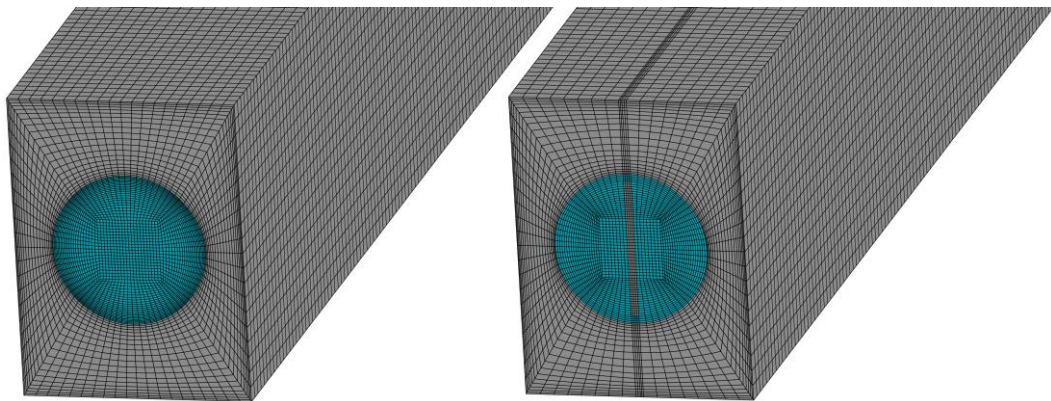

Figure 4.3 Three-dimensional computational mesh structure of MC-N and MC-G-P=0.

60

4.4 Model validation

The conjugate heat transfer model for the microchannel defined in sections 2.1 to 2.3 is validated by comparing its predictions against correlations for the friction loss and for the convective heat transfer in pipes, reported in the literature. The friction factors obtained from the model at different Reynolds numbers are compared against the corresponding Darcy friction factors for a fully developed laminar flow in a straight pipe with a circular cross-section, calculated from the Hagen-Poiseuille equation (Cengel, 2010b). The Darcy friction factor is determined from $f = 64 \, Re^{-1}$ (Cengel, 2010b). This formula only applies to the hydrodynamically fully developed region. Therefore, the friction factor is evaluated from the static pressure change between the end of the entry length $L_h \cong 0.05 Re D_h$ (Cengel, 2010b) of the microchannel and the microchannel outflow, to exclude the hydrodynamic entrance region contributions to f. Figure 4.4 (a) shows that the friction factors from the numerical simulation agree well with the corresponding values from the Darcy law, as the two curves overlap. The substantial overlap between these two friction factor predictions in Figure 4.4 (a) provides confidence that the model can satisfactorily predict the microchannel hydraulic head loss over the Reynolds number range 100 to 500. Figure 4.4 (b) compares the predictions of the local Nusselt number for MC-N from the conjugate heat transfer model to corresponding ones determined by the Shah correlation (Narendran et al., 2020) of equation (4.3). Figure 4.4 (b) displays, overall, a fairly good agreement between the two sets of predictions, with a maximum discrepancy of 5.7%. More importantly, both methods differentiate well the non-dimensional heat transfer due to convection at different local Reynolds numbers, as expressed by the channel length on the abscissa, and exhibit the same monotonic trend. This enables the use of the microchannel conjugate heat transfer model with some confidence for the current comparative study of heat transfer in laminar pipe flow at different Reynolds numbers.

$$Nu = \begin{cases} 1.953 (RePr \dfrac{D_h}{x})^{1/3} & (RePr \dfrac{D_h}{x}) \geq 33.3 \\ 4.364 + 0.0722 (RePr \dfrac{D_h}{x}) & (RePr \dfrac{D_h}{x}) < 33.3 \end{cases} \qquad (4.3)$$

(a)

(b)
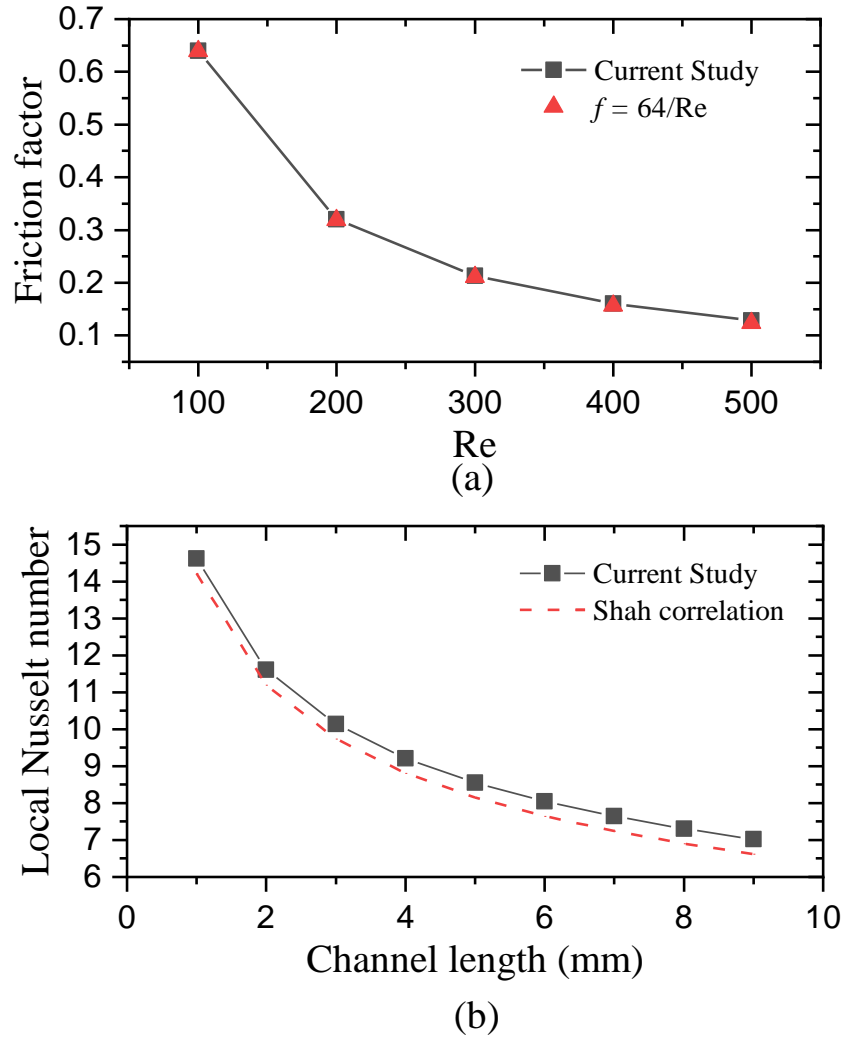
Figure 4.4 Comparison of flow and heat transport predictions from the microchannel model to published correlations. (a) Friction factor and (b) local Nusselt number of MC-NT.

4.5 Results and Discussion

In this section the thermal performance of the circular microchannel heat sink with several modified twisted tape designs is described.

4.5.1 Effects of twisted tape pitch on temperature distribution and flow pattern

Figure 4.5 illustrates the temperature distributions on the bottom surface as well as on the inner wall of cases MC-N, MC-NG-P=0, MC-NG-P=L/2 and MC-NG-P=L/4 at the Reynolds number of 500. The surface temperature distribution is presented in colour iso-levels, with red indicating 335 K and blue 298 K. Figure 4.5 shows that by introducing the straight tape (MC-NG-P=0), the bottom and the inner wall surface temperatures are reduced to below 308 K (in light blue) at the microchannel inlet and to approximately 327 K (in yellow) at the microchannel exit. Temperatures are further reduced to 304 K and

302 K at the inlet and to 319 K and 317 K at the exit, by twisting the tape with pitch distance L/2 (MC-NG-P=L/2) and L/4 (MC-NG-P=L/4), respectively.
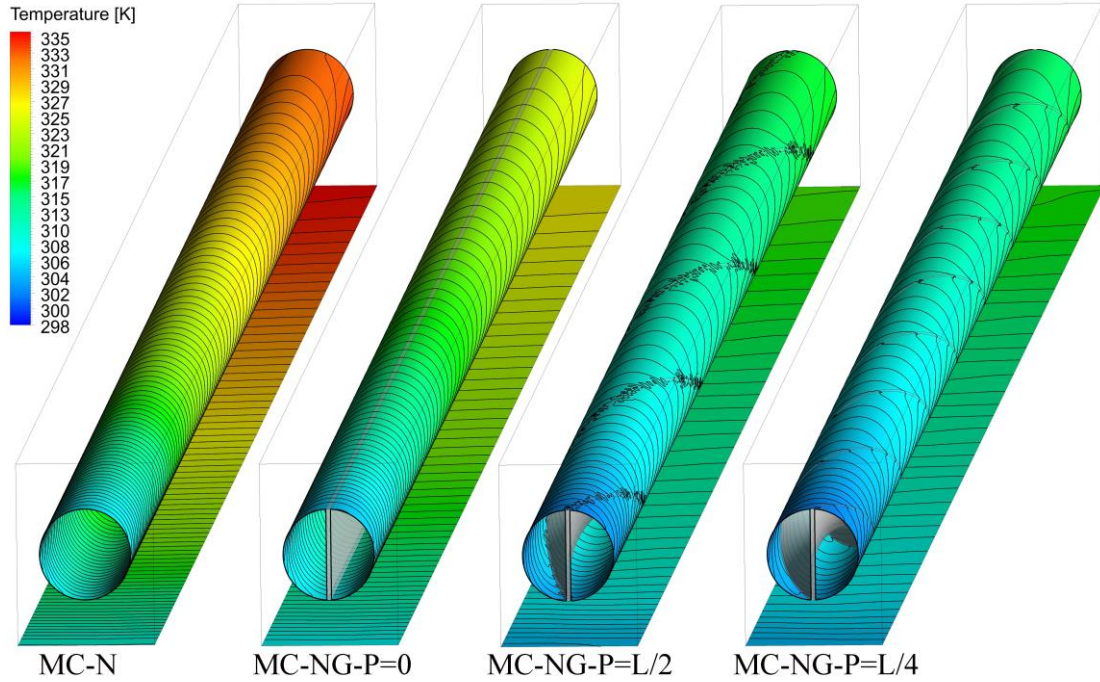
Figure 4.5 Temperature colour iso-levels on the bottom surface as well as on the inner wall of MC-N, MC-NG-P=0, MC-NG-P=L/2, and MC-NG-P=L/4 at Re = 500.

Figure 4.6 displays the temperature distribution in the cross-sectional plane through the middle of the microchannel heat sink with no tape and with a tape of pitch distance P=0, P=L/2, and P=L/4, at Re = 500. The maximum bottom wall temperature is obtained with the microchannel with no tape, whereas the minimum bottom wall temperature is obtained in the case with the pitch distance P=L/4. The tape acts as a heat bridge across the pipe, improving the heat transfer performance by increasing the internal wet surface area. A minor contribution is also thought to be produced by the axial conduction along the tape from the outlet to the inlet due to the axial increase in temperature towards the outlet. Twisting the tape further reduces the thermal resistance between the solid and the fluid regions by generating a secondary swirl flow that increases the velocity of the fluid near the channel wall, as Figure 4.7 and Figure 4.8 illustrate.
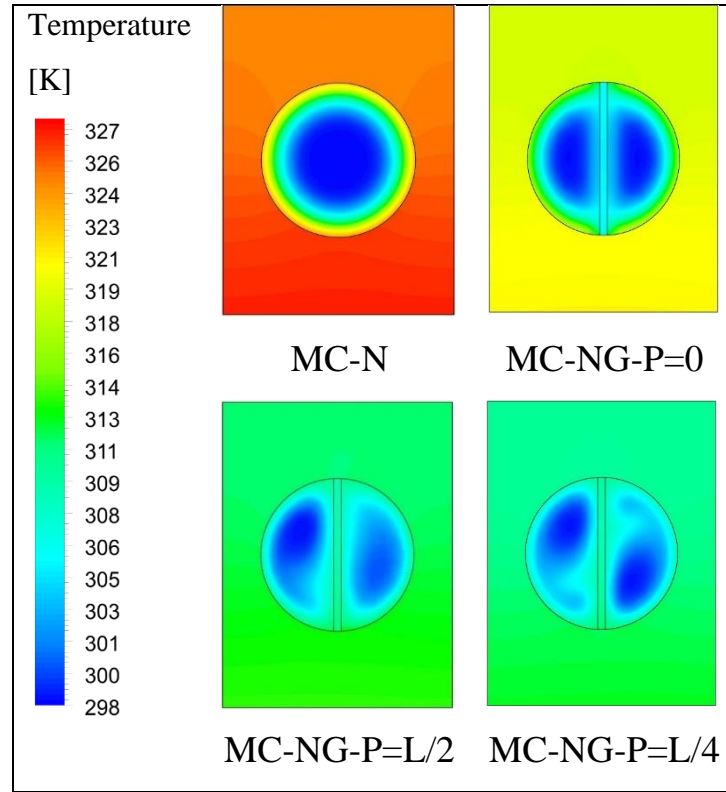
Figure 4.6 Temperature distribution in the cross-sectional plane through the middle of the microchannel heat sink with no tape and with a tape of different pitch distances, at Re = 500.

To clarify the effect of the tape on the flow pattern in the microchannel heat sink, streamline distributions are presented in Figure 4.7. The cases shown are MC-N, MC-NG-P=0, MC-NG-P=L/2, and MC-NG-P=L/4 at Re = 500. The streamlines are coloured by flow velocity magnitude, with red corresponding to 5 m/s and blue to 0 m/s. Inserting the straight tape (P=∞) raises the flow blockage because of the growing boundary layers on the tape surfaces, resulting in a slightly higher axial velocity away from the walls compared to the case with no tape. This effect, together with the increase of the internal wet surface area, contributes to the enhancement of the cooling performance at the expense of an increased flow resistance, and therefore of an increased pumping power. The twisted tape is shown in Figure 4.7 to generate a swirl flow that increases the cooling performance but also the flow resistance, compared to the cases with no tape (MC-NT) and with a straight tape (MC-NG-P=0). A higher flow resistance is also obtained by decreasing the pitch distance from L/2 to L/4. Varying the Reynolds number in the range $100 \leq Re \leq 500$ results in a corresponding change in velocity and in similar swirl streamline patterns that are not shown here, for brevity. The Re = 500 condition provides the highest cooling performance due to its higher bulk velocity.
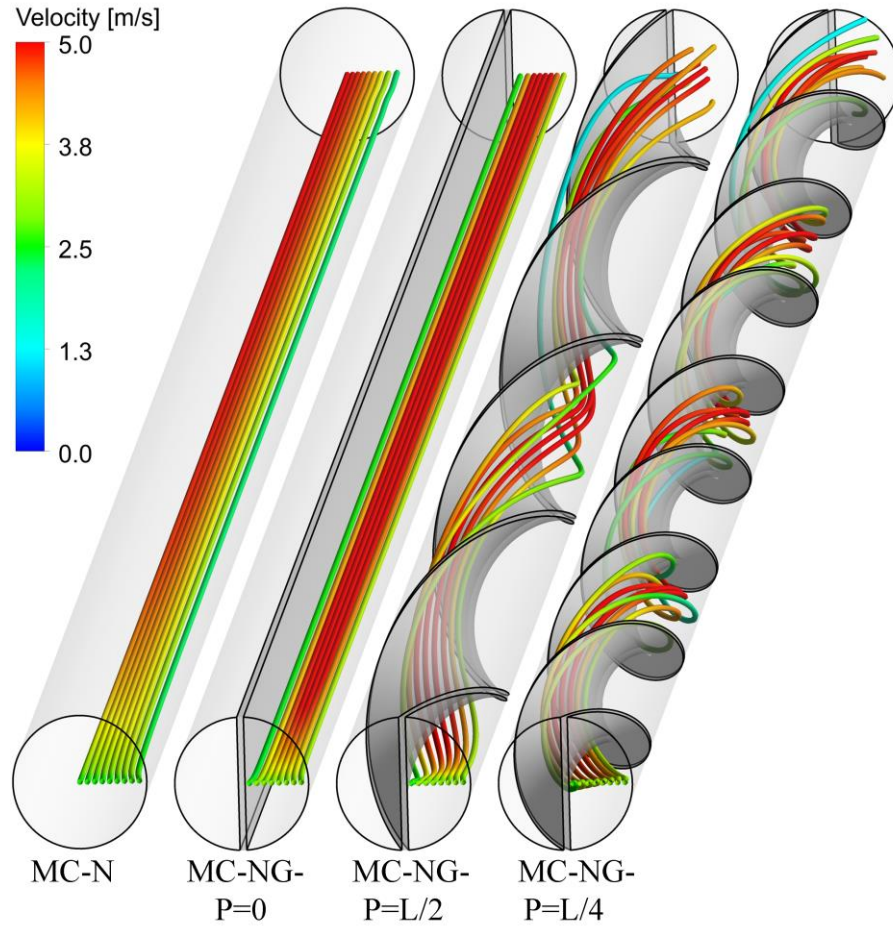
Figure 4.7 Streamlines in the microchannel heat sinks MC-N, MC-NG-P=0, MC-NG-P=L/2, and MC-NG-P=L/4, at Re = 500. The streamlines are colour-coded by the velocity magnitude.

Figure 4.8 displays the velocity magnitude distributions on the cross-sectional plane in the middle of the microchannel heat sink, with no tape and with a continuous tape of pitch distance P=0, P=L/2, and P=L/4, at Re = 500. The velocity magnitude is shown by colour iso-levels, with red corresponding to 5 m/s and blue to 0 m/s, while the black vectors represent the in-plane velocity component. As it can be seen from these colour iso-levels, the velocity magnitude of the microchannel without any tape (MC-N) is highest at the centre and decreases towards the wall, as in a classical Hagen-Poiseuille type flow through a pipe. In the case with the inserted straight tape (MC-NG-P=0), the flow is divided into two equal parts, each part acting as a Hagen-Poiseuille type flow. Thus, case MC-NG-P=0 shows an increased peak velocity compared to case MC-N. Inserting a twisted tape with a pitch distance of L/2 increases the flow blockage and generates significant in-plane motion, or secondary flow, as shown in Figure 4.8 by the black vectors. A stronger secondary flow is obtained by decreasing the pitch distance from L/2 to L/4. This swirl flow increases the heat convection in the transverse direction as it helps

transport heated fluid away from the cooler microchannel top, which has adiabatic walls, towards the hotter microchannel bottom, which has the heated wall. Varying the Reynolds number in the range 100 to 500 results in a corresponding change in velocity distribution and in-plane velocity vectors magnitude that is not shown here, for brevity. The flow pattern is consistent over this Reynolds number range. At Re = 500, the strongest swirl flow and therefore the highest cooling performance is predicted.
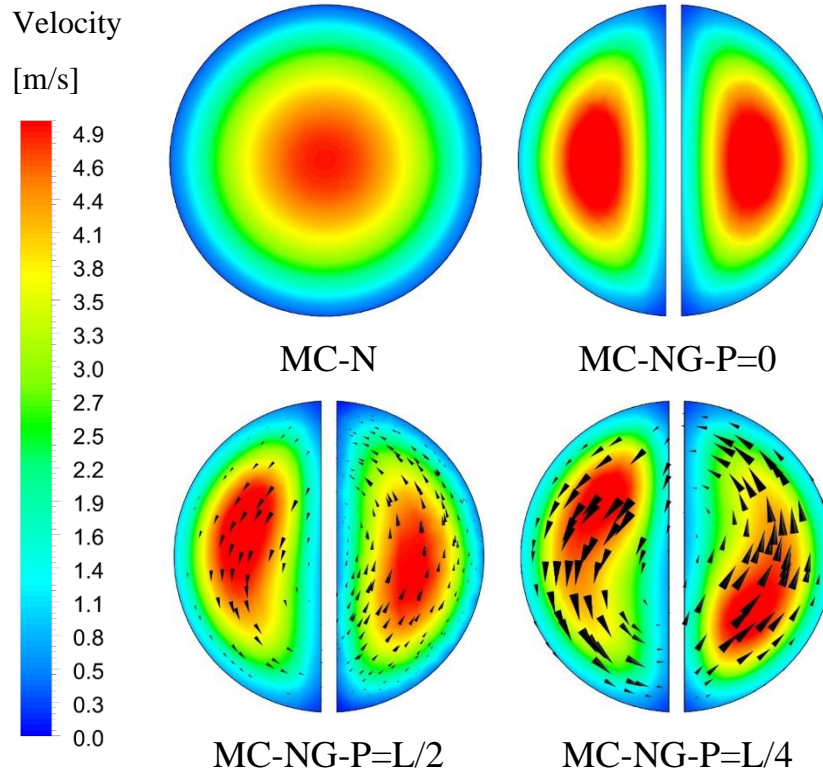
Figure 4.8 Colour iso-levels of velocity magnitude in the $x_1 = 5$ mm plane and in-plane velocity vectors at Re = 500. MC-N, MC-NG-P=0, MC-NG-P=L/2, and MC-NG-P=L/4, viewed from the inlet.

4.5.2 Effects of twisted tape radial gap and segmentation on temperature distribution and flow

Figure 4.9 shows the temperature distributions on the bottom surface as well as on the inner wall for cases MC-G-P=L/4, MC-NG-P=L/4, MC-NG-4P-4SD and MC-NG-4P-4AD, at Re = 500. The surface temperature distribution is presented by colour iso-levels, with red corresponding to 318 K and blue to 298 K. The temperature distribution in the microchannel without any radial gap (MC-NG-P=L/4) is lower than in the microchannel with radial gaps (MC-G-P=L/4), indicating a lower thermal resistance, as illustrated in the discussion of Figure 4.10. A further decrease in the average bottom wall temperature is achieved by splitting the twisted tape into four helices in the same direction

(MC-NG-4P-4SD), with an even further reduction obtained with four helices in alternating directions (MC-NG-4P-4AD). The reason for this temperature reduction will be discussed in the context of Figure 4.12 and Figure 4.13. The effect of the number of helices, not visualized here for brevity, indicates that twisted tapes with four helices (4SD and 4AD) provide a better cooling performance compared to the ones with two helices (2SD and 2AD), respectively. The effect of the Reynolds number from 100 to 500 was also examined, showing that the surface temperature decreases by increasing the Reynolds number and that the lowest surface temperature is achieved at Re = 500.
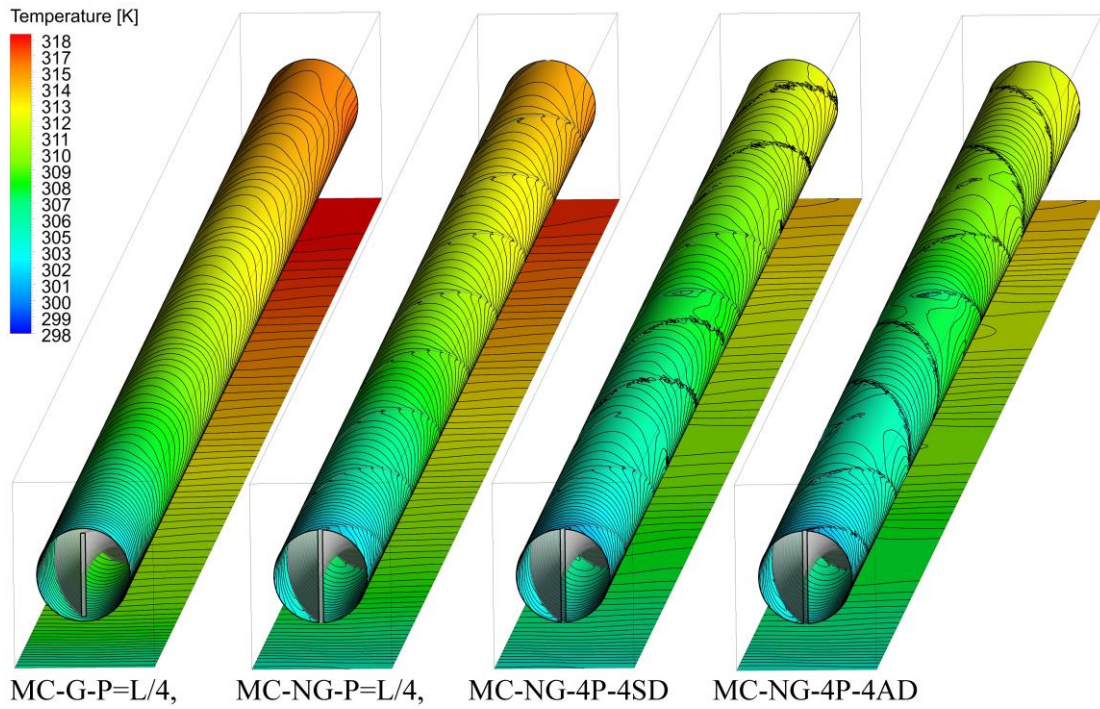
Figure 4.9 Temperature colour iso-levels on the bottom surface and on the inner wall of MC-G-P=L/4, MC-NG-P=L/4, MC-NG-4P-4SD, and MC-NG-4P-4AD, at Re = 500.

Figure 4.10 shows the temperature distribution on the cross-sectional plane in the middle of the microchannel heat sink with different twisted tape designs, at Re = 500. The negative effect of the radial gaps along the tape top and bottom edges is clearly shown by the MC-G tape being colder. These gaps prevent the conduction of heat between the tape and the channel wall, which enhances the cooling performance of the microchannel in the case with no radial gap, as previously argued in the context of Figure 4.6. As a result, the average temperature in the case MC-NG-P=L/4 is lower than in the case MC-G-P=L/4. Cases MC-NG-4P-4SD and MC-NG-4P-4AD show decreased temperatures and a more homogeneous temperature distribution. The four helices in alternating directions (MC-

NG-4P-4AD) produce the lowest thermal resistance among all the modelled configurations.
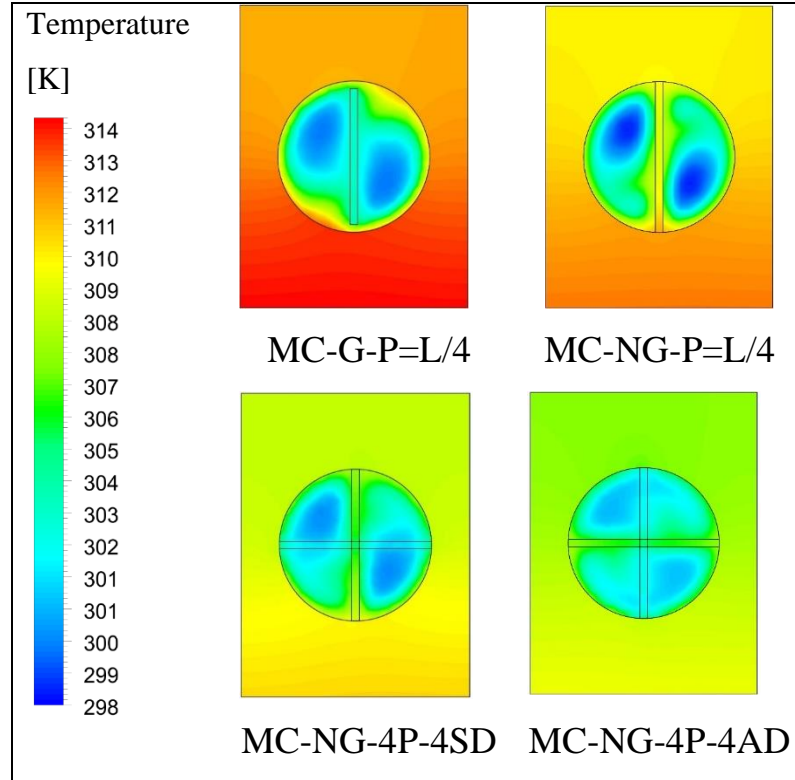
Figure 4.10 Temperature distribution in the cross-sectional plane $x_1 = L/2$ with different twisted tape designs at Re = 500 and at a constant twist pitch distance P = L/4.

An analysis of the flow pattern is performed to explain these effects. Figure 4.11 displays a radial rake of streamlines in the microchannel heat sink with the twisted tape designs MC-G-P=L/4, MC-NG-P=L/4, MC-NG-4P-4SD, and MC-NG-4P-4AD, at Re = 500. The streamlines are coloured by the flow velocity magnitude, with red corresponding to 5 m/s and blue to 0 m/s. The microchannel with radial gaps and the microchannel without gap MC-NG-P=L/4 appear to have the same twisting streamline pattern. The segmentation of the tape into four clockwise helices in MC-NG-4P-4SD produces a stronger mixing but also a higher flow blockage. The four helices in alternating directions in MC-NG-4P-4AD produce a further increase in the flow blockage, due to the change in the direction of the swirl shown by the streamlines, but lead to a more even mixing, as clarified in Figure 4.12 and Figure 4.13.
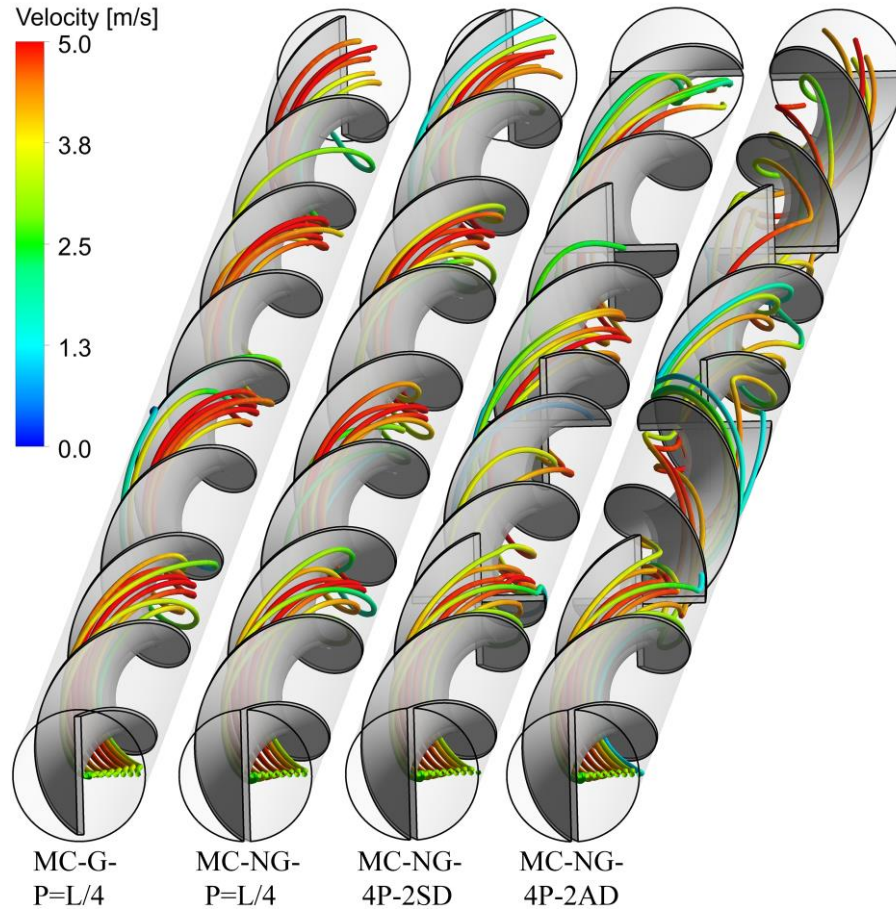
Figure 4.11 Streamlines through the microchannel heat sinks MC-G-P=L/4, MC-NG-P=L/4, MC-NG-4P-4SD, and MC-NG-4P-4AD, at Re = 500. The streamlines are colour coded by the velocity magnitude.

Figure 4.12 shows the velocity magnitude distributions on the cross-sectional plane at $x_1 = 7$ mm from the inlet with the twisted tape designs MC-G-P=L/4, MC-NG-P=L/4, MC-NG-4P-4SD, and MC-NG-4P-4AD, at Re = 500. The microchannel with radial gaps along the tape perimeter MC-G-P=L/4 is predicted to feature a slightly higher peak velocity magnitude than the microchannel without any gap MC-NG-P=L/4. This appears to be due to the additional flow resistance encountered by the flow in the vicinity of the gaps, where secondary flow features narrow the effective cross-section area. An even higher peak velocity magnitude and in-plane motion are obtained by segmenting the tape, by which the flow blockage is increased. Although Figure 4.12 shows a somewhat higher peak velocity magnitude from the microchannel with the four helices in alternating directions MC-NG-4P-4AD compared to the microchannel with four helices in the same direction MC-NG-4P-4SD, additional flow changes are likely to underpin the heat performance difference between these two configurations.
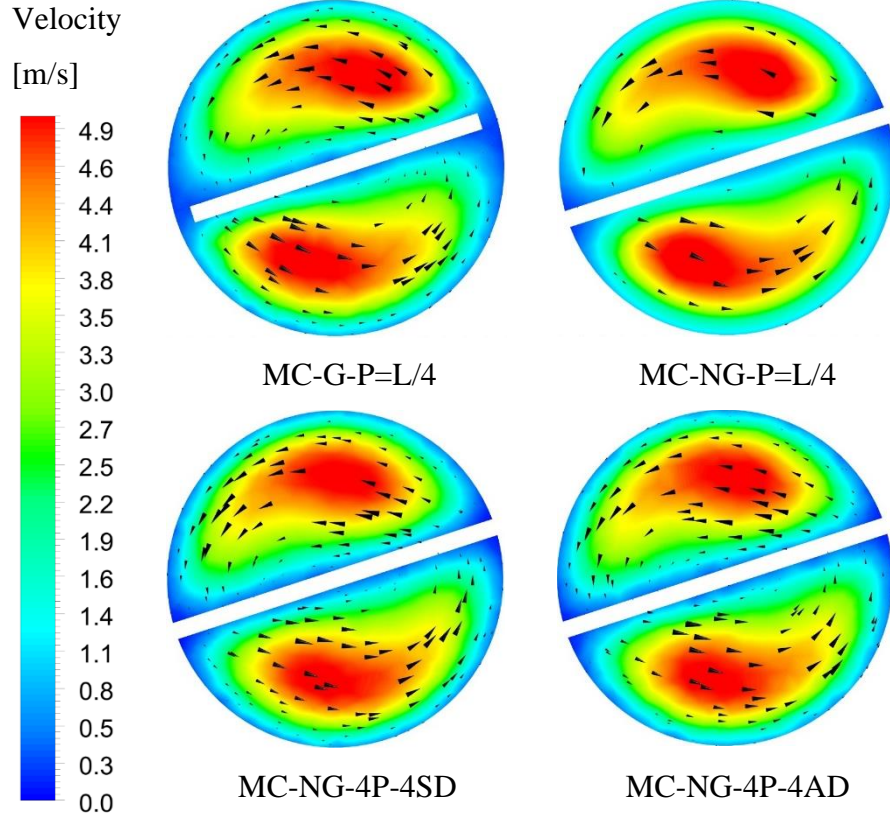
Figure 4.12 Colour iso-levels of velocity magnitude and in-plane velocity vectors 7 mm from the inlet of the microchannel heat sink, for different twisted tape designs, at Re = 500.

To further investigate this difference, Figure 4.13 shows selected streamlines for cases MC-NG-4P-4SD and MC-NG-4P-4AD at Re = 500. The streamlines are generated from an annular source at the inlet with a diameter around 0.16 mm at a distance from the inlet of 2.45 mm. As it can be seen from these streamlines, using four helical tape segments with alternating directions in MC-NG-4P-4AD tends to radially push the streamlines from the axis of the microchannel towards the near-wall region more than by using only clockwise twisted tape segments in MC-NG-4P-4SD. This behaviour reduces the thermal resistance by offering further convection heat transfer along the microchannel inner cylindrical wall and produces a more homogeneous temperature distribution in comparison to the case MC-NG-4P-4SD, as shown in Figure 4.10.
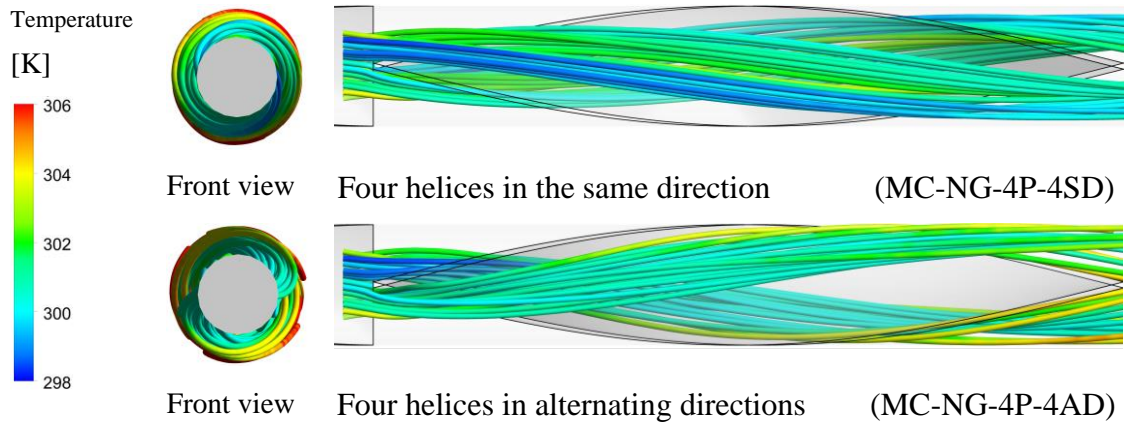
Figure 4.13 Streamlines through microchannels with only clockwise twisted tape inserts MC-NG-4P-4SD and with alternating clockwise and anti-clockwise twisted tape inserts MC-NG-4P-4AD, at Re = 500. The streamlines are colour-coded by the temperature.

4.5.3 Effects of twisted tape design on thermal characteristics

The convective heat transfer relative advantage of microchannel heat sinks with tape over the no tape configuration of Figure 4.1(d) is shown in Figure 4.14, where the average Nusselt number ratio (Nu/Nu_0) from the configurations of Figure 4.1 (e-j) are reported over the Reynolds number range 100 to 500. Subscript ($_0$) refers to the microchannel without any tape. For reference, Table 4.3 lists the Nusselt number, the pressure drop, and the friction factor predicted from the microchannel heat sink model without any tape. It is noted that the average Nusselt number ratio monotonically increases with increasing Reynolds number, so that the tape inserts are predicted to facilitate heat convection more at the higher Reynolds numbers. Figure 4.14 shows that the average Nusselt number ratio of the microchannel without any radial gap, of Figure 4.1 (f), is higher than that from the microchannel with radial gaps, of Figure 4.1 (e), at any given Reynolds number. This advantage is attributed to the heat conduction between the tape and the heat sink cylindrical inner wall, as these surfaces touch one another in Figure 4.1 (f). The absence of any tape radial gap also marginally increases the tape heat transfer surface area. Figure 4.14 shows that inserting a straight tape already provides about a 20% higher average Nusselt number, depending on the Reynolds number, compared to not having any tape. Twisting the tape increases this advantage. Reducing the twisted tape pitch distance from L/2 to L/4, i.e. using a tape helix finer pitch, provides a further gain in the predicted average Nusselt number ratio. With this finer pitch, coolant flow parcels, guided by the tape, follow a longer path from the microchannel inlet to the microchannel exit, so they get an extended exposure to the heated microchannel walls. This provides more distance over which to extract heat from the microchannel inner surface.

71

Figure 4.14 shows that the technique by Eiamsa-ard and Promvonge (2010) and by Abolarin et al. (2019) of inserting a 90 degrees tape pitch angle step, by segmenting the tape, works well in the silicon microchannel heat sink configuration of Figure 4.1. Using the tape made up of two silicon segments twisted in the same direction (MC-NG-4P-2SD) of Figure 4.1 (g) confers a higher average Nusselt number ratio than having a single tape helix throughout the microchannel length. Increasing the tape segmentation from two to four (MC-NG-4P-4SD), as in Figure 4.1 (h), increases this gain. The flow study presented in section 4.5.2 advances the state of the art by providing evidence to explain the performance gain from the pitch angle steps in a microchannel heat sink. This gain is probably due to the generation of a fresh, thin thermal boundary layer at the leading edge of each new tape segment. The trailing edge of the preceding tape segment sheds a shear layer that promotes coolant flow mixing. Furthermore, the new helix appears to circulate the coolant towards the microchannel bottom, which is closer to the heat source, over a shorter axial distance compared to an uninterrupted tape helix. These three effects combine to provide the observed heat transfer performance advantage.

Figure 4.14 corroborates another interesting aspect from the work of Eiamsa-ard and Promvonge (2010), which is the generation of a convective heat transfer advantage by alternating the direction of twist in consecutive tape segments. With microchannels as in Figure 4.1 (i) and (j), the average Nusselt number ratio labelled MC-NG-4P-2AD and MC-NG-4P-4AD is higher than the corresponding values labelled MC-NG-4P-2SD and MC-NG-4P-4SD, which use only clockwise twist. The flow study in section 4.5.2 provides new, state of the art, important insight into the mechanism behind this gain, such knowledge being fundamental to exploiting this phenomenon in industrial products. By alternating the direction of the twist, the incoming flow produces a phenomenon akin to a leading-edge stall on the tape segment that follows. The stall reportedly diverts the coolant away from the tape surface, moving away from the centre of the microchannel towards the heated cylindrical walls. In this process, less hot coolant running through the channel centre replaces the warmer coolant running closer to the cylindrical walls. This provides a more uniform coolant through-flow temperature, as shown in Figure 4.10. The average Nusselt number ratio gain is highest at Reynolds number 500, with a gain of 168.1%, 155.33%, 106.31% and 76.13% with respect to the MC-N configuration for cases MC-NG-4P-4AS, MC-NG-4P-4SD, MC-NG-P=L/4 and MC-G-P=L/4, respectively.

72
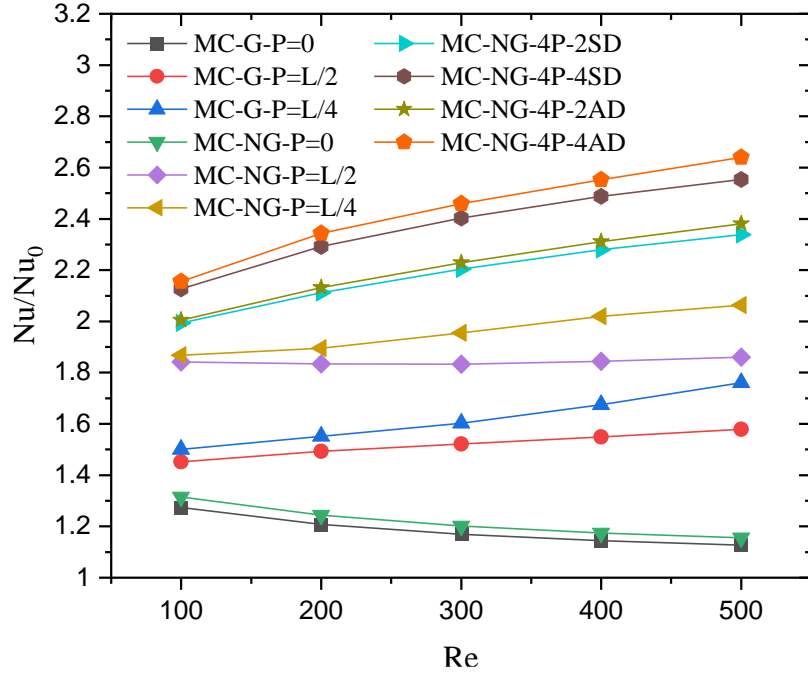
Figure 4.14 Average Nusselt number ratio for all the microchannel configurations of Figure 4.1, over the Reynolds number range 100 to 500.

Table 4.3 Average Nusselt number, pressure drop and friction factor of the microchannel heat sink without any tape MC-NT.

Re	100	200	300	400	500
Nu_0	11.17	13.07	14.45	15.59	16.57
ΔP_0 (kPa)	4.21	8.75	13.6	18.76	24.23
f_0	0.67	0.35	0.24	0.18	0.15

Figure 4.15 shows how the tape inserts of Figure 4.1 (e-j) affect the difference between the average temperature (T_{max}) of the heated bottom wall and the temperature (T_{in}) of the coolant at the microchannel inlet, over the Reynolds number range 100 to 500. $T_{max} - T_{in}$ decreases monotonically with increasing Reynolds number in all the configurations of Figure 4.1 (d-j) irrespective of the presence of any tape. The largest temperature difference T_{max} -T_{in} at all Reynolds numbers is obtained in the absence of any tape (MC-N), as in Figure 4.1 (d). This difference is up to 57 K at the lowest Reynolds number of 100 and it represents a significant unwanted temperature overheat in the thermal conditioning of microprocessors and of microelectronic devices. Inserting a straight tape as in Figure 4.1 (e) lowers this temperature difference (MC-G-P=0). Twisting the tape (MC-G-P=L/2) and reducing the tape pitch (MC-G-P=L/4) progressively reduces T_{max}-T_{in}.

Closing the radial gaps between the tape and the heated cylindrical wall, as in Figure 4.1 (f), provides a lower temperature difference in MC-NG-P=0 than in the corresponding configuration with radial gaps of Figure 4.1 (e), MC-G-P=0. Closing the radial gaps is likewise advantageous with twisted tapes of L/2 pitch, MC-G-P=L/2 vs MC-NG-P=L/2, and of finer pitch L/4, MC-G-P=L/4 vs MC-NG-P=L/4. This trend is displayed across the full Reynolds number range 100 to 500.

T_{max}–T_{in} in MC-NG-P=L/4 is further reduced by inserting 90 degrees tape pitch angle steps, and two steps (MC-NG-4P-2SD) give a lower temperature difference than one step (MC-NG-4P-4SD). Alternating the direction of the tape twist (MC-NG-4P-2AD and MC-NG-4P-4AD) provide a small incremental decrease in the temperature difference compared to using just clockwise twisted tape segments (MC-NG-4P-2SD and MC-NG-4P-4SD). The T_{max} of MC-NG-4P-4AD, MC-NG-4P-4SD, MC-NG-P=L/4 and MC-G-P=L/4 are 16.13℃, 15.91℃, 13.7℃ and 12.42℃ lower than the T_{max} with the MC-N configuration at the Reynolds number of 500.
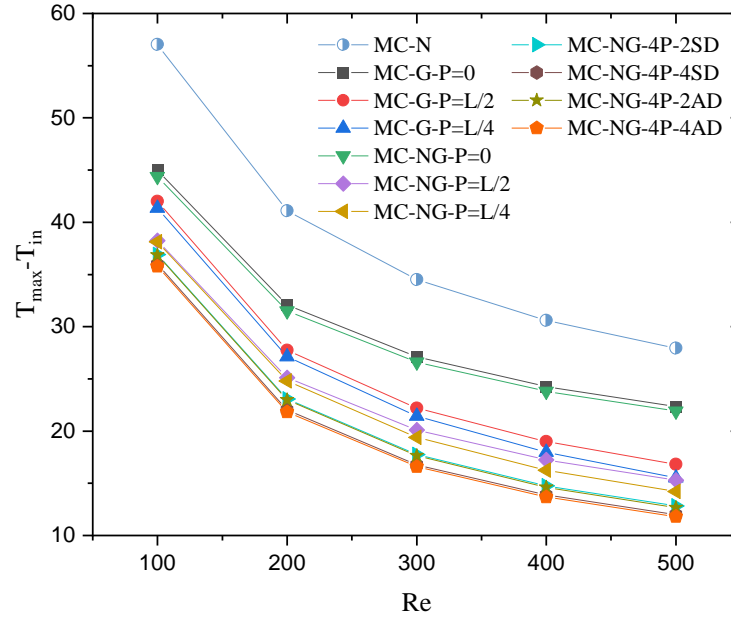
Figure 4.15 Difference between the average bottom wall temperature (T_{max}) and the inlet flow temperature (T_{in}) in microchannels with different tape inserts, over the Reynolds number range 100 to 500.

4.5.4 Effects of twisted tape design on hydraulic characteristics

Inserting a tape in a microchannel causes unwanted additional resistance to flow and Figure 4.16 quantifies this effect in terms of the ratio between the pressure drop predicted with a tape to the one without a tape, $\Delta p/\Delta p_0$, over the Reynolds number range 100 to 500. All microchannel configurations with a tape insert are shown to have about

three times the pressure drop of the microchannel without any tape MC-N. The pressure drop of the microchannel without any tape increases monotonically with the Reynolds number, a shown in Table 4.3. Whereas $\Delta p / \Delta p_0$ for configurations MC-G-P=0, MC-NG-P=0, MC-G-P=L/2, MC-NG-P=L/2, and partially MC-NG-P=L/4 have downwards trends with increasing Reynolds number, the raise of Δp_0 with Re in Table 4.3 produces a net rise in Δp with increasing Reynolds numbers, for all the modelled microchannel configurations. The pressure drop across all the microchannels with radial gaps is higher than that of the corresponding microchannel configuration without any radial gap, due to flow leakage through the gap creating secondary flows and a locally high shear stress past the gap. This pressure drop mechanism is akin to the blade tip leakage effect in unshrouded turbine blades, which experience larger passage losses than equivalent shrouded blades. Twisting the tape (MC-NG-P=L/2) increases the pressure loss compared to using a straight tape (MC-NG-P=0), more so if the pitch of the tape twist is finer (MC-NG-P=L/4).

Modifying the twisted tape MC-NG-P=L/4 by inserting 90° tape pitch angle steps generates additional pressure drop in MC-NG-4P-2SD, which increases with the number of pitch angle steps in MC-NG-4P-4SD, and by alternating the direction of the tape helix (MC-NG-4P-2AD and MC-NG-4P-4AD) in consecutive tape segments. At the Reynolds number of 500, the pressure drop (Δp) of MC-NG-4P-4AS, MC-NG-4P-4SD, MC-NG-P=L/4 and MC-G-P=L/4 are 269.5%, 256.6%, 220.99% and 253.57% higher than that from the MC-N configuration, which is the microchannel without any tape.
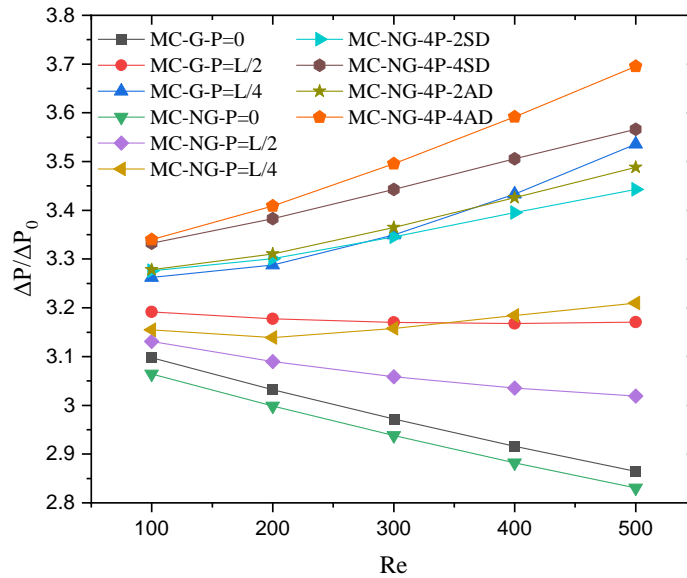
Figure 4.16 Pressure drop across microchannels with various tape inserts normalised by the pressure drop across the microchannel without any tape MC-NT. Numerical predictions over the Reynolds number range 100 to 500.

The same increased flow resistance effect in microchannels with a tape in Figure 4.16 can be expressed in terms of changes in the friction factor ratio f/f_0, as shown in Figure 4.17. f/f_0 is the ratio of the friction factor predicted in a microchannel with a tape to the one predicted in the configuration MC-N of Figure 4.1 (d), without any tape. Figure 4.16 and Figure 4.17 are identical but for a scaling factor on the ordinate. The friction factor, which is calculated using the Darcy equation, Eq. (2.26), is a function of the pressure drop, the hydraulic diameter, and the length of the microchannel. Since the microchannel length L is constant for all the microchannel configurations of Figure 4.1 (d-j), then $f/f_0 = (\Delta p/\Delta p_0)(D_h/D_{h_0})^3$, at any given Reynolds number. The reduction in hydraulic diameter from inserting the tape reported in Table 4.1 generates the ordinate scaling factor between Figure 4.16 and Figure 4.17. MC-N has the lowest friction factor, due to its lowest wetted wall surface area and its mainly axial through flow. The same observation was reported by Bazdidi-Tehrani et al. (2020) in a tube. The friction factors (f) of MC-NG-4P-4AS, MC-NG-4P-4SD, MC-NG-P=L/4 and MC-G-P=L/4 are 173.66%, 164.11%, 137.73% and 162.30% higher than f_0 of the MC-N configuration at the Reynolds number of 500.
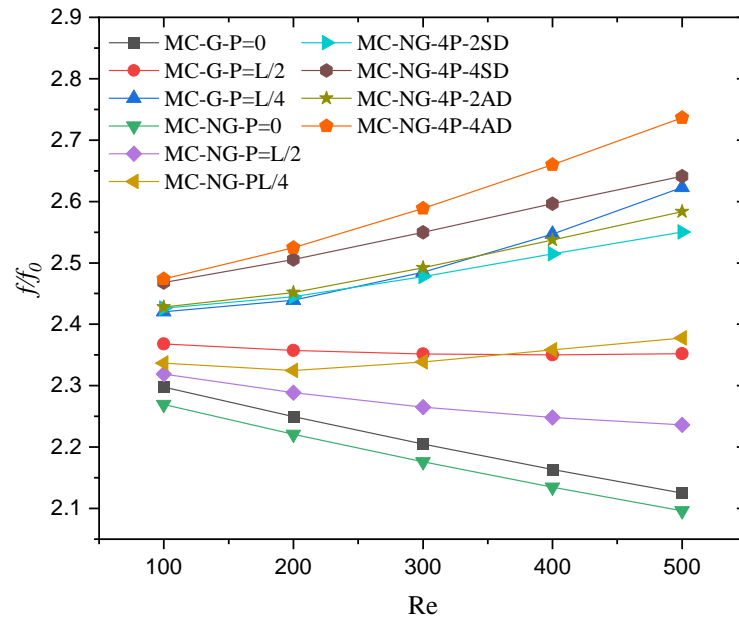

Figure 4.17 Friction factor through microchannels with various tape inserts normalised by the friction factor from the microchannel without any tape MC-N. Numerical predictions over the Reynolds number range 100 to 500.

4.5.5 Overall thermal performance

The Figure of Merit (FoM) in Figure 4.18 shows the trade-off between the gains in thermal performance, expressed by Nu/Nu_0, and the hydraulic losses incurred, expressed by f/f_0, as a tape insert is added to a cylindrical microchannel. The performance of the cylindrical microchannel with no tape (MC-N) is used as a reference at each Reynolds number. Figure 4.18 shows that the FoM from all the microchannel configurations with a twisted tape is above 1.0 and hence it is higher than that of MC-N. Using a straight tape provides an unwanted, adverse trade-off of less than 1.0 at all Reynolds numbers, which is mainly due to a relatively modest thermal performance gain against a more significant hydraulic loss penalty, for the configurations MC-G-P=0 and MC-NG-P=0. The trade-off is more adverse at the higher Reynolds numbers. Radial gaps between the tape edges and the cylindrical inner wall, in MC-G-P=0, MC-G-P=L/2, and MC-G-P=L/4 lower the FoM compared to the corresponding configurations MC-NG-P=0, MC-NG-P=L/2, and MC-NG-P=L/4 without any radial gap. This is due to a combination of lack of thermal conduction between the tape and the cylindrical walls and of hydraulic loss caused by the tape gap through-flow, as shown in Figure 4.14 and Figure 4.17, respectively. The FoM bars in Figure 4.18 show that introducing one 90 degrees tape pitch angle step in MC-NG-P=L/4 provides an appreciable gain in the FoM (MC-NG-4P-2SD). Adding a second 90 degrees pitch angle step (MC-NG-4P-4SD) gives a further benefit in the FoM. Conversely, alternating the azimuthal direction of the tape twist in consecutive tape segments, like in MC-NG-4P-2AD and in MC-NG-4AD, provides a comparatively lower gain in the FoM over inserting tape segments of only clockwise twist, as in MC-NG-4P-2SD and MC-NG-4P-4SD. Alternating the tape twist may therefore not provide an attractive uplift to the FoM over other configuration variants. The microchannel with fine pitch twist tape segments of alternating direction (MC-NG-4P-4AD) provides the highest FoM among all the configurations tested in this study.
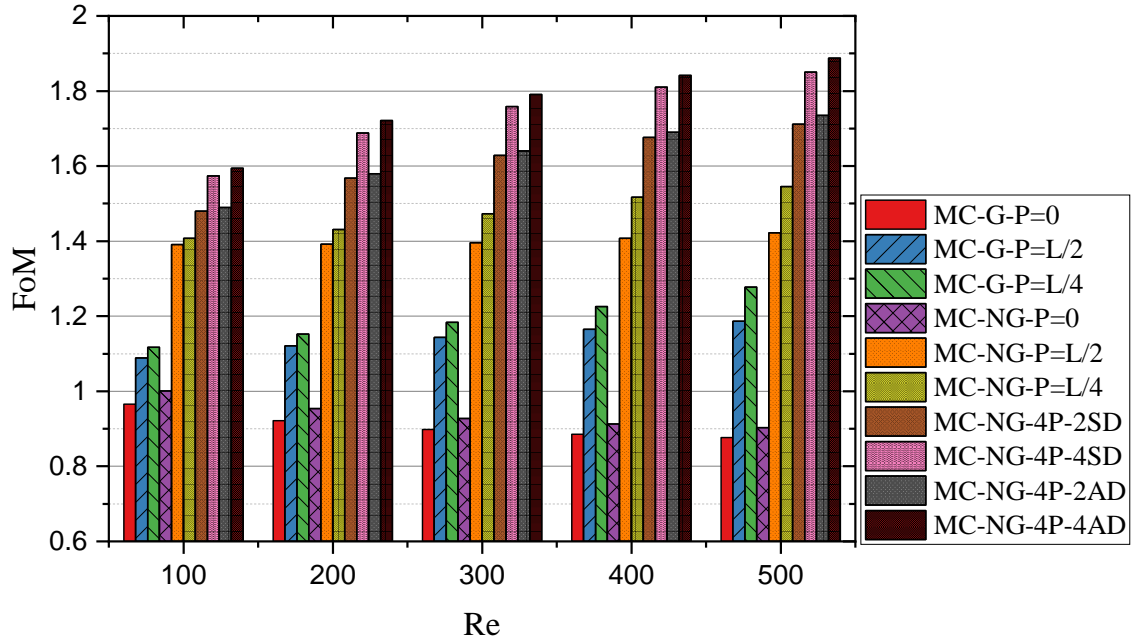
Figure 4.18 Variation of Figure of Merit (FoM) with Reynolds number for various twisted tape designs.

4.6 Conclusions

This article documented the application of conjugate heat transfer and of computational fluid dynamics to examine the effect of twisted tape inserts in a silicon microchannel heat sink, cooled by pure water at an inlet temperature of 298 K, over the Reynolds number range 100 to 500. These simulations combine individual design features of twisted tapes from past work and detail, for the first time, how these features affect the microchannel hydrothermal performance, when applied in isolation and in combination with one another. These features are: (i) radial gaps between the tape edges and the channel inner cylindrical wall, (ii) an axial twist in the tape at the three pitch distances of P=0, P=L/2 and P=L/4, (iii) segmenting the tape by one or two 90 degrees tape pitch angle steps, and (iv) alternating the direction of the helix in consecutive tape segments.

The lowest average bottom wall temperature is predicted by using a tape with no radial gap, of the finest pitch P=L/4, with two 90 degrees tape pitch angle steps, and alternating helix directions. It shows that the design features (i) to (iv) constructively combine to reduce the average bottom wall temperature by 16.13 K below that of the equivalent microchannel without any tape insert, at the same Reynolds number of 500. Using this type of design enables keeping electronic components cooler for a given electrical load. The 16.13 K lower contact temperature is significant in the context of

microchip cooling that typically works at heat sink contact temperatures of around 70 degrees Celsius. Cooler microchips typically are more energy efficient and have a longer life, generating operating cost savings and a lower environmental impact.

The microchannel flow analysis in this work has exposed a mechanism that is thought responsible for this temperature reduction with the alternating tape twist direction of feature (iv). This pitch reversal causes flow separation over the leading edge of the downstream helix. This separation is seen to divert cooler flow running near the axis of the microchannel towards the heated cylindrical microchannel walls. The process results in a more uniform coolant temperature.

The microchannel tape insert with no pitch reversal was predicted to achieve a microchannel wall average temperature reduction of 15.91 K at Re = 500, compared to the configuration without any tape. This appears to be still a very useful temperature reduction and avoids the complexity of assembling tape segments of alternating pitch. The flow analysis has identified to some extent the mechanism behind this performance advantage compared to having no tape insert. The tape twist displaces coolant that is running near the top wall, which is unheated, towards the bottom wall, which is heated, so that the bottom wall has a continuous supply of relatively colder coolant that displaces the coolant being heated on it. Using a finer pitch of P=L/4 enhances this effect compared to the coarser pitch of P=L/2.

Closing any radial gap between the tape and the microchannel cylindrical wall is shown by the numerical simulations to be advantageous both to the thermal performance and to the hydraulic performance of the heat sink. This dual advantage comes from the thermal conduction through the contact between these two surfaces and from the elimination of tape tip gap leakage hydraulic losses.

Inserting a straight tape in the microchannel heat sink delivers a lower temperature than with no tape. This simple arrangement may have manufacturing advantages over the more complex geometries presented herein, but this paper has shown by numerical modelling some performance gains from adding tape twist and 90 degrees angle steps that may meet the lower temperature requirement of future generation microchips.

From a methodological prospective, the Figure of Merit (FoM) used in this paper was found to be a useful performance quality indicator, as it presents the trade-off between any heat removal gain and frictional loss penalty from implementing the tape inserts as a

single, computable quantity. It appears to be a good candidate performance function for computer-assisted optimization processes such as techniques based on artificial intelligence. The conjugate heat transfer analysis and flow simulation has shown to be able to provide sound physical arguments to explain the predicted performance of the different tape inserts, thereby providing robust foundations and a sound physical base for the design and optimization process of microchannel heat sinks.

Chapter 5: Numerical Analysis on the Thermal Performance of Microchannel Heat Sinks with Al₂O₃ Nanofluid and Various Fins

5.1 Introduction

The continuous growth in power and the miniaturization of modern electronics require more effective thermal management systems. Traditional coolants and cooling methods struggle to ensure low temperatures and hence the efficiency and reliability of new high-performance electronic components. The heat sink performance of straight rectangular microchannels is well-documented (Ghani et al., 2017a), optimized, and has limited residual growth potential. Consequently, it is necessary to investigate combinations of new cooling flow passages and of unconventional working fluids to enhance the rate of heat transfer in microchannels, adapting heat exchange features that are found effective in conventional channels (Sidik et al., 2017).

Fin arrays in microchannels expand the heat transfer surface area (Tullius et al., 2011). Ribs and cavities enhance flow mixing and thereby the heat transport away from a hot source (Li et al., 2016). They disrupt the growth of wall boundary layers, creating high local heat transfer regions at the rib and cavity leading edges (Ghani et al., 2017a). Channel bifurcations (Duan et al., 2021) likewise create new boundary layer leading edges with high local heat transfer characteristics. This may explain the better thermal performance of fractal microchannels at increasing channel height to width aspect ratio (Yan et al., 2020). Channel curvature can create Dean vortices to enhance heat transport by flow mixing (Steinke and Kandlikar, 2004).

Sinusoidal waviness in microchannels increases the flow path length, which improves the heat transfer performance by a factor of 1.7 to 2.9 at a pressure loss penalty of 1.3 to 2.0, due to the lengthened flow run (Sui et al., 2010). Transverse waviness causes less pressure loss penalty than longitudinal waviness, while a zig-zag path provides comparatively more heat transport than a sinusoidal path but at a higher pressure loss (Dai et al., 2015). A convergent-divergent, or varicose, channel can increase flow mixing and thereby the heat transport (Li et al., 2019).

A vertical stacking of microchannels creates a double-layered microchannel heat sink, with either parallel flow or counter flow coolants (Srivastava et al., 2021). The

counter flow operation, like in classical heat exchangers, provides greater thermal performance at the expense of greater complexity in manufacturing the channels and in assembling their end connections.

All these approaches can improve the cooling performance, albeit at a pressure-drop penalty, but they need to be combined with other technologies to generate the performance growth capacity required to meet the higher heat flux dissipation demands of advanced electronic components.

Among other technologies, novel coolants with improved thermo-physical properties, such as nanofluids, have been explored. Nanofluids are known to exhibit high stability, flexible properties, minimal particle agglomeration, in addition to an enlarged effective particle surface for optimum interphase heat exchange compared to micrometre-sized particle suspensions (Kakaç and Pramuanjaroenkij, 2009). The limited additional pressure drop and mechanical deterioration make nanofluids particularly useful in compact heat exchanger applications (Sabbaghzadeh and Ebrahimi, 2007). Several hypotheses have been formulated to explain the thermal properties of nanofluids based on micro-scale mechanisms. These mechanisms include clustering, particle rotation, fluid layers particle encapsulation, particle migration, Brownian motion connected with micro convection and corresponding non-uniform property profiles, and the perturbation of the boundary layers (Eastman et al., 2004).

Various studies have investigated the use of nanofluids in microchannels. Pak and Cho (1998) investigated the convective heat transfer behaviours of TiO_2 and Al_2O_3 nanofluids under turbulent flow conditions. Seyf and Keshavarz (2011) studied the thermal and hydraulic performance of Al_2O_3 nanofluid in a counterflow microchannel heat exchanger. Yan et al. (2019) numerically showed an increase in the heat transfer performance of a micro-heat sink resulting from the increase in nanoparticle volume concentration and Reynolds number. Al_2O_3 nanofluid was also investigated by Irandoost et al. (2020), who predicted heat transfer coefficient improvements based on the nanoparticle diameter and volume fraction of Al_2O_3 under laminar flow. Shi et al. (2018) performed further research of heat transfer rates in microchannels with different volume fractions of nanoparticles, showing a non-linear relationship between the increase in thermal performance and the volume fraction. Rahimi-Gorji et al. (2015) assessed the heat transfer properties of a microchannel heat sink using several nanoparticles in water and

ethylene glycol including Cu, Al_2O_3, Ag and TiO_2 nanoparticles, showing that the temperature difference between the working fluid and microchannel heat sink walls decreased at higher concentrations due to the increased Brownian motion of the nanoparticles.

Ambreen and Kim (2018a) studied the combined effects of nanofluids and fins with square, circular and hexagonal outline profiles on a micropin-fin heat sink. Akbari et al. (2016) modelled the heat transfer of Cu nanofluid under turbulent flow in a rectangular microchannel with semi-attached fins, which produced stronger vortices and a better mixture. Wang et al. (2016) investigated the effect of different geometric designs on the thermal and hydraulic characteristics of microchannel heat sinks, showing that the thermal resistance increased by increasing the number of channels, but at the penalty of a considerable additional pressure drop. Sheikhalipour and Abbassi (2016) examined nanofluid heat transfer within trapezoidal microchannels and determined that adding nanoparticles has a marginal influence on the heat transfer if the Reynolds number is not sufficiently high. Toghraie et al. (2018) explored the thermal and hydraulic characteristics in smooth, sinusoidal, and zigzag shaped microchannels using nanofluid. Alipour et al. (2017) examined the effect of a semi-attached T-fin on the thermal properties of a silver-water nanofluid at various volume fractions under turbulent flow in a trapezoidal microchannel, confirming that the convection heat transfer coefficient in the boundary layer increases at increasing Reynolds numbers and volume concentrations of the nanoparticles. Sakanova et al. (2015) examined the combined effect of nanofluids and wavy channel structures, showing that the introduction of nanoparticles is dominant compared to the wavy wall effect.

These studies show that certain flow mixing devices, like fins, can enhance the heat removal rate of a microchannel heat sink at the penalty of additional pressure drop. It is therefore essential to quantify the trade-off between any thermal gain and any pressure drop penalty from these flow trips. To do so, Bahiraei et al. (2019c) used a Figure of Merit, described as the ratio of the heat removal rate gain fraction to the pumping power increment fraction of a microchannel with fins with respect to a baseline channel without fins. A Figure of Merit higher than one indicates improvement with respect to the baseline. Alternatives to the Figure of Merit are reported in the literature, based on comparisons of entropy generation (Bejan, 2013), exergy expenditure and exergy destruction (Liu et al., 2018a), and of the second law efficiency. Improved designs were sought by minimising

the entropy generation (Bejan, 1982), which is made up by a dominant heat transfer contribution and a secondary contribution due to friction (Guo et al., 2018). Increasing the Reynolds number reduces the former, which depends on the temperature gradient in the flow direction (Chen, 2005), but increases the latter (Guo et al., 2018). Entropy generation is high at the microchannel entrance, due to locally high thermal and velocity gradients (Haddad et al., 2004), making this region a prime target for microchannel re-designs. Past entropy minimization driven microchannel re-designs used fan-shaped re-entrant cavities and internal ribs (Xia et al., 2013) and changes to the channel aspect ratio (Abbassi, 2007) to alter the hydraulic and thermal boundary layers. Increasing the wall thermal conductivity (Khan et al., 2006) or the solid wall to coolant thermal conductivity ratio (Abbassi, 2007) lowers the entropy generation in the microchannel. This reinforces the importance of good material selection in microchannel heat sink design.

The trade-off analyses based on the Figure of Merit and its alternatives have led to the identification of heat sink configurations in which inserting fins can enhance the thermal performance at the expense of only a modest pressure drop. These studies have also shown that nanofluid-type coolants can improve the heat exchange process in forced-convection microchannel heat sinks.

To date, no study has been undertaken on combining the three fin designs shown in Figure 5.1 with nanofluids in a rectangular microchannel heat sink. In an attempt to address this gap in the current knowledge, a numerical study is presented herein that considered the thermal and hydraulic performance of a forced convection microchannel heat sink that has no fins (MC-N), or has a rectangular (MC-R), twisted (MC-T), or zigzag (MC-Z) fin, cooled by an Al_2O_3 nanofluid, over the volume fraction range 0 to 3%. The microchannel heat sink in (Sakanova et al., 2015) was selected as a reference case and used to validate the results in the present study. Past numerical investigations of microchannel flow over the Reynolds number ranges 100 to 500 (Ghani et al., 2017b) and 99 to 232 (Sakanova et al., 2015) prompted modelling the flow over the Reynolds number range 100 to 350, to keep the range consistent with past work. The intent is to combine the increased surface area and the vertical motion due to the fins with the increased thermal conductivity of the working fluid, leading to a decreased thermal resistance of the microchannel and a decreased contact temperature of the heat sink base.

5.2 Geometry and boundary conditions

Figure 5.1 (a) illustrates the schematic of a rectangular microchannel heat sink, uniformly heated from below and cooled by nanofluid through flow. 50 parallel rectangular ducts run through a square base silicon block, along x_1. Six out of the 50 ducts are shown in Figure 5.1 (a), for clarity. Due to the relatively large number of parallel ducts, only one duct is modelled and the temperature field is assumed symmetric between adjacent ducts, about the sectional planes shown by the dashed lines in Figure 5.1 (a). Within the microchannel, different fin arrangements are considered, as shown in Figure 5.1 (d-g). These are microchannels (MC) with either no fins (MC-N), or a rectangular (MC-R), or a twisted (MC-T), or a zigzag (MC-Z) fin. The twist and zigzag patterns, shown in Figure 5.1 (b), are spatially periodic and repeat along channel length. The pattern wavelength in x_1 is λ and the pattern amplitudes in x_2 and x_3 are 0 and v, respectively. All microchannels use a top and bottom wall uniform thickness h and all side walls have constant thickness $2w$. Table 5.1 lists the relevant dimensions of the microchannel and of the fins. In order to decrease the thermal stress between the heat sink and chip, all solid parts of the microchannel are made from the same material used in most modern integrated circuit chips, i.e., silicon. The properties of silicon used in the conjugate heat transfer simulation are shown in

Table 5.2. The thermal conditions of the velocity-inlet were set to a uniform total temperature T_{in} = 298 K. The interior walls bounding the fluid region were modelled as no-slip wall type boundaries with Coupled type Thermal Conditions. The front, back, and top exterior walls of the microchannel used a zero heat flux thermal condition, to impose the zero wall-normal temperature gradients specified in section 2.3. A constant heat flux of 150 W/cm^2 was prescribed at the bottom wall. To reduce the computational effort, the computational domain was constrained to one out of the 50 microchannels that make up the heat sink shown in Figure 5.1. The Reynolds number at the inlet of the microchannel heat sink is defined as

$$R_e = \frac{\rho_{nf} u_{in} D_h}{\mu_{nf}} \qquad (5.1)$$

and ranges between 100 and 350. u_{in} is the average fluid velocity at the microchannel heat sink inlet and ρ_{nf} and μ_{nf} are defined in equations (2.17) and (2.20), respectively. D_h is the hydraulic diameter, which is defined by:

$$D_h = \frac{4A}{P} = \frac{4ab}{2(a+b)} = \frac{2ab}{a+b} \qquad (5.2)$$

Table 5.1 Geometric dimensions of the square microchannel heat sink, in mm.

Lx_1	Lx_2	Lx_3	H	h	W	w	T	v	Fin thickness
10	0.35	10	0.25	0.05	0.12	0.04	0.175	0.035	0.01

Table 5.2 The thermo-physical properties of silicon (Wang et al., 2011)

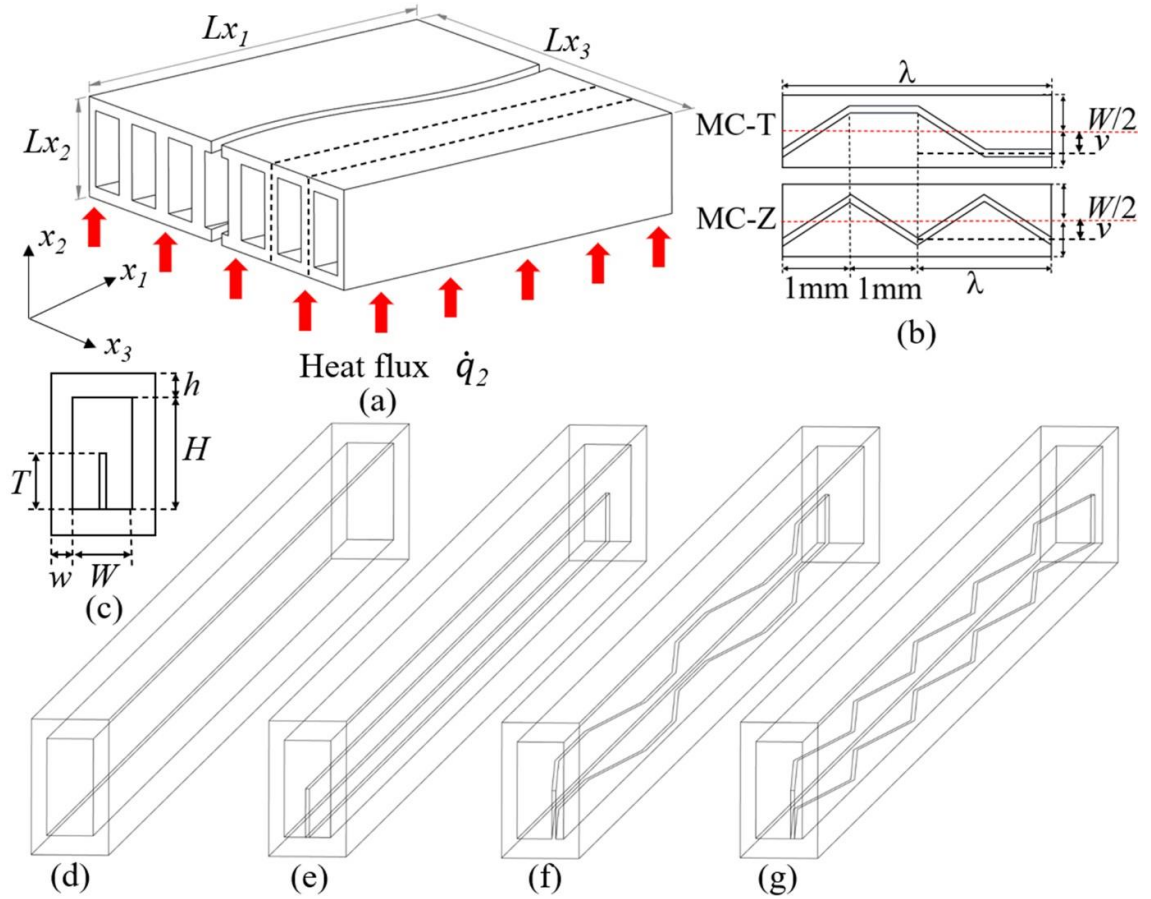|	ρ (kg/m^3)	Cp (J/kg·K)	k (W/m·K)
Silicon	2330	710	148

Figure 5.1(a) Isometric view of the rectangular microchannel heat sink. (b) See-through top view of the twisted and of the zigzag fins. (c) Front view of the microchannel heat sink. (d) Microchannel heat sink without fin (MC-N). (e) Microchannel heat sink with a rectangular fin (MC-R). (f) Microchannel heat sink with a twisted fin (MC-T). (g) Microchannel heat sink with a zigzag fin (MC-Z).

5.3 Numerical mesh

The numerical mesh is fully hexahedral in the solid and the fluid regions of the computational domain of Figure 5.1 (a). Figure 5.2 shows the mesh structure of the four configurations, MC-N, MC-R, MC-T, and MC-Z. The mesh spacing is uniform along the channel length, in x_1, and height, in x_2. The fin is uniformly discretised across its thickness, in x_3, as are the channel side walls. The x_3 mesh spacing in the narrowest gap between the fin and the side walls is uniform, as shown to the right of the fin in Figure 5.2 (c) and in Figure 5.2 (d). The fluid domain first interior cell x_3 dimension is upper bound limited to the x_3 mesh spacing across the fin thickness. Geometric mesh stretching in x_3 from the solid boundaries allows the x_3 discretization to accommodate the fin thickness, twist, and zigzag. The top and bottom channel walls use the same x_3 discretization of the fluid domain between them. A grid-independence study was conducted for cases MC-N, MC-R, MC-T, and MC-Z using water at the Reynolds number of 250. Figure 5.3 shows the microchannel average bottom wall temperature T_w and the loss in static pressure Δp, between the microchannel inlet and outlet, as a function of the number of unit cells in the numerical mesh. The refinement process of the mesh is done by increasing the number of elements in x_1, x_2 and x_3 directions for all cases. T_w and Δp in Figure 5.3 show no significant difference between 0.8M and 5.2M cells. Therefore, the mesh with 2.3M cells was selected for all cases. The number of elements in x_1, x_2 and x_3 are 600, 64 and 60, respectively.
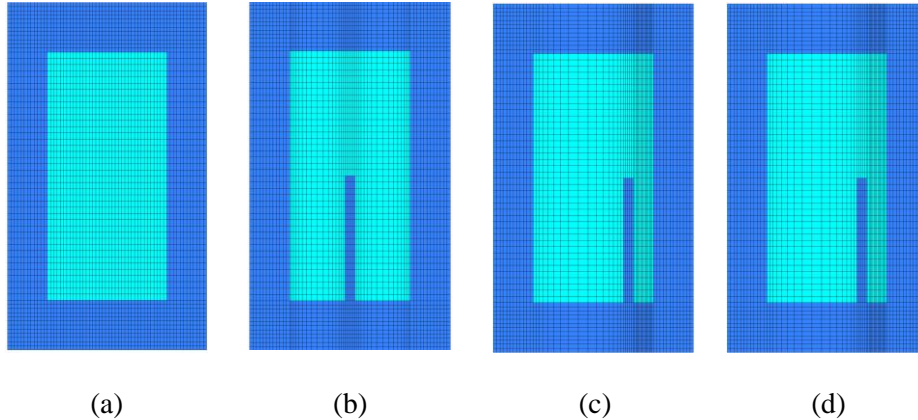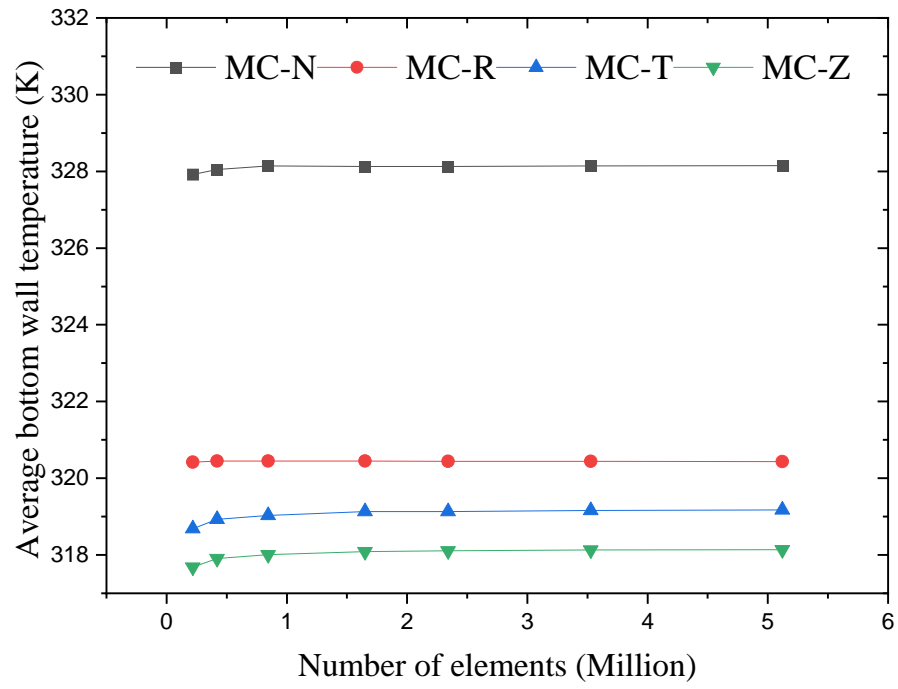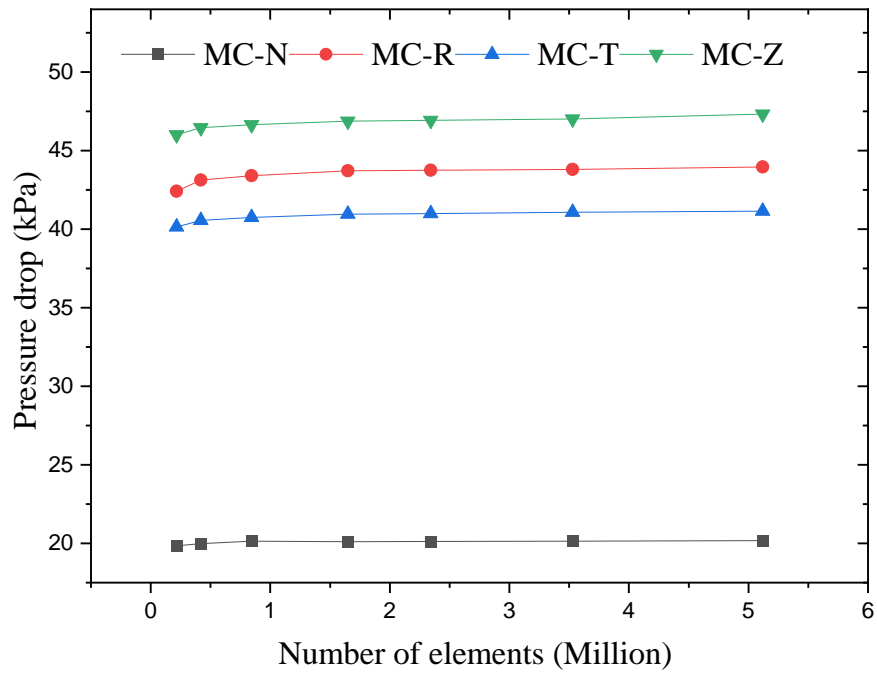

(a) (b) (c) (d)

Figure 5.2 Cross-section mesh structure of (a) MC-N, (b) MC-R, (c) MC-T, and (d) MC-Z.

(a)

(b)

Figure 5.3 Numerical mesh sensitivity of (a) the predicted bottom microchannel wall temperature and (b) the predicted pressure drop for MC-N, MC-R, MC-T, and MC-Z with water at Re = 250.

5.4 Validation

To assess the accuracy of the numerical predictions, the local Nusselt number of MC-N is compared in Figure 5.4 with that obtained from an empirical correlation in Phillips (1990). Both methods predict the same exponential reduction in Nusselt number with increasing distance from the channel inlet x_1. The numerical prediction of Nu is below the empirical correlation estimate along the full channel, by a constant $\Delta Nu \simeq 0.25$. As the local Nusselt number ranges between 5 and 9, this difference amounts to a maximum error of about 5%. The thermal behaviour of a microchannel is expected to change by the presence of a fin. Xie et al. (2015) reported the thermal resistance of a rectangular microchannel with a rectangular fin running from about half-length to the channel exit. The geometry can be considered as a compound of the MC-N and the MC-R joined head to tail and enables testing the consistency of the current numerical method for microchannels with a fin against published work. The thermal resistance is closely related to the microchannel bottom wall to coolant temperature difference by equation (2.25). By matching the specific geometry in Xie et al. (2015), Figure 5.5 shows that the temperature differences predicted by the current numerical model and the ones estimated from Xie et al. (2015) are in close agreement over the Reynolds number range 250 to 350. This builds confidence in the current method of estimating the thermal parameters of microchannels with and without a fin.

Figure 5.6 compares the numerical predictions of the static pressure drop across MC-N against that from an empirical correlation by Steinke and Kandlikar (2006), for pure water, and against numerical simulations at $\phi = 0$ and 5% nanoparticle volume fraction in Sakanova et al. (2015). The empirical correlation by Steinke and Kandlikar (2006) accounts for the channel aspect ratio (W/H) both in its friction loss term and in its channel entry major loss term, where the Hagenbach factor (Steinke and Kandlikar, 2006) is used. Over the Reynolds numbers range 100 to 350, the static pressure drop shows good agreement among the numerical predictions and the empirical correlation, for $\phi = 0$. At $\phi = 5\%$, both numerical predictions report a greater pressure loss with the nanofluid running through the rectangular microchannel than with pure water and both simulations at $\phi = 5\%$ predict the same rising trend with increasing Reynolds number. Using the specific geometry of the partially finned microchannel by Xie et al. (2015), essentially the same pressure drop is predicted as that reported in (Wang et al., 2020). This indicates that the

proposed model can correctly predict the thermal and hydraulic performance for a reliable comparative evaluation of the various designs considered.
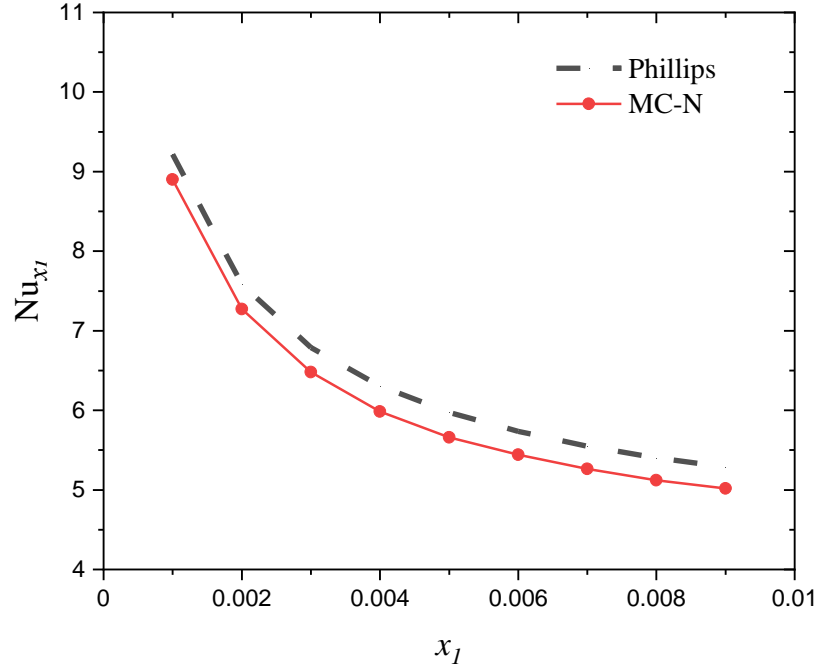
Figure 5.4 Local Nusselt number along the rectangular microchannel heat sink (MC-N). Prediction from the current numerical model (circles) and by the empirical correlation by Phillips (1990) (dashed line) reported as equation (19) in Wang et al. (2020).
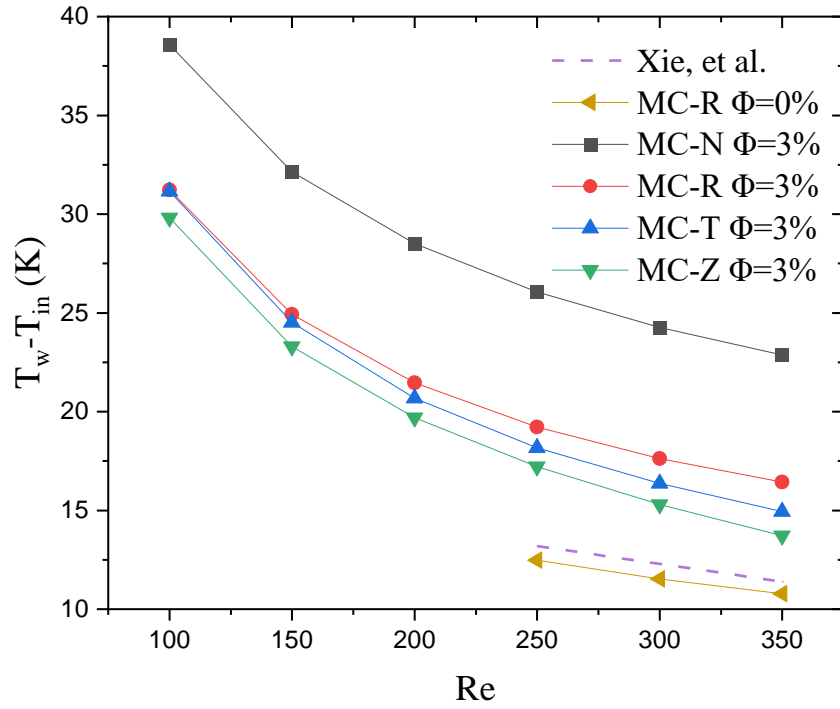
Figure 5.5 Difference between the microchannel bottom wall average temperature and the cooling flow inflow temperature as a function of Reynolds number for MC-N, MC-R, MC-T, and MC-Z at $\phi = 3\%$ Al$_2$O$_3$ nanoparticles. Current model predictions are compared with Xie et al. (2015) at $\phi = 0$ for a partially finned microchannel.
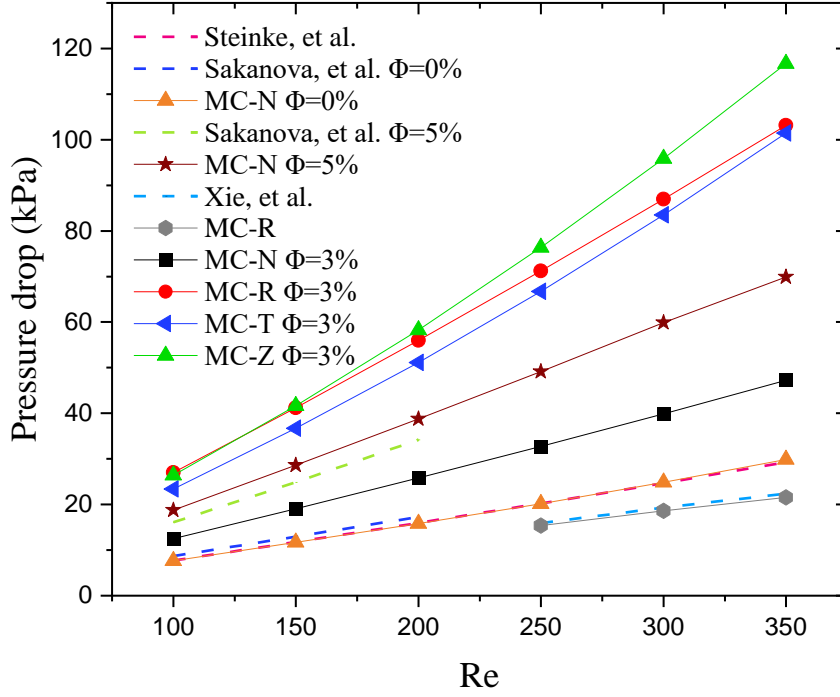
Figure 5.6 Static pressure drop from inlet to outlet of rectangular microchannels with fins (MC-R, MC-T, MC-Z) and without fins (MC-N), at different Reynolds numbers and Al_2O_3 nanoparticle volume fractions. Current model predictions are compared with the empirical correlation reported as equation (12) in Steinke and Kandlikar (2006) or MC-N at $\phi = 0$, with numerical results from Sakanova et al. (2015) for MC-N at $\phi = 5\%$, and with Xie et al. (2015) for a partially finned microchannel similar to MC-R at $\phi = 0$.

5.5 Results and Discussion

This section reports the thermal and the hydraulic performance of the microchannel heat sink with different fin designs and nanoparticle concentrations. It concludes with considerations of the second law efficiency.

5.5.1 Effects of fin design on the microchannel heat sink temperature

Figure 5.7 compares the temperature distribution on cross-sections in the $x_2 = 0$ and $x_3 = 0$ planes for the four different fin configurations, MC-N, MC-R, MC-T, and MC-Z. The Reynolds number and nanoparticle concentration are fixed at 350 and 3%, respectively, in this comparison, but similar conclusions can be drawn for all other regimes and working fluids investigated. The results show that the temperature for all designs increases monotonically from the inlet to the outlet, and that the highest temperature is predicted at the bottom wall near the outlet. Cases MC-Z, MC-T, and MC-R display lower solid wall temperatures towards the outflow compared to MC-N. This indicates a lower thermal resistance across the working fluid thermal boundary layer, resulting in a cooler

91

bottom wall. The average bottom wall temperature in the MC-Z, MC-T and MC-R configurations is consequently lower than in MC-N, due to the presence of the fins in each case. The MC-Z configuration provides the most desirable solid wall temperature distribution among the four configurations as it keeps the microchannel heat sink walls temperature lower than the other designs.
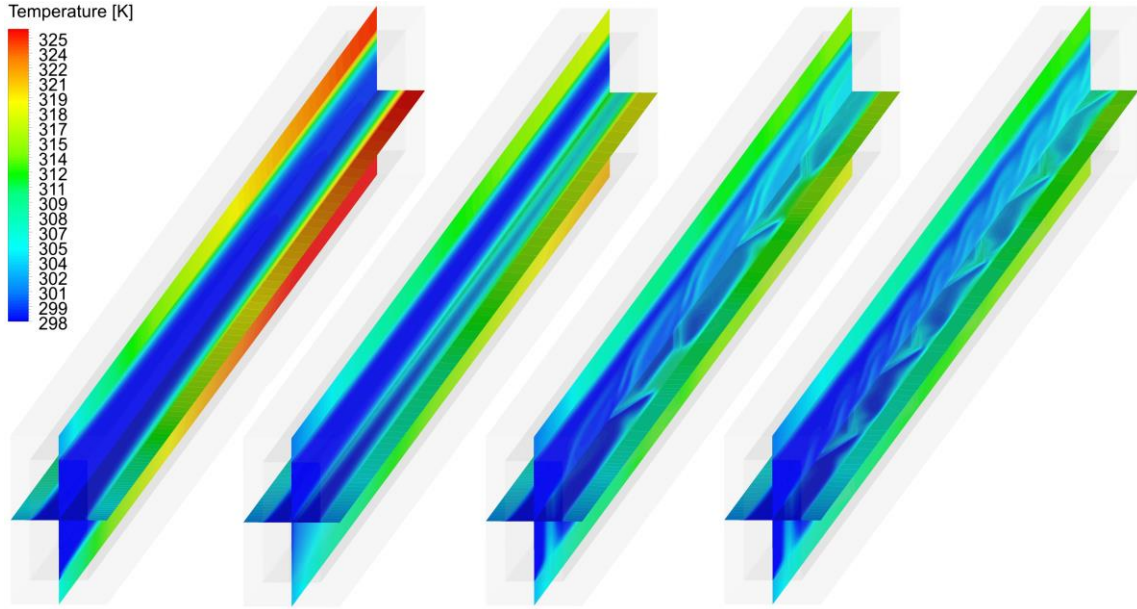
Figure 5.7 Temperature colour iso-levels for MC-N, MC-R, MC-T, and MC-Z at ϕ = 3% Al$_2$O$_3$ nanoparticles at a Reynolds number of 350. $x_2 = 0$ and $x_3 = 0$ planes.

The analysis of the temperature range in the solid part of the microchannel heat sinks yields similar results. Figure 5.8 illustrates the temperature distributions on the cross-sectional plane at $x_1 = 5$ mm from the inlet, for the MC-N, MC-R, MC-T, and MC-Z configurations at Re = 350 and $\phi = 3\%$ of Al$_2$O$_3$ nanoparticles. The predicted temperature at the bottom wall of MC-Z is the lowest of the four configurations, followed by MC-T, MC-R, and MC-N in ascending order. The microchannel heat sink with the zigzag fin provides the lowest resistance to the transfer of heat from the solid to the working fluid among the four microchannel designs at the same heat input rate.
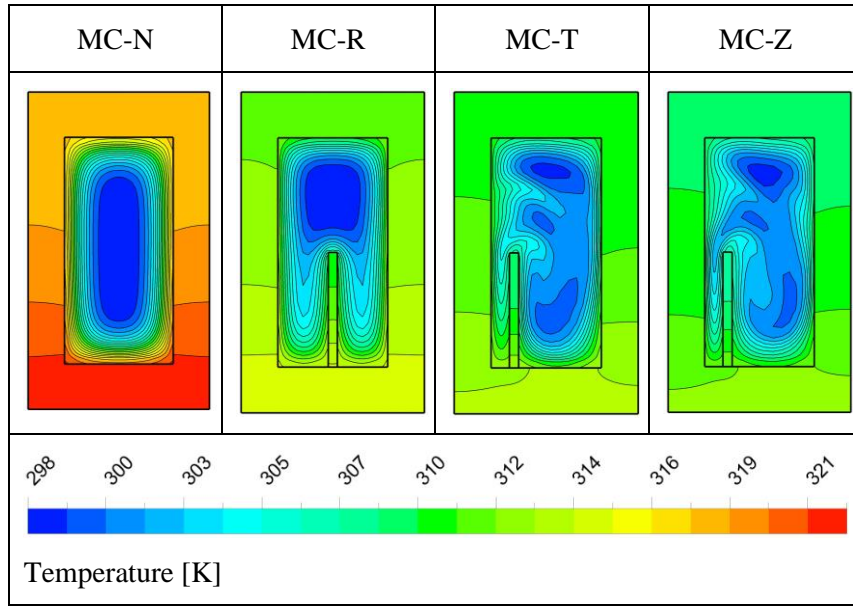
Figure 5.8 Colour iso levels of the temperature distributions for MC-N, MC-R, MC-T, and MC-Z at $\phi = 3\%$ and Re = 350. x_1 plane 5 mm from the inlet.

5.5.2 The effect of fin designs on the fluid flow pattern

Figure 5.9 displays selected streamlines through MC-N, MC-R, MC-T, and MC-Z. The colour of the streamlines is based on the velocity magnitude. The working fluid is Al$_2$O$_3$ nanofluid at $\phi = 3\%$ and the Reynolds number is 350. The streamlines for the MC-N and MC-R configurations follow a similar path but differ in that the magnitude of the velocity through MC-R is larger above the fin and smaller towards the bottom of the channel. Inserting the rectangular fin increases the wetted wall area, which produces more resistance to flow. This flow resistance is uneven across the x_1 planes in that the flow is channelled through narrower passages on both sides of the rectangular fin. As the flow runs through the path of least resistance, it flows preferentially through the top section of the channel, as shown by the higher MC-R velocity magnitude in this region. This is therefore mainly the effect of solid blockage due to the rectangular fin. The streamlines through MC-T and MC-Z differ both in velocity magnitude and direction compared to MC-N and MC-R. The nearly parallel flow in MC-N and MC-R is replaced by a three-dimensional flow, with vortex-like structures forming about the crests of the fins. This indicates that the throughflow is impeded by wake blockage that adds to the solid blockage effect. One vortex-like structure appears to form almost after every reversal of the slope of the fin in the x_3 plane. These slope reversals are more frequent in the zigzag fin geometry due to the smaller fin pitch compared to MC-T. It is therefore likely that this generates a greater wake blockage effect in the MC-Z configuration compared to the other configurations. Although this blockage raises the static pressure drop in the microchannel

and thus the pumping power required, as shown in Figure 5.10, it also provides secondary motion in the x_1 plane that promotes the transport of heat away from the microchannel walls, thus increasing the thermal mixing in the centre of the microchannel. Figure 5.9 also illustrates the influence of the hydrodynamic entry length L_h in the MC-N and MC-R streamlines, which bend slightly towards the centre of the microchannel at the inlet. The hydrodynamic entry length is the axial distance over which the laminar flow develops a streamwise self-similar velocity profile (Cengel, 2010b). In laminar flow, $L_h \approx 0.05\,Re\,D$, which corresponds to $L_h/L_{x_1} = 0.28$ and 0.25 for MC-N and MC-R, respectively.
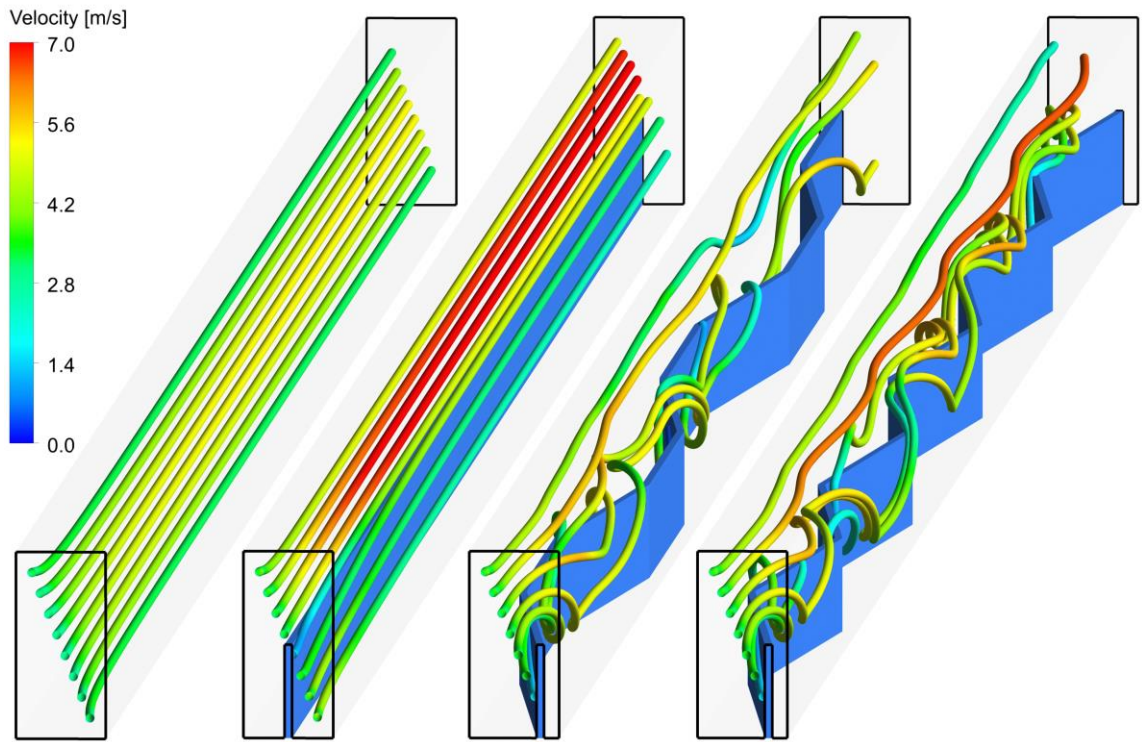
Figure 5.9 Three-dimensional streamlines through MC-N (far left), MC-R (left), MC-T (centre), and MC-Z (right) at $\phi = 3\%$ Al$_2$O$_3$ nanoparticles and Re = 350.

Figure 5.10 (a) illustrates the velocity distribution on the cross-sectional plane at $x_1 = 5$ mm from the inlet, for MC-N, MC-R, MC-T, and MC-Z at $\phi = 3\%$ and at the Reynolds numbers of 350. In this composite figure, the coloured contours denote the velocity magnitude, whereas the vectors denote the in-plane velocity, i.e., the two-dimensional velocity (u_2, u_3) as projected onto the x_1 plane. Figure 5.10 (b) Colour iso-levels of the velocity component u_2 with red corresponding to 0.8 m/s and blue to –1 m/s, thus indicating the direction of rotation of the vortices for MC-N, MC-R, MC-T, and MC-Z at $\phi = 3\%$ and at the Reynolds numbers of 350. The microchannel without fins, MC-N, develops a classical Hagen-Poiseuille type flow in Figure 5.10 (a), featuring a maximum

axial velocity at its geometric centre and a monotonic velocity decay towards its boundaries. Inserting a rectangular fin causes the flow to run preferentially through the top part of the channel, where the flow passage is wider and the flow resistance is lower, as discussed in the context of Figure 5.9. Consequently, MC-R reaches a higher flow speed above the fin than MC-N. Both MC-N and MC-R have very small in-plane velocity components, which are negligible compared to the in-plane motion in MC-T and MC-Z and effectively disappear from the figure when plotted at the same vector scaling length as for MC-T and MC-Z. The in-plane velocity vectors for MC-T and MC-Z show a clockwise circulation centred to the right of the fin tip. This circulation is probably caused by the narrowing of the gap between the fin and the channel left wall and the concurrent widening of the gap between the fin and the channel right wall. The working fluid moves from the narrowing channel section towards the widening channel section, setting up a motion that resembles a wing tip vortex. It is important to note that the centre of the recirculation is offset with respect to the location of maximum velocity magnitude. The MC-Z configuration in Figure 5.10 (b) generates a greater velocity component in u_2 compared to the other configurations. This is likely to be a useful feature with regard to the cooling performance of the channel. It enables the transport of heated fluid away from the walls into a channel region in which a higher x_1 velocity can transport this heat away, towards the channel outlet.

(a)

| MC-N | MC-R | MC-T | MC-Z |

Velocity component u_2[m/s]

(b)
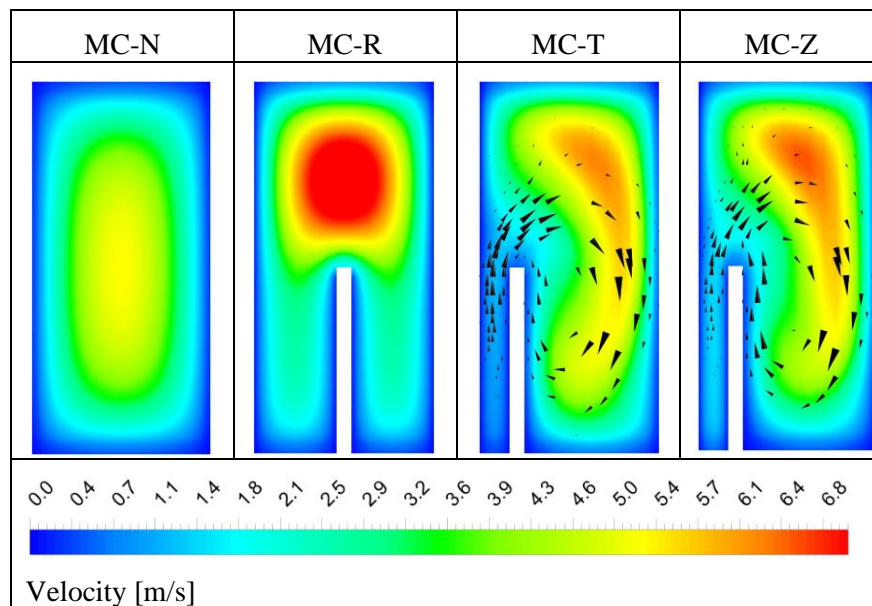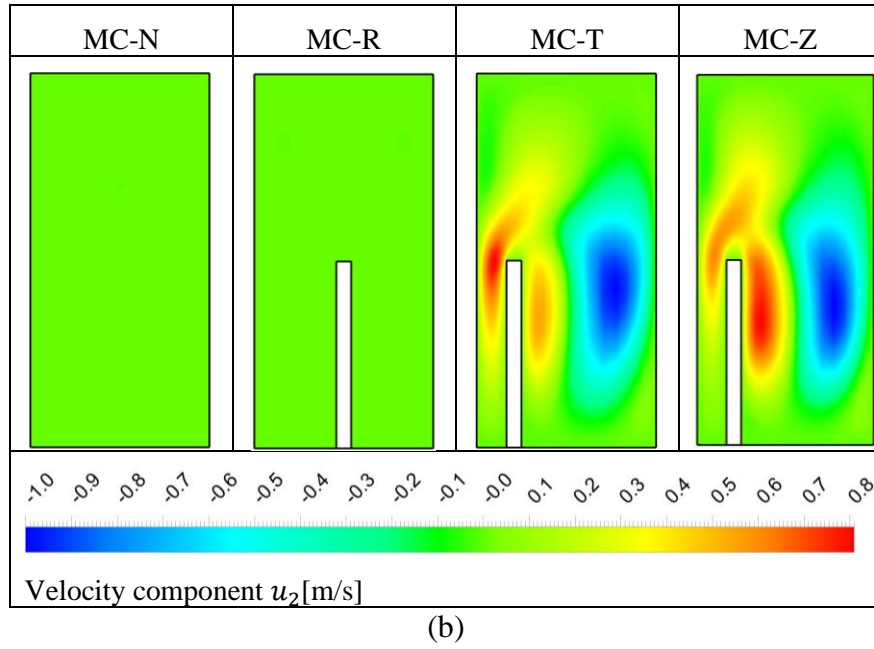
Figure 5.10 (a) Colour iso-levels of velocity magnitude and in-plane velocity vectors and (b) Colour iso-levels of the velocity component u_2 for MC-N, MC-R, MC-T, and MC-Z at ϕ = 3% Al$_2$O$_3$ nanoparticles and Re = 350. Cross-sections at a constant x_1, 5 mm from the inlet.

5.5.3 The Effect of fin design on thermal characteristics

Figure 5.11 shows the predicted change in Nusselt number with increasing Reynolds number from the MC-N, MC-R, MC-T, and MC-Z simulations at ϕ = 3% of Al$_2$O$_3$ nanoparticles. For all four microchannel configurations, the average Nusselt number increases monotonically with Reynolds number. All microchannel configurations with a fin (MC-R, MC-T, and MC-Z) are predicted to give Nusselt number distributions above that of the microchannel with no fin (MC-N) at all Reynolds numbers. Inserting the fin delivers the largest gain in Nusselt number, with further smaller incremental gains in Nusselt number achieved by twisting the fin and then by using a zigzag fin. The main gain associated with the insertion of the fin is likely to be due to the increase in the microchannel internal surface area. Redistributing the heat transfer rate from the microchannel bottom over a larger surface reduces the heat flux through the fluid-solid interface, leading to a lower temperature difference between the flow and the walls. The further gain in the value of the Nusselt number associated with the twisted and zigzag fins is probably due to the secondary flow, as discussed in the context of Figure 5.10. This secondary flow motion generates heat convection streams not only in the channel bulk flow direction, x_1, but also in both the vertical and transverse directions. This motion gives further homogeneous heating of the nanofluid through the microchannel cross-section, as shown by the more homogeneous temperature distributions in Figure 5.8, so that the

96

thermal cooling capacity of the liquid coolant is better used. Below a Reynolds number of 250, the $(W/2 - v)$ narrow gap between the channel internal side wall and the twisted fin restricts the flow through it and hence constrains the convection of heat away from these surfaces. This is evidenced by the elevated coolant temperature through this gap, shown by MC-T in Figure 5.8, compared that through the $(W/2 + v)$ gap. This reduced convection offsets the benefit of the increased internal surface area of MC-T compared to MC-R. At Reynolds numbers above 250, the larger streamwise pressure gradient moves more coolant through the $(W/2 - v)$ narrow gap and this confers a thermal performance advantage to MC-T compared to MC-R. With a volume fraction of 3% at a Reynolds number of 350, the Nusselt numbers of MC-Z, MC-T, and MC-R are increased by 60.01%, 46.26%, and 39.69%, respectively, compared to the MC-N configuration.
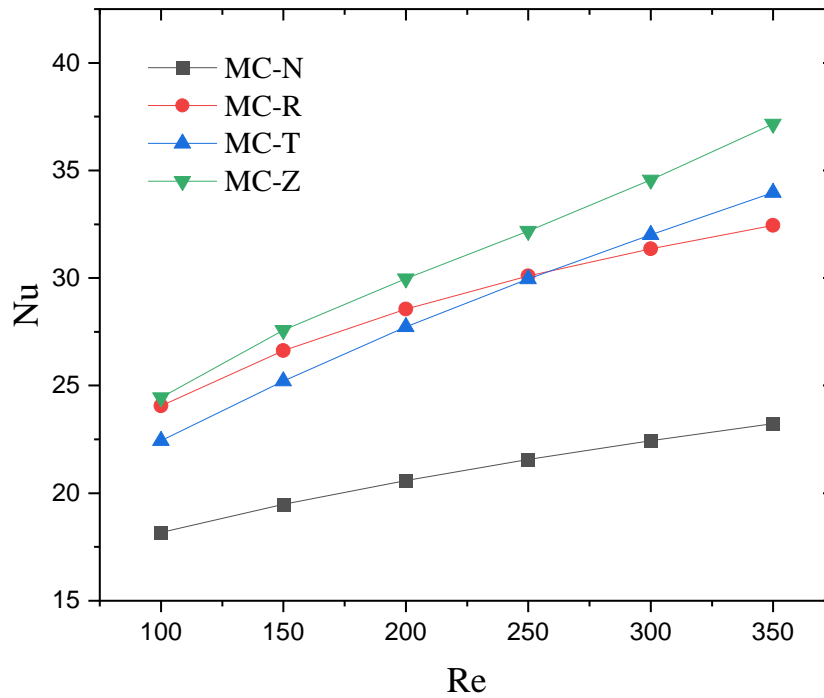
Figure 5.11 Change of the average Nusselt number with increasing Reynolds number for MC-N, MC-R, MC-T, and MC-Z with a volume fraction ϕ = 3% of Al_2O_3 nanoparticles.

Figure 5.5 illustrates how the difference between the microchannel bottom wall average temperature and the inlet temperature of the fluid varies with the Reynolds number. Predictions for the MC-N, MC-R, MC-T, and MC-Z configurations are reported, with ϕ = 3%. The microchannel bottom wall average temperature reduces with increasing Reynolds number, with and without fins. The presence of a fin produces a lower microchannel bottom wall temperature at any given Reynolds number over the range $100 \leq Re \leq 350$. At the Reynolds number of 350, the bottom wall average temperature

for MC-Z, MC-T, and MC-R is predicted to be 9.15°C, 7.92°C and 6.44°C lower than that of MC-N, respectively. Such heat sink contact temperature reductions are of practical interest, since they can benefit the lifespan and the performance of electronic chips. For instance, Sahini et al. (2017) found that increasing the coolant inlet temperature from 25°C to 50°C of an Enterprise-class server increased the processor electric power consumption by 4%. According to equation (2.25), the total thermal resistance of the microchannel is equal to the temperature difference shown in Figure 5.5, divided by the bottom wall heat flux $\dot{q}$. Since the value of $\dot{q}$ was held constant throughout these simulations, the total thermal resistance is simply proportional to $(T_w - T_{in})$ and, therefore, it follows the same trend. At the Reynolds number 350 and $\phi = 3\%$, the average thermal resistances of MC-Z, MC-T, and MC-R are 40.03%, 34.64%, and 28.15% lower than that of MC-N, respectively.

5.5.4 Effects of nanoparticle concentration on thermal characteristics

The effect of changing the volume fraction of the nanoparticles was investigated for the microchannel configuration predicted to deliver the lowest bottom wall average temperature. For this configuration, the nanoparticle volume fractions $\phi = 0$, 1, 2, and 3% were modelled. Figure 5.12 shows the variation of the Nusselt number with Reynolds number for the MC-Z configuration at nanoparticle volume fractions between 0 and 3%. Over this nanoparticle volume fraction range, the Nusselt number increases monotonically with the Reynolds number. Adding Al_2O_3 nanoparticles generates a modest increment in Nusselt number over the full Reynolds number range, an increment that is higher at higher nanoparticle concentrations. Specifically, the Nusselt number for MC-Z with $\phi = 1$, 2 and 3% at the Reynolds number of 350 increases by 0.19%, 1.31%, and 0.67%, respectively. The Nusselt number expresses the ratio between the heat convection rate through the working fluid and the heat conduction rate. The small change in Nusselt number obtained by adding nanoparticles indicates that the flow remains substantially unchanged, that is, that the thermal transport mechanism established in pure water does not change substantially when the nanoparticles are introduced. This knowledge has a practical use, for instance, it enables the characterization of the flow of heat and mass by applying a pure water numerical model. Once a satisfactory flow is found, then wall temperatures can be adjusted by adding small concentrations of nanoparticles without reiterating the flow pattern analysis. A comparison between Figure 5.11and Figure 5.12 shows that the increase in Nusselt number obtained by changing the geometry of the channel is

significantly higher than that obtained by introducing nanoparticles with a volune fraction of up to 3%.
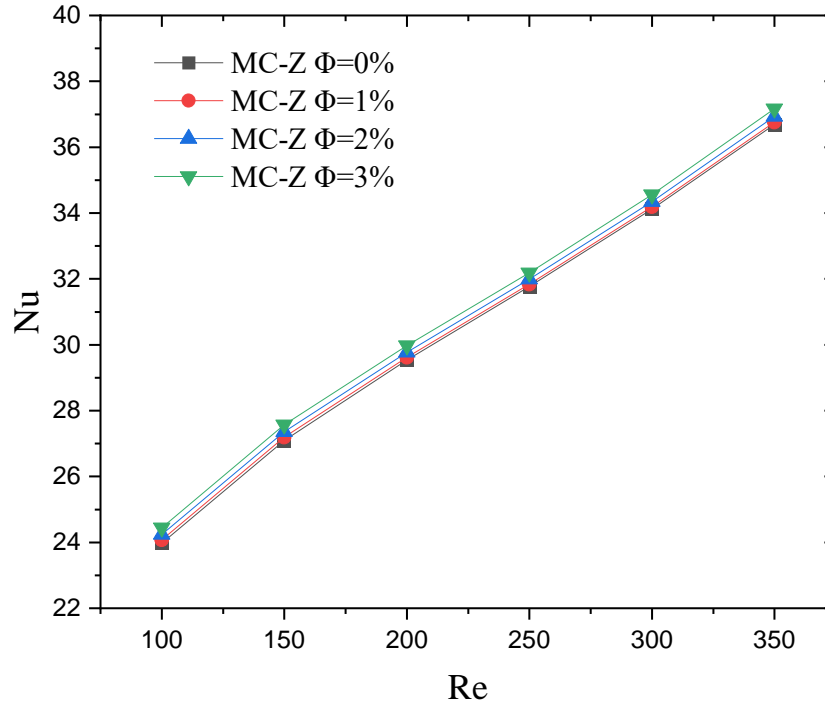
Figure 5.12 Change of Nusselt number with increasing Reynolds number for MC-Z at different volume fraction of Al2O3 nanoparticles.

The effect of adding nanoparticles to the coolant is more substantial on the microchannel bottom wall temperature than on the Nusselt number. Figure 5.13 shows the difference between the fluid inlet and the bottom wall average temperatures for the MC-Z configuration at the four nanoparticle volume fraction from 0% to 3%. The bottom wall average temperature approaches the inlet temperature with increasing Reynolds number. The lowest temperature difference is achieved at the highest nanoparticle volume fraction of ϕ = 3%. This improvement is because of the Al$_2$O$_3$ nanoparticles having a higher thermal conductivity and a lower specific heat capacity than the base fluid, so that they can absorb more quickly heat per unit volume and transport it out of the microchannel heat sink. Comparing Figure 5.12 and Figure 5.13 shows that, whereas only a modest change in Nusselt number is obtained by the addition of nanoparticles within the volume fraction range 0% to 3%, a useful decrease in microchannel bottom wall average temperature can be achieved. The definition of the average Nusselt number from equation (2.24) seems to suggest that the thermal conductivity of the modelled nanofluid is of comparatively greater importance compared to its specific heat capacity effect. This drives a change in the average convective heat transfer coefficient, h_{avr}, that in turn, by

Newton's law of convection, affects the microchannel thermal resistance and hence determines a useful change in the bottom wall temperature. The range of such change, about 6°C in Figure 5.13, is lower but comparable to the change obtained by introducing a fin, about 7.5°C, as shown in Figure 5.5.
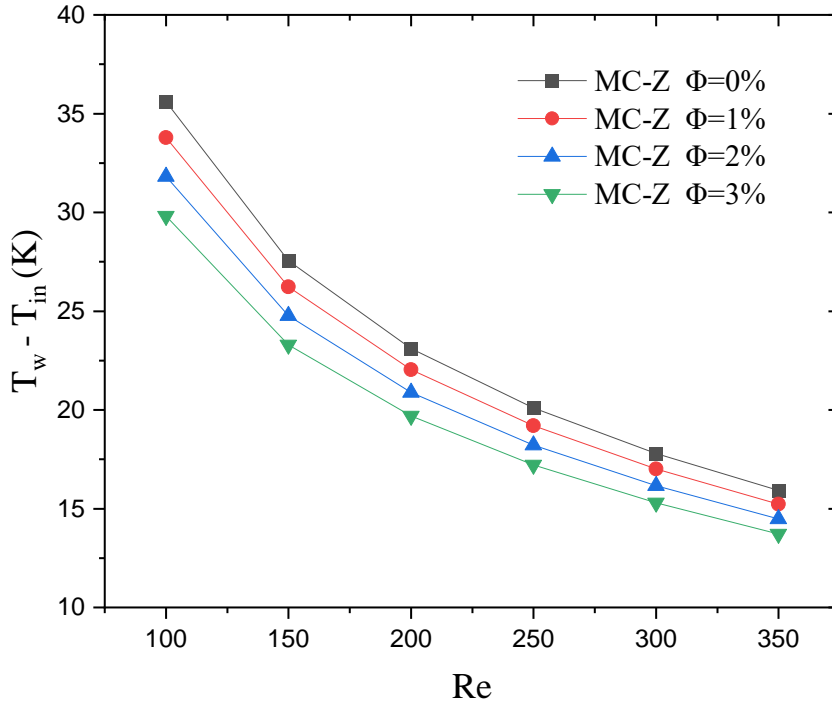
Figure 5.13 Difference between the microchannel bottom wall average temperature and the working fluid inflow temperature as a function of Reynolds number for MC-Z at different volume fraction of the Al$_2$O$_3$ nanoparticles.

5.5.5 Effects of fin design on hydraulic characteristics

Figure 5.6 shows the predicted static pressure drop (Δp) over the Reynolds number range $100 \leq Re \leq 350$ for MC-N, MC-R, MC-T, and MC-Z at $\phi = 3\%$ volume fraction of Al$_2$O$_3$ nanoparticles. MC-Z is predicted to have the largest pressure drop among the four microchannel configurations. This larger pressure drop is a result of increased flow resistance. As discussed in the context of Figure 5.9, both solid blockage and wake blockage effects combine in the zigzag fin case MC-Z to produce a larger hydraulic head loss. The bulk motion of the flow in x_1, which is driven by the drop in static pressure, Δp, is transformed into secondary flow motion by deflection by the fin, as shown in Figure 5.9. Some of this motion is then dissipated by viscosity, both along the wall and within the vortical structures. MC-Z, MC-T, and MC-R all show a higher resistance to flow, that is, a hydraulic performance penalty compared to the microchannel without fins, MC-N. At the Reynolds number of 350 and $\phi = 3\%$, the predicted pressure drop for MC-Z, MC-

T, and MC-R increases by 147.1%, 114.87%, and 118.51%, respectively, as compared to MC-N.

5.5.6 Effects of nanoparticle concentration on hydraulic characteristics

Figure 5.14 shows the variation in the friction factor, f, with Reynolds numbers for MC-N, MC-R, MC-T, and MC-Z with $\phi = 3\%$ of Al$_2$O$_3$ nanoparticles. Consistent with Figure 5.6, MC-Z is predicted to have the largest friction factor among all microchannel configurations due to it having the largest static pressure drop at the same dynamic pressure and channel length Lx_1. MC-N has the lowest friction factor among all the microchannel configurations over the entire Reynolds number range investigated, which reflects its lowest wetted microchannel wall surface area and mainly axial (x_1) flow. The friction factor decreases with increasing Reynolds number for all microchannel configurations as a negative power of the Reynolds number. For reference, Figure 5.14 shows the Darcy-Weisbach friction factor $f = 62.2\ Re^{-1}$ for fully developed laminar flows in a rectangular duct (Cengel, 2010b). This equation is only appropriate to the hydrodynamically fully developed region. Hence, the entry length, $L_h \cong 0.05 Re D_h$, is estimated to calculate the hydrodynamic entrance region (Cengel, 2010b) and the friction factor for MC-N with $\phi = 0\%$ of Al$_2$O$_3$ nanoparticles. The simulated friction factor shows the expected scaling with the inverse of the Reynolds number, in agreement with the friction factor from the Hagen-Poiseuille law. The Darcy-Weisbach friction factor curve is below all predicted friction factors for the finned microchannel configurations, but it is also below that for the no fin MC-N, with $\phi = 3\%$ Al$_2$O$_3$ nanoparticles. The presence of nanoparticles produces a steeper near-wall velocity gradient; this causes additional friction that is not accounted for by the fully developed laminar flow of the Darcy-Weisbach model. At the Reynolds number of 100 and $\phi = 3\%$, the friction factors for MC-Z, MC-T, and MC-R are 72.10%, 49.65%, and 72.19% greater than for MC-N, respectively.
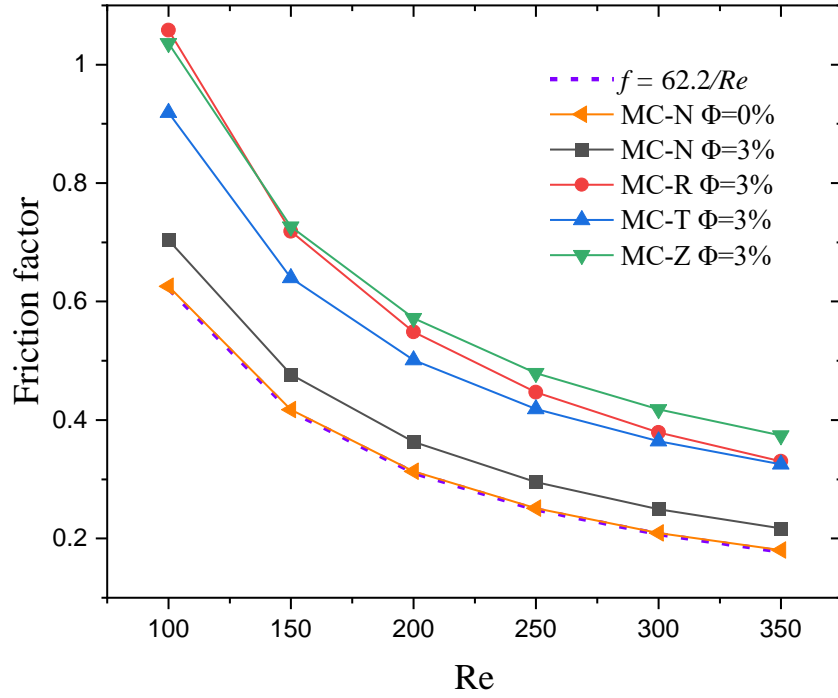
Figure 5.14 Change of friction factor f with increasing Reynolds number for MC-N, MC-R, MC-T, and MC-Z at $\phi = 3\%$ of Al2O3 nanoparticles.

5.5.7 Overall performance improvement

Figure 5.15 compares the Figure of Merit (FoM) for all microchannel configurations (MC-N, MC-R, MC-T, and MC-Z), nanoparticle concentrations, and Reynolds numbers modelled in this work. The intent is to assess the merit of using either a rectangular, a twisted, or a zigzag fin, and/or of adding different volume fractions of Al_2O_3 nanoparticles. The FoM is defined against the reference case MC-N at $\phi = 0\%$, for all Reynolds numbers. The numerical results indicate that all proposed designs have a FoM > 1.0, indicating that they provide comparatively more heat convection performance than the flow resistance penalty they generate. Configuration MC-R reaches a maximum FoM around Re = 250, whereas MC-T and MC-Z increase monotonically with Reynolds number. The mechanism responsible for the enhancement due to the twisted or zigzag fin, as compared to the rectangular fin design, can be explained by the generation of a secondary flow, as discussed in the context of Figure 5.10. This shows how the effects of the microchannel design parameters investigated in this study are strongly dependent on one another and suggests that the design optimization process needs to properly consider these coupled effects.

Overall, for applications in which the electrical resistance increases with temperature, such as for copper-based circuits, a reduced electrical energy consumption from running the circuit at a lower temperature may offset the increase in the pumping energy required through the microchannel heat sink. In such cases, the higher FoM may indicate a better overall energy efficiency. For such applications, Figure 5.15 indicates that the best configuration is that of MC-Z. Moreover, a greater FoM occurs at a Reynolds numbers of 350 for all proposed designs. All values of FoM for MC-R, MC-T, and MC-Z are slightly reduced by increasing the volume fraction concentration of the nanoparticles, which results in greater viscous loss due to friction and in a greater static pressure drop, as shown in Figure 5.14.
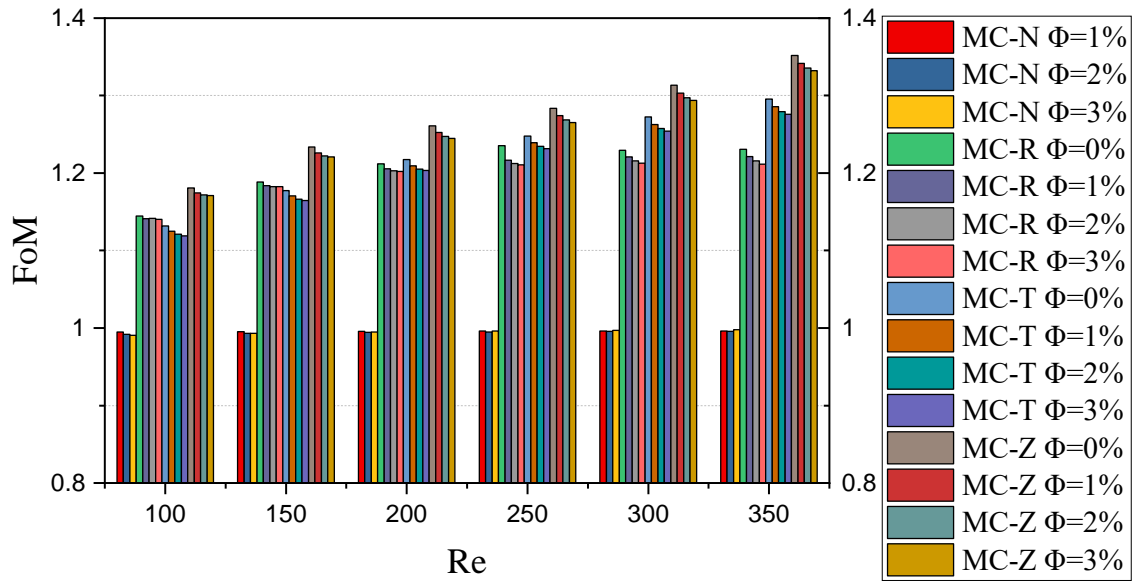
Figure 5.15 Change of Figure of Merit with increasing Reynolds number for MC-N, MC-R, MC-T, and MC-Z, at ϕ = 1, 2 and 3% of Al_2O_3 nanoparticles, referenced to the performance of MC-N at ϕ = 0%.

5.5.8 Exergistic characteristics of the microchannel heat sink

Figure 5.16 illustrates how the exergy expenditure rate by the microchannel heat sink varies with Reynolds number in MC-N, MC-R, MC-T, and MC-Z at ϕ = 0% of Al_2O_3 nanoparticles. The global trend is not monotone, as the rate of exergy expenditure decreases to a minimum around Re = 150 and then increases for higher Reynolds numbers. As shown in Figure 5.16, this is due to the opposing effects that the Reynolds number has on the two integrals in equation (2.32), associated respectively with the reversible work potential of the heat supplied from the hot source and with the reversible work potential of the supplied coolant, respectively. In the first integral, the reduced average bottom wall

temperature lowers the exergy rate supplied, $\dot{E}_{xQ}$, whereas in the second integral the increased kinetic energy of the flow introduces additional exergy, $\dot{E}_{xW}$. Overall, the finned configurations (MC-R, MC-T, and MC-Z) require a lower rate of exergy expenditure than the MC-N channel. The MC-Z configuration has the lowest rate of exergy expenditure due to its lowest bottom wall temperature.
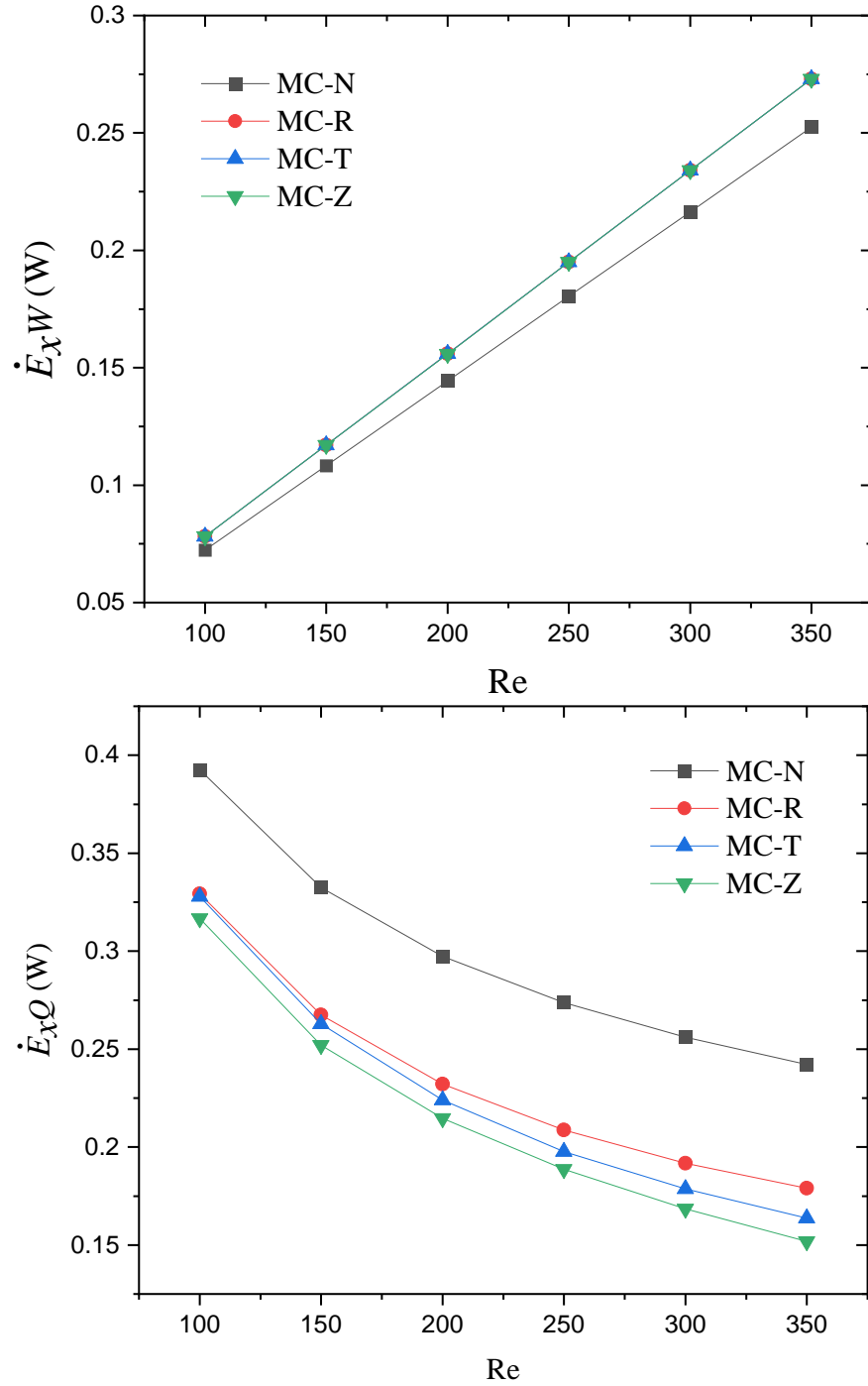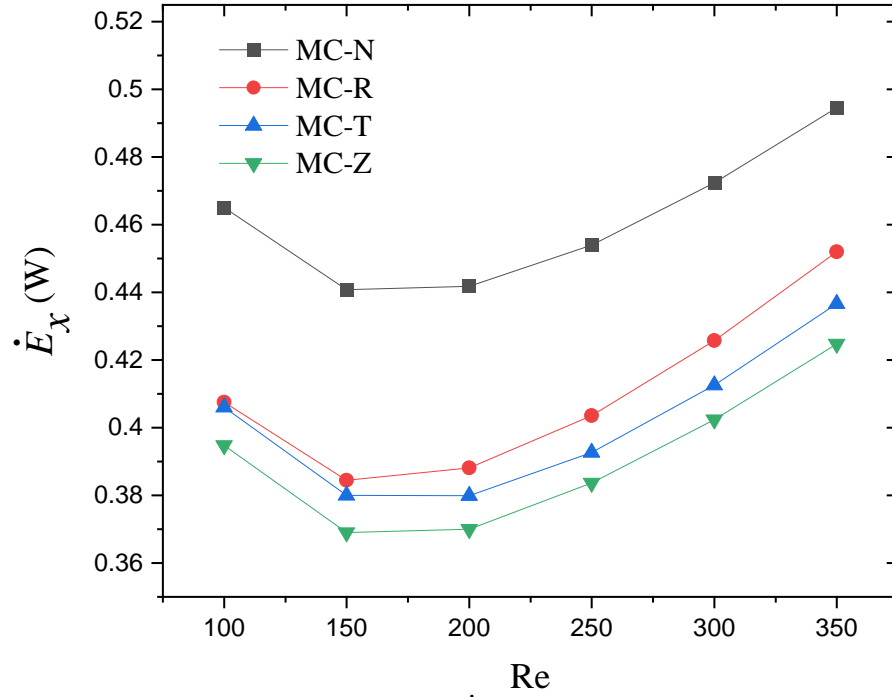
Figure 5.16 The global exergy expenditure rate $\dot{E}_x$ (bottom) for MC-N, MC-R, MC-T, and MC-Z at $\phi = 0\%$. This is the sum of the exergy expenditure rate from the loss of reversible work potential of the coolant, $\dot{E}_{xW}$ (middle), and that from the loss of reversible work potential by the heat supplied by the hot source, $\dot{E}_{xQ}$ (top).

Figure 5.17 (a) shows that the exergy destruction rate decreases monotonically with Reynolds number for all configurations (MC-N, MC-R, MC-T, and MC-Z) for $\phi = 0\%$. This is due to the decrease in the average bottom wall temperature at higher Reynolds numbers that reduces $\left(1 - \frac{T_r}{T}\right)$ in equation (2.30). This term appears to have the strongest effect on $\dot{E}_{xd}$, with the second term ($r\,\psi\,u_i$), associated with the exergy of the coolant only providing a second-order contribution. The MC-Z configuration provides the lowest rate of exergy destruction among the four configurations, due to its lowest bottom wall average temperature. The second law efficiency, η_{II}, based on the exergy expenditure and destruction rates, is shown in Figure 5.17 (b). The microchannel with a straight fin provides a second law efficiency increase of 14% compared to MC-N, at the Reynolds number of 350. With a zigzag fin, the corresponding increment is 15% and, with a twisted fin, it is 12%. Similar results are obtained at lower Reynolds numbers. This means that the reduction in exergy destruction rate due to the presence of the fin outweighs the associated reduction in exergy expenditure rate, yielding a better second law efficiency overall.
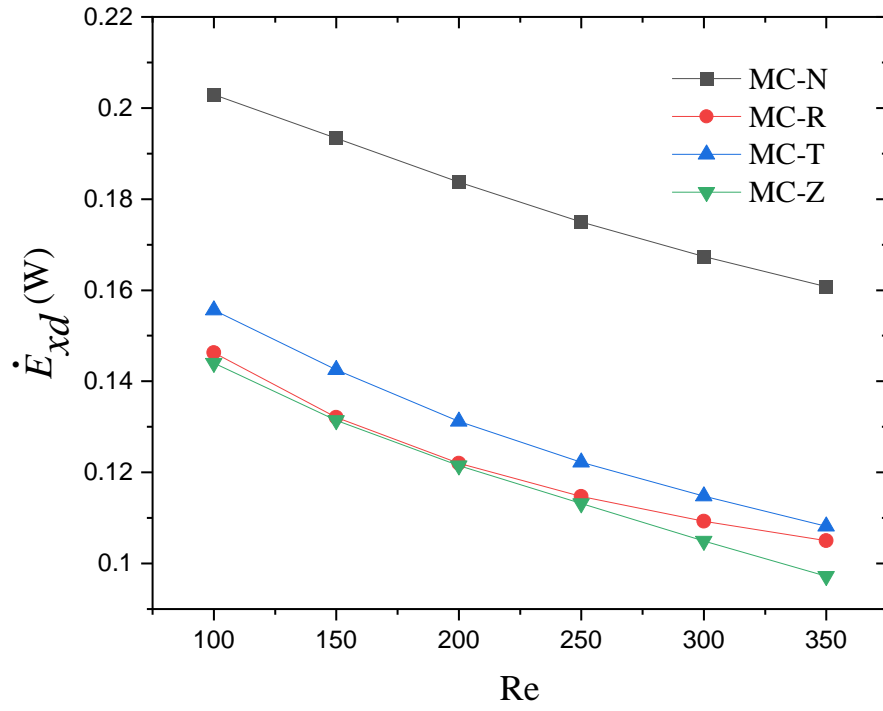
(a)
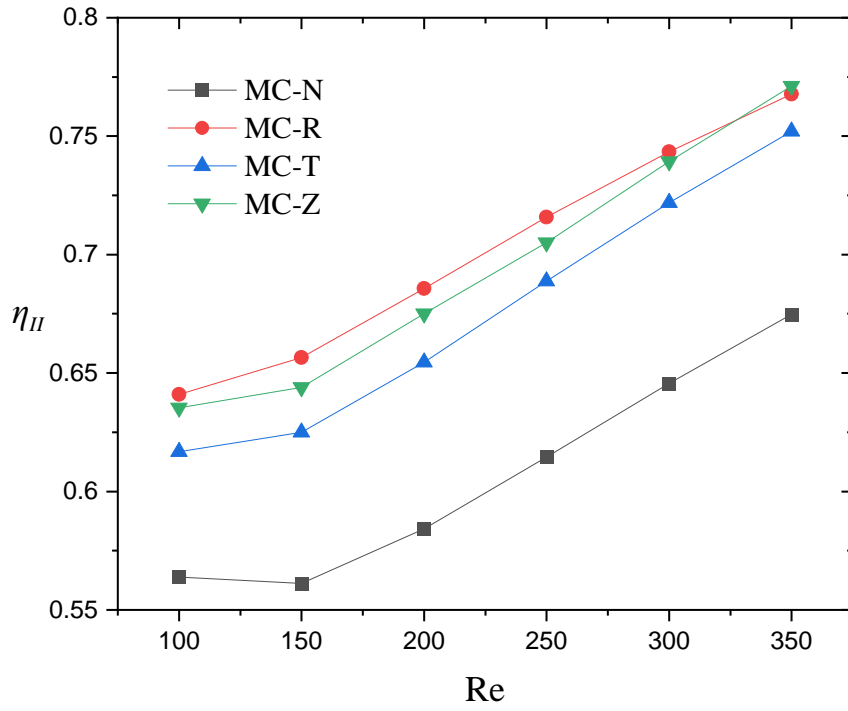
(b)

Figure 5.17 (a) Exergy destruction rate and (b) second law efficiency for MC-N, MC-R, MC-T, and MC-Z at $\phi = 0\%$.

5.6 Conclusions

This paper numerically investigated three different fin designs (rectangular, twisted, and zigzag) for a microchannel heat sink, in combination with a nanofluid as the working fluid. It provides new enlightening insights into the microchannel heat sink cooling process.

The lowest microchannel bottom wall average temperature for a given coolant inflow temperature was predicted with the zigzag fin configuration operating at the highest Reynolds number (350) and with the highest nanoparticle concentration (3%). This reduced base temperature is not only desirable to keep electronic components from overheating, but is also shown to yield an overall increase in second law efficiency.

The advantage of the zigzag design, compared to the other fin designs, is suggested to be due to the combination of an increase in the microchannel internal surface area, leading to a lower temperature difference between the flow and the walls, and of an induced secondary flow, which promotes the fluid exchange and therefore the heat transport between the warmer peripheral regions near the walls and the cooler centre of the microchannel. Based on these considerations, a further study on alternative designs could potentially deliver even more effective configurations.

The addition of nanoparticles produced a useful decrease in the bottom wall average temperature, thanks to the increased convective heat transfer coefficient of the working fluid. However, the change in Nusselt number was modest, due to the concurrent increase in the fluid thermal conductivity. It is therefore important to identify the purpose of the design optimization (in this case the reduction of the temperature of the electronic component) to properly guide the design process.

The rate of heat removal to hydraulic power loss ratio identified by the Figure of Merit is a useful indicator of the overall performance where the solutions adopted to increase the thermal performance also tend to increase pumping power requirements, as it combines the different effects produced by fin configuration, nanoparticle concentration, and Reynolds number in a single scalar performance indicator (FoM).

These observations justify the use of the bespoke model developed in this work that combines different aspects (geometry, nanofluid coolant, and Reynolds number) in one joint optimization process for the thermal and hydrodynamic performance of a microchannel heat sink.

Chapter 6: A novel physically consistent application of the mixture model for modelling nanofluid conjugate heat transfer in minichannel heat sinks

6.1 Introduction

The performance growth and size reduction of micro-electronic devices, such as computer cores, are currently limited by the ability to dissipate the heat produced by the supplied electrical power, through a conventional air-cooled heat sink. There is therefore a sustained research interest in water-based liquid coolants for mini/microchannels cooling systems, owing to the higher specific heat capacity of water compared to air. Water-based suspensions of nanoparticles, referred to as nanofluids, have an even better cooling potential. Compared to the base fluid (water), the nanofluids can extract more heat for the same volume flow rate. Many studies have investigated nanofluids by way of experiment and/or simulation. As the tracking of individual nanoparticles by an Eulerian-Lagrangian approach remains computationally expensive, nanofluid numerical computations use either a single-phase or a two-phase approach.

In the single-phase approach, the suspension of nanoparticles in a base fluid is assumed to be homogeneous and the nanoparticles are assumed in thermal equilibrium with the base fluid (Sidik et al., 2016). The nanofluid is replaced by a single fluid of equivalent thermophysical properties to the ones of the suspension, determined from experiment or by the physical model. The accuracy to which the thermophysical properties of the single fluid are estimated is very important for this type of flow simulation. Santra et al. (2009), Koo and Kleinstreuer (2005) and Xuan and Roetzel (2000) used this single-phase approach, which is relatively computationally inexpensive and has shown to reproduce flow predictions close to experimental measurements.

The single-phase approach is popular for modelling the nanofluid flow for electronic core heat sinks. For example, Bhattacharya et al. (2009) examined the laminar forced convective heat transfer of Al_2O_3 nanofluid in a microchannel heat sink of a rectangular cross-section. They found the addition of nanoparticles to be more beneficial to cooling at a lower Reynolds number. Nebbati and Kadja (2015), Ali et al. (2021a) and Ali et al. (2021b) modelled Al_2O_3 nanofluid in microchannel heat sink and showed that the nanofluids can increase the Nusselt number and reduce the heat sink contact surface temperature compared to water, at an acceptable through-flow pressure drop penalty.

In the two-phase approach, nanoparticles and their base flow are split into two separate phases. These phases move and interact according to a volume of a fluid model (VOF) (Rashidi et al., 2018), or a mixture model (Hussien et al., 2016), or an Eulerian model (Akbari et al., 2011), or a Discrete Phase model (Ambreen and Kim, 2018b). Each model is distinct in the way it manages the mass, momentum, and energy conservation of each phase. The mixture model solves one momentum and one energy equation for the mixture, one volume fraction equation, and individual continuity equations for each phase. The phase velocities are then obtained by empirical correlations (Lotfi et al., 2010, ANSYS, 2017). By this, a greater insight into the role of each phase in heat transfer is obtained compared to a single-phase approach (Yang et al., 2016).

Mixture models of microchannel flows have shown heat transfer enhancement with increasing nanoparticle concentration, in Esmaeilnejad et al. (2014), in line with previous findings by Bianco et al. (2009), secondary flow generated by helical inserts, in Narrein et al. (2015), and nanoparticle size effect on heat transport, in Mirmasoumi and Behzadmehr (2008) and in Akbarinia and Laur (2009).

Comparisons between single-phase and two-phase mixture model predictions are shown in Akbari et al. (2012), who report the two-phase model good agreement in Nusselt number in a CuO nanofluid experiment, and in Sidik et al. (2017), where the laminar and turbulent forced convection by the two-phase model was in closer agreement with experiments by Chein and Chuang (2007). Ambreen and Kim (2017) modelled a microchannel cooled by Al_2O_3 nanofluid, showing that single-phase and two-phase mixture models produced a maximum Nusselt number deviation of 11% and 3.2% compared to experiment, respectively. Kumar and Sarkar (2019) modelled the laminar forced convection of Al_2O_3 nanofluids in a minichannel heat sink. The single-phase and mixture models predicted average Nusselt numbers 22.57% and 13.21% different than in experiment, respectively.

The main alternatives to the mixture model for the two-phase approach are compared in Moraveji and Ardehali (2013), where a steady, laminar microchannel flow simulation with Al_2O_3 nanofluid uses the single-phase, VOF, mixture, and Eulerian methods. The two-phase model predictions are in closer agreement to experiment than single-phase model predictions. Naphon and Nakharintr (2015) reported the same finding using TiO2 nanofluids in a minichannel heat sink and so did Moraveji and Ardehali (2013)

by way of applying Al_2O_3 nanofluid in a liquid block. Kurowski et al. (2009) made use of the single-phase, Eulerian–Lagrangian, and mixture models to simulate nanofluid flow inside a minichannel and documented a consistent flow and heat transfer behaviour among the three models. Haghshenas Fard et al. (2010) analysed the 0.2% CuO nanofluid heat transfer inside a tube and found the average relative error between the experiment and single-phase and two-phase model predictions to be 16% and 8%, respectively, with the best performing two-phase model. Kamyar et al. (2012) studied the forced convection of a nanofluid in a horizontal tube using single-phase, mixture and Eulerian two-phase models, showing that the mixture model is more accurate than the other two models.

Whereas the reduced assumptions of the two-phase mixture model compared to single-phase approach can provide higher fidelity predictions, some authors reported over-estimations of the heat transfer with the two-phase mixture model compared to the single-phase approach (Mojarrad et al., 2013). This generates a lack of confidence in the application of the two-phase mixture simulations for modelling microchannel and minichannel heat sink flows.

The main aim of this work is to review the implementation of the two-phase mixture model to microchannel and mini-channel heat exchangers and show that improved heat prediction performance with respect to a single-phase approach can be achieved, when appropriate physical modelling assumptions are made. This provides a significant contribution to the scientific community by identifying how the two-phase model mixture can be used with confidence and exploit its greater fidelity to the physical flow. The main expected outcome is the wider adoption of this higher fidelity model, to provide significant energy savings, longevity, and cost reduction to microprocessor aided technology, now ubiquitous across all industrial sectors.

To reach this aim, this paper provides the following content: Section 2.1.2 Methodology states the two-phase mixture model formulation used in this work, which is essential in a paper aimed at providing an archival reference on how to implement such a model. Within, section 6.2.2 validates the implementation against experimental results recorded by Kumar and Sarkar (2019) in a minichannel cooled by Al_2O_3 nanofluid. Section 6.3 shows a key aspect for obtaining physically consistent and reliable heat transfer model predictions from the minichannel two-phase mixture model, namely to define two fluid phases, the first being water and the second being a suspension of Al_2O_3

nanoparticles in water, modelled as a fluid of equivalent properties. Model limitations with respect to the nanoparticle volume fraction in the second phase and with respect to the size of the nanoparticles compared to that of the 'bubbles' of the second phase are documented.

Section 6.3.4 explores another important aspect of minichannel heat sinks, from the second law of thermodynamics prospective. The heat sink heat extraction process involves the irreversible conversion of higher grade input heat into lower grade output heat, through thermal resistances, and of coolant pumping power into heat, by friction. This can be assessed by means of entropy generation (Bejan, 2013, Bejan, 1996, Balaji et al., 2007) and exergy (Liu et al., 2018a) and by different approaches based on the second law of thermodynamics (Ibrahim et al., 2021, Bahiraei and Mazaheri, 2021, Khaleduzzaman et al., 2016, Zhai et al., 2015, Bahiraei et al., 2019a). Khaleduzzaman et al. (2016) and Bahiraei et al. (2019a) reported an increasing frictional entropy production and a decreasing thermal entropy production with increasing Reynolds number or flow velocity. In a TiO2 nanofluid heat sink model of Khaleduzzaman et al. (2016), the outlet exergy increased with the Reynolds number. Bahiraei et al. (2019a) showed these trends are nanoparticle volume fraction invariant. The current investigation aims to confirm these findings using the physically consistent two-phase mixture model implementation detailed in this work, for a constant minichannel heat flux input of 16.67 W/cm^2, 1% Al$_2$O$_3$ nanofluid, over the Reynolds number range 91 to 455.

6.2 Geometry and boundary conditions

Minichannel heat sink consists of nine parallel rectangular-shaped ducts with a length of 30 mm, a height of 4 mm, a channel width of 1 mm, a fin width of 1 mm, and a channel height of 3 mm. Only one duct is modelled to decrease the complexity and the computational cost. The temperature field is assumed to be symmetric between adjacent ducts, about the sectioned planes shown with dashed lines in Figure 6.1. Table 5.3 shows the thermo-physical properties of the solid domain made from aluminium . The boundary conditions in section 2.3 for the fluid domain are implemented by the velocity-inlet, pressure-outlet, symmetry, and wall boundary types in FLUENT 19.5. At the minichannel inlet, the velocity (u_{in}) is set uniform and normal to the boundary, the inflow temperature is 303.15 K and uniform, and, in two-phase simulations, the second phase volume fraction is set according to Table 2.2. At the pressure outlet, a uniform gauge pressure of zero is applied. A steady heat flux input of 16.67 W/cm^2 is prescribed on the base wall and of 0 W/cm^2 on all other exterior walls. The reference absolute pressure is set to 1 bar. The

single-phase approach uses constant values for $\rho_{nf}, Cp_{nf}, \mu_{nf}$ and k_{nf} which are set at the start of the computation by evaluating equations (2.17)-(2.20) with $\phi = 1\%$. The two-phase mixture model uses constant values of $\rho_{bf}, Cp_{bf}, \mu_{bf}$ and k_{bf} for the first phase and constant values for $\rho_{nf}, Cp_{nf}, \mu_{nf}$ and k_{nf} for the second phase, which are also set at the start of the computation by evaluating equations (2.17)-(2.20) with Φ from Table 2.2. These constant properties are space and time invariant in both the single-phase and the two-phase simulations. The Reynolds number referenced to the inlet conditions ranges from 91 to 455 and it is defined as:

$$R_e = \frac{\rho_{nf} u_{in} D_h}{\mu_{nf}} \tag{5.1}$$

where ρ_{nf} is the density of the working fluid evaluated by equations (2.17) with $\phi = 1\%$, u_{in} is the average fluid velocity at the minichannel inlet, and μ_{nf} is the dynamic viscosity of the working fluid evaluated by equations (2.20) with $\phi = 1\%$. The hydraulic diameter (D_h) is

$$D_h = \frac{4A}{P} = \frac{4ab}{2(a+b)} = \frac{2ab}{a+b} \tag{5.21}$$

where, P, a and b are, respectively, the perimeter, width, and thickness of the duct.

Table 5.3 The thermo-physical properties of aluminium (Thomas et al., 2016).

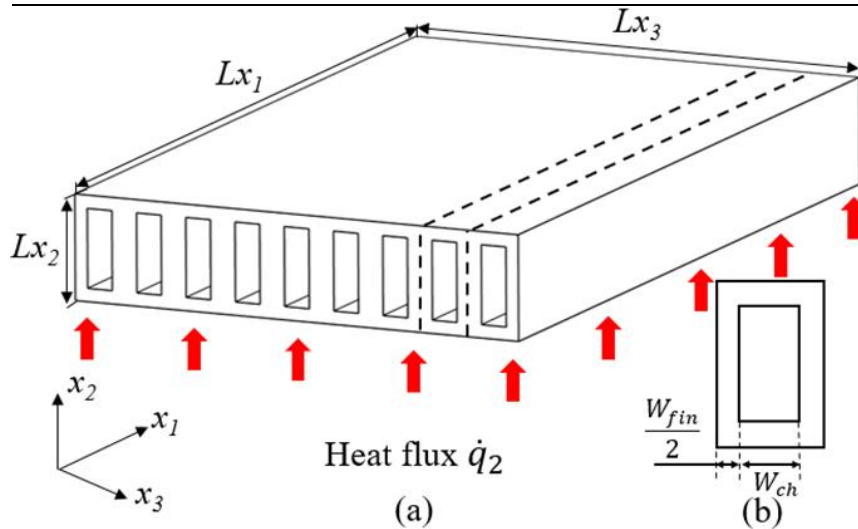|	ρ (kg/m^3)	Cp (J/kg $\cdot$ K)	k (W/m $\cdot$ K)
Aluminium	2719	871	202.4

Figure 6.1 (a) isometric schematic of the rectangular minichannel heat sink and (b) front view of the minichannel heat sink. The heat flux direction is indicated by the up-pointing arrows.

An auxiliary test case is defined to test the model limitations identified in the minichannel heat sink simulations, using a geometry that features greater flow complexity. To this end, simulation is performed of the flow and heat transport over a microscale backwards facing step, which is uniformly heated over its base, as shown by the two-dimensional schematic of Figure 6.2. The inlet channel height $h_u = 0.4$ mm, the step height $h_d = 0.6$ mm, the length of the narrow channel upstream of the step $L_u = 100$ mm, and the length of the wide channel downstream of the step $L_d = 150$ mm. The geometry is tested at a constant Reynolds number of 280, which is based on the inflow conditions and on the hydraulic diameter $D_h = (h_u + h_d)$. The nanofluid, made by a 1% by volume suspension of Al_2O_3 nanoparticles in water, flows through the conduit. A constant heat flux $\dot{q}_2 = 30$ kW/m^2 is applied to the bottom wall, as in Ahmed et al. (2018). Further details are provided in Kherbeet et al. (2014) and Klazly and Bognar (2022) where both measurements and numerical predictions are available, for comparison purposes.

Considering purpose of this auxiliary test case of addressing the model limitations in the presence of greater flow complexity, this computation is limited to the flow domain, which removes the requirement of solving a conjugate heat transfer problem through the solid walls. To this end, the single-phase approach of section 2.1.1 and the two-phase mixture model of section 2.2 are used, together with the nanofluid model of section 2.2. At the inlet, boundary condition 1 of section 2.1.1 is used. At the outlet, boundary condition 2 of section 2.1.1 is used. The bottom wall is modelled with the no-slip boundary condition and $-k_f \frac{\partial T_f}{\partial x_2} = \dot{q}_2$. The remaining walls are modelled as no-slip and adiabatic, by which $u_1 = u_2 = 0$ and $\frac{\partial T_f}{\partial x_n} = 0$. where n is the coordinate normal to the wall.
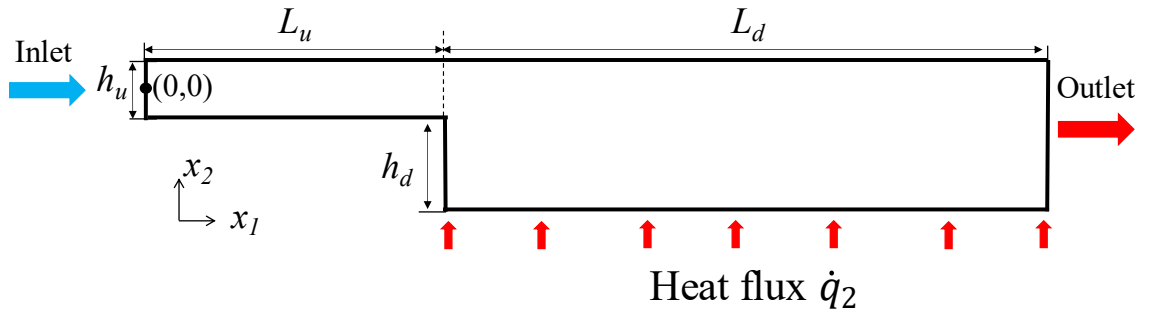
Figure 6.2 Two-dimensional schematic diagram of a horizontal backward-facing step. The schematic is enlarged vertically, for illustration purposes. The heat flux direction is indicated by the up-pointing arrows.

6.2.1 Numerical mesh

In this work, the rectangular prism shape of the minichannel enables the use of a topologically simple hexahedral computational mesh. Such mesh can provide a better computational accuracy and an improved convergence speed over tetrahedral and/or mixed element meshes in simple geometries (Viceconti et al., 1998). The sensitivity of the predictions to the level of spatial mesh refinement was determined by comparing the numerical results from six computational meshes ranging from 0.24 million cells and to 1.74 million cells. Predictions were obtained of the average minichannel bottom wall temperature and of the inlet to outlet pressure drop, at the coolant Reynolds number of 274, coolant inlet temperature of 303.15 K, base heat flux input of 16.76 W/cm^2, and with a suspension of 1% Al$_2$O$_3$ nanoparticles in water. The single-phase approach and the two-phase mixture model were both used, the latter with a combination of second phase volume fraction $\alpha_{nf} = 10\%$ and of second phase nanoparticle volume fraction $\Phi = 10\%$, and with ($\alpha_{nf} = 1\%, \Phi = 100\%$). Figure 6.3 (a) and (b) indicate differences among the models in the average minichannel bottom wall temperature and in the pressure drop, but for each model the predictions become substantially mesh independent above 1.12 million cells. Consequently, the mesh with 1.12 million cells is used throughout the remainder of this investigation. The number of elements in x_1, x_2 and x_3 are 600, 66 and 34, respectively. Figure 6.4 shows the three-dimensional structure of this mesh at the minichannel inlet.
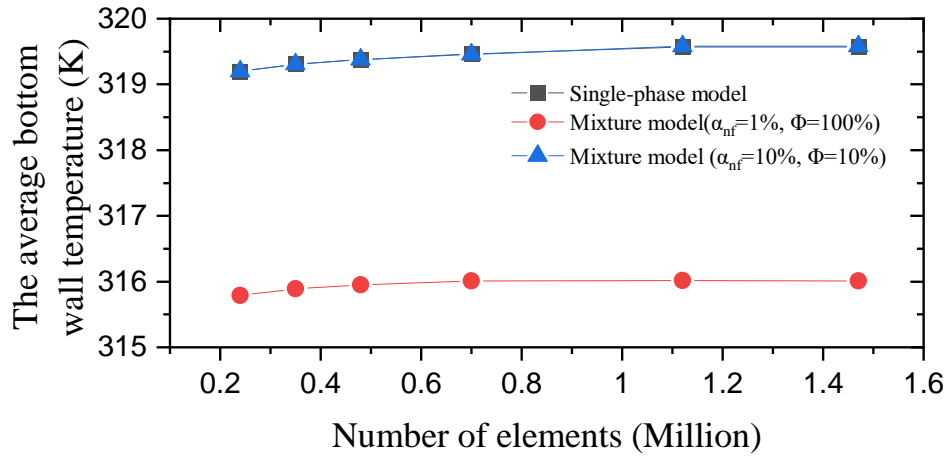
(a)
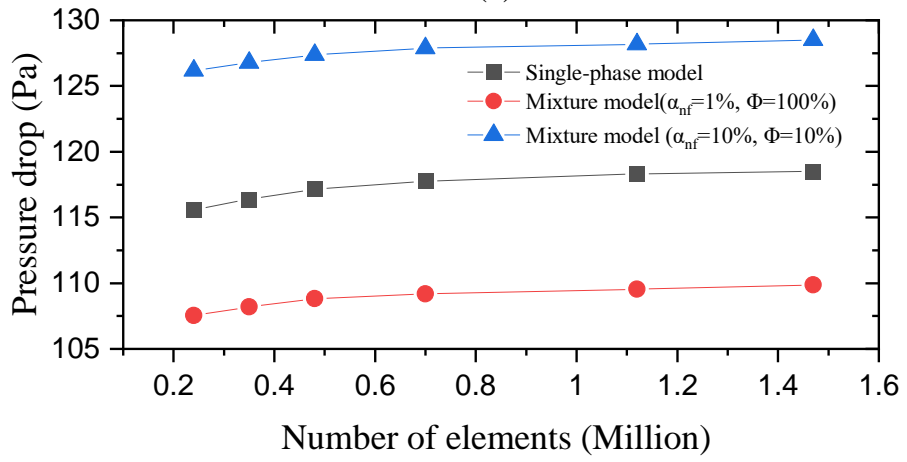
(b)

Figure 6.3 Mesh dependence of (a) the average bottom minichannel bottom wall temperature and (b) the inlet to outlet pressure drop.
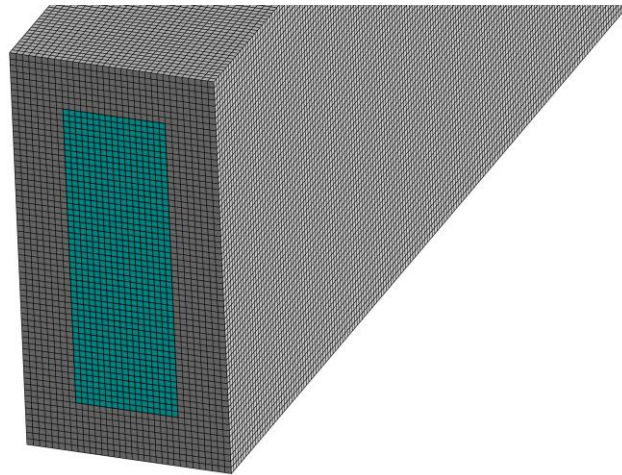
Figure 6.4 Three-dimensional mesh structure of the minichannel heat sink.

Figure 6.5 shows an example of the convergence history with the two-phase mixture model. In this run, the minichannel through flow at a Reynolds number of 455 is simulated with a second phase volume fraction α_{nf} of 4% and with $\Phi = 25\%$. The residuals for continuity, x-velocity, y-velocity, z-velocity, and energy equations reduce monotonically below 10^{-6} in less than 100 iterations. This indicates an appropriate convergence of the results for the purpose of comparing them against corresponding ones from the single-phase approach and other two-phase mixture model runs.
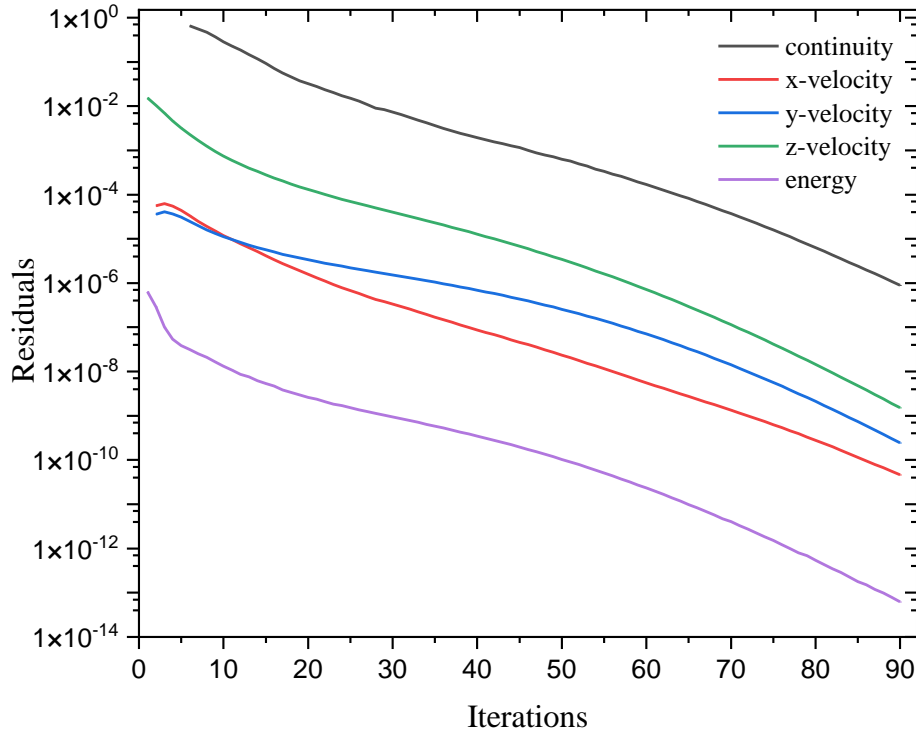
Figure 6.5 Residuals history obtained using the two-phase mixture model at Re = 455 with $\alpha_{nf}=$ 4% and $\Phi = 25\%$.

6.2.2 Validation

To assess the numerical models, Figure 6.6 (compares the average heat transfer coefficient of the minichannel heat sink predicted by the single-phase approach using water as the working fluid against experimental results recorded by Kumar and Sarkar (2019). The single-phase approach predictions are shown to follow reasonably well the experimental results, with a 16.7% maximum discrepancy at the Reynolds number of 92. In addition, Figure 6.6 (b) compares the friction factor from plain water flowing through the minichannel single-phase simulation against the friction factor correlation for laminar square duct flows, the Darcy-Weisbach friction factor $f = 62.2\ Re^{-1}$ (Cengel, 2010b). As this friction factor correlation applies to a fully developed laminar duct flow, f was

estimated from the pressure drop between the end of the hydrodynamic entrance region and the minichannel outlet. The hydrodynamic entrance region length $L_h \cong 0.05 Re D_h$ (Cengel, 2010b). There is good agreement in trend and values between the numerical predictions and the empirical correlation, which both follow the ($1/Re$) proportionality.

The two-phase mixture model was run using water for both phases and produced the same predictions for the average heat transfer coefficient and for the friction factor as the single-phase approach, over the range $92 \leq Re \leq 455$.
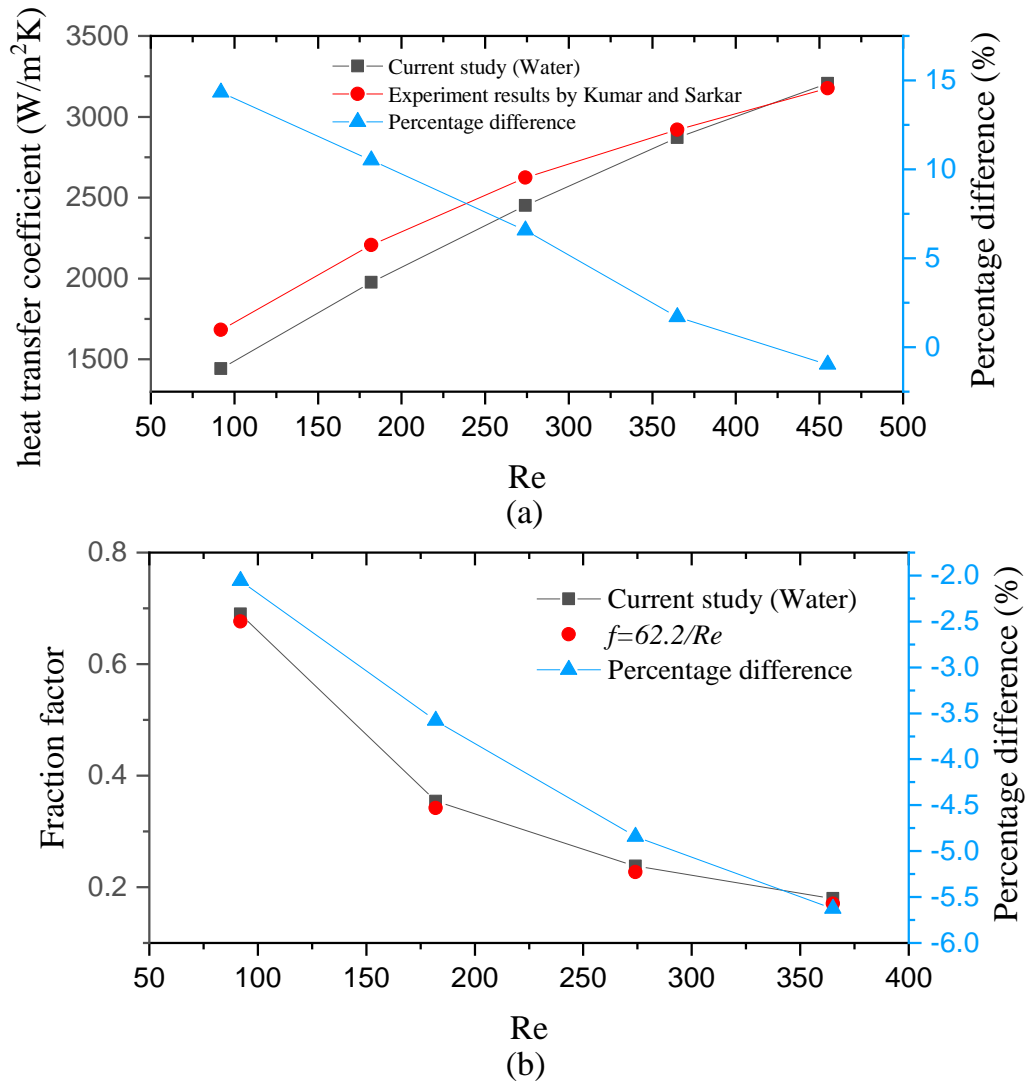
Figure 6.6 Validation of numerical results (a) the average heat transfer coefficient and (b) friction factor

6.3 Results and Discussion

In this section, the influence of Al_2O_3 nanofluid on the thermal and hydraulic characteristics of a minichannel heat sink has been evaluated using both the single-phase approach and the two-phase mixture model.

6.3.1 Effect of the volume fraction of the second phase α_{nf} on the thermal characteristic.

Figure 6.7 shows the average heat transfer coefficient obtained with single-phase approach and with the two-phase mixture model. Different combinations of phase two volume fraction α_{nf} and of phase two Al_2O_3 nanoparticle volume fraction Φ, as defined in Table 2.2, provide the same 1% Al_2O_3 nanoparticle volume fraction in the mixture. The results are compared to the experiments by Kumar and Sarkar (2019), over Reynolds number range 92 to 455. Overall, the average heat transfer coefficient in the minichannel heat sink increases with the Reynolds number, due to the higher velocity providing a stronger heat convection. This improvement in h is similar to that reported in the literature (Kalteh et al., 2012, Kumar and Puranik, 2017). The mixture model with ($\alpha_{nf} = 1\%, \Phi = 100\%$) is shown to overpredict the average heat transfer coefficient when compared to the experiments and to any of the other models, due to the overestimation of the phase interaction between nanoparticles and the base fluid, consistent with the results by Akbari et al. (2011), Moraveji and Ardehali (2013) and Mojarrad et al. (2013). On the contrary, the average heat transfer coefficient from the single-phase approach and from the two-phase mixture model with ($\alpha_{nf} \geq 2\%, \Phi \leq 50\%$) is underestimated, particularly at lower Reynolds numbers. This is in line with the results obtained for water reported in Section 6.2.2 which show a similar underestimation at low Reynolds numbers.

It is observed that the predictions from the single-phase approach and from the two-phase mixture with ($\alpha_{nf} \geq 2\%, \Phi \leq 50\%$) essentially overlap. The close agreement between the two-phase mixture model at ($\alpha_{nf} = 50\%, \Phi = 2\%$) and the single-phase approach at $\phi = 1\%$ shows that the two-phase mixture model predicts the same heat transport as the nanoparticles approach a uniform distribution in the flow, which is what the single-phase approach simulates. The convergence between the two models in their heat transport prediction is an important outcome of this investigation. It shows that the reservations in the application of the two-phase mixture model to minichannel heat

transport problems can be overcome by a judicious model use, as further elaborated later on in this paper.

Figure 6.7 shows that the average heat transfer coefficient predicted by the two-phase mixture model is substantially invariant over a range of α_{nf} and Φ combinations. This is likely to result from the simple geometry of the channel, which promotes the nanoparticle dispersion towards a uniform distribution. The absence of significant flow curvature to drive phase segregation indicates that the mass transport mechanism in this minichannel is unlikely to form areas of high nanoparticle concentration, which the two-phase mixture model is designed to resolve.
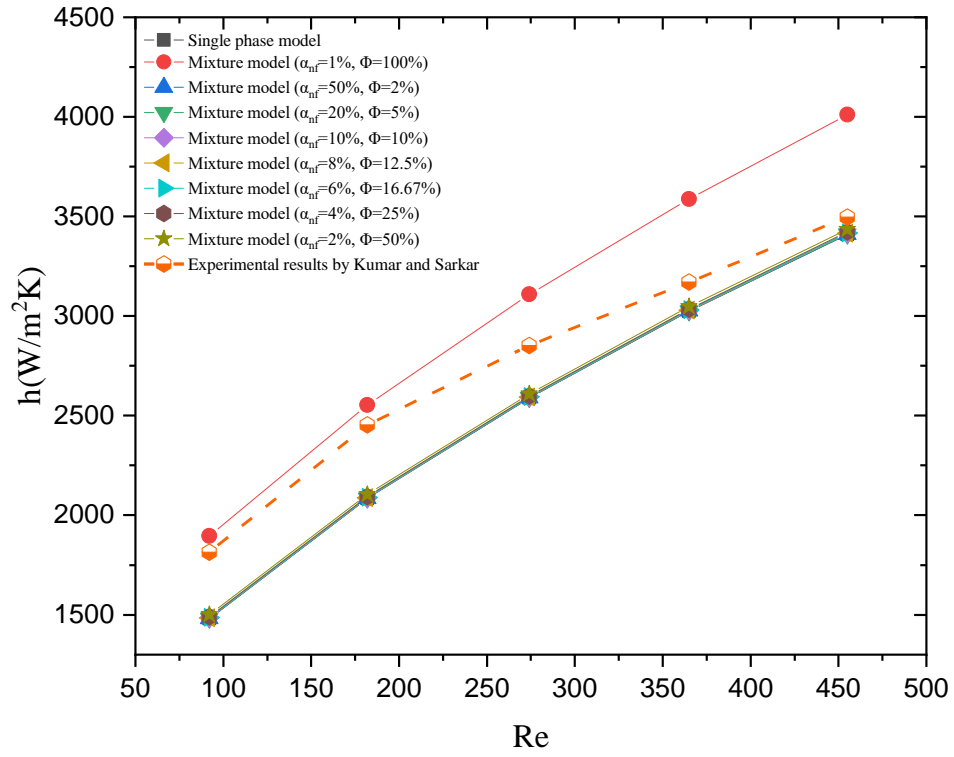
Figure 6.7 Average heat transfer coefficient of the minchannel heat sink from using the single-phase approach and the two-phase mixture model at $92 \leq Re \leq 455$.

6.3.2 Effect of the volume fraction of the second phase α_{nf} on the hydraulic characteristics

Figure 6.8 shows the pressure drop along the minichannel predicted by the single-phase approach and by the two-phase mixture model at the conditions defined in Table 2.2. The results are compared to the experiments by Kumar and Sarkar (2019) in the Reynolds number range 92 to 455 at the same Al_2O_3 nanofluid volume fraction $\phi = 1\%$. The pressure drop in the minichannel heat sink is shown to increase with the increasing

Reynolds number. The single-phase approach and the two-phase mixture model with $(\alpha_{nf} \geq 6\%, \phi \leq 16.67\%)$ underpredict the pressure drop compared to the experiments, and so does the $(\alpha_{nf} = 1\%, \Phi = 100\%)$ two-phase mixture model, as previously reported by Akbari et al. (2012) and Ambreen and Kim (2017). In the two-phase mixture model with $(\alpha_{nf} = 1\%, \Phi = 100\%)$, the second phase is made up entirely of nanoparticles, yet the phase is modelled as a Newtonian fluid, with a finite molecular viscosity. This is an unphysical implementation of the two-phase mixture model, as a volume of nanoparticles packed at 100% volume fraction would respond to stress by a strain rather than by a strain rate. As such equation (2.20) appears to be used beyond its range of applicability. Figure 6.8 shows that the $(\alpha_{nf} = 1\%, \Phi = 100\%)$ prediction is an outlier. Specifically, Figure 6.8 shows a monotonic increment of the pressure drop predicted by the two-phase mixture model with decreasing α_{nf}, down to $\alpha_{nf} = 2\%$, followed by a sharp drop in pressure loss, as α_{nf} is reduced from 2% to 1%, across the whole Reynolds number range 92 to 455. This behaviour typically suggests an inconsistency in the use of the physical model, which this work has identified in the definition of the second phase viscosity.

Concerning the two-phase mixture model with $\alpha_{nf} \geq 2\%$, Figure 6.8 shows that increasing α_{nf} produces pressure drop predictions that monotonically reduce at increasing α_{nf} and that incrementally approach the pressure drop predicted by the single-phase simulation. The closest two-phase mixture model prediction to that from the single-phase approach is that with $(\alpha_{nf} = 50\%, \Phi = 2\%)$, which most closely represents the homogeneous mixing of the single-phase approach among the two-phase mixture simulations. This convergence in predictions provides further confidence in using the two-phase mixture model to perform minichannel flow predictions, provided its modelling assumptions are upheld.

Figure 6.8 shows that, unlike the average heat transfer coefficient, the pressure drop depends on the combination of the phase two volume fraction α_{nf} and of the phase two Al$_2$O$_3$ nanoparticle volume fraction Φ. As the phase two volume fraction decreases below 50%, the pressure drop approaches the experimental results. For $\alpha_{nf} = 4\%$, the mixture corresponds to the case with the highest Φ for which the homogenous model used within a single bubble is valid. For $\alpha_{nf} = 2\%$, the volume fraction of nanoparticles within a bubble is above 30%, beyond the range of applicability of the homogenous model (Xuan

and Roetzel, 2000), and this is reflected by a steep increase in pressure drop compared to the $\alpha_{nf} = 4\%$ case. These results confirm the challenge of modelling nanofluids. As the homogeneous mixture relation between viscosity and nanoparticle volume fraction is not linear, Equation (2.20), the overall pressure drop is sensitive to the second phase nanoparticle volume fraction Φ in the two-phase mixture model.

This means, in principle, that it is possible to cluster nanoparticles to obtain a desired pressure drop independently from the average heat transfer coefficient. This may be obtained by adding a coagulant to the nanofluid to promote flocculation or by adding a surfactant to promote nanofluid particle dispersion. Surfactants appear to be of greater potential benefit to a minichannel heat sink than coagulants, since, by promoting the nanoparticle dispersion, the condition of a homogeneous mixture of the single-phase model could be induced, which Figure 6.8 shows being that associated with the smallest pressure drop, among the physically valid models.
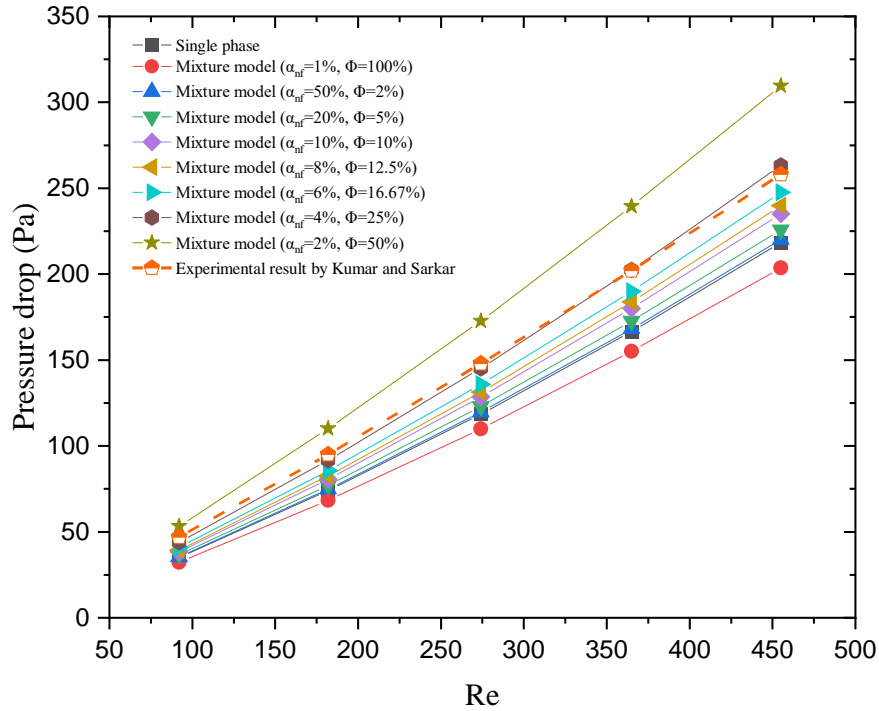
Figure 6.8 Minichannel inlet to outlet pressure drop (Δp) from the single-phase approach and the two-phase mixture model at $92 \leq Re \leq 455$.

The effect of the second phase α_{nf} on the hydraulic characteristics is consistent over the Reynolds number range 92 to 455 and Figure 6.9 enables these appreciation this consistency by providing a larger spread among the friction factor curves at the low end of the Reynolds number range compared to Figure 6.8. The friction factor prediction that

follows most closely the experimental results is that from the two-phase mixture model with ($\alpha_{nf} = 4\%, \Phi = 25\%$) that under-predicts the measured friction factor by 4%. The single-phase model under-predicts the measured friction factor by 16%, and the two-phase model with ($\alpha_{nf} = 1\%, \Phi = 100\%$) under-predicts the measured friction factor by 20%.
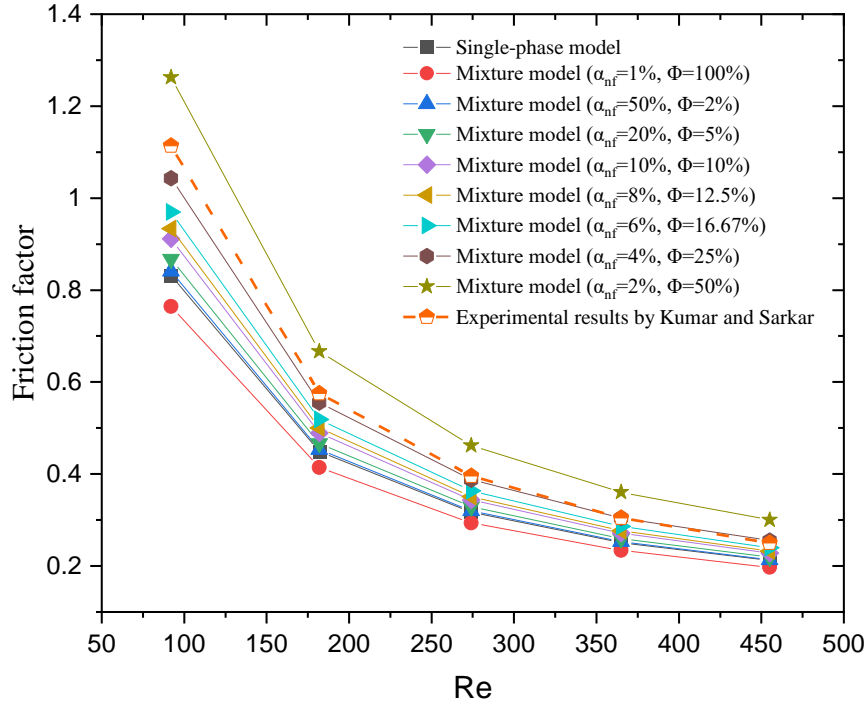
Figure 6.9 Friction factor along minchannel predicted by the single-phase approach and by the two-phase mixture model at $92 \leq Re \leq 455$.

6.3.3 Effect of the diameters size of the second phase nanofluid bubbles on thermal and hydraulic characteristics

Figure 6.10 presents a parametric study of the minichannel average bottom wall temperature and of its pressure drop using the two-phase mixture model with ($\alpha_{nf} = 20\%, \Phi = 5\%$) and ($\alpha_{nf} = 4\%, \Phi = 25\%$), in which the second phase nanofluid bubble diameter is varied over the range 85 nm $\leq d_{nf} \leq$ 150 nm. The average bottom wall temperature and the pressure drop are shown to be substantially independent from d_{nf} over the range 85 nm to 150 nm. The two-phase mixture model with ($\alpha_{nf} = 4\%, \Phi = 25\%$) did not meet the residuals convergence threshold of 1×10^{-6} when using a second phase nanofluid diameter in the range 137 nm $\leq d_{nf} \leq$ 150 nm. These less converged results are shown in Figure 6.10 by the open symbols. Whilst not meeting the 10^{-6} residuals convergence criterion, these less converged results support the substantial independence of the two-phase mixture model predictions from the second phase bubble diameter d_{nf},

over the range 85 nm $\leq d_{nf} \leq$ 150 nm. All other two-phase mixture model simulations presented in this paper use a fixed value of $d_{nf} = 98$ nm, which is within this range.
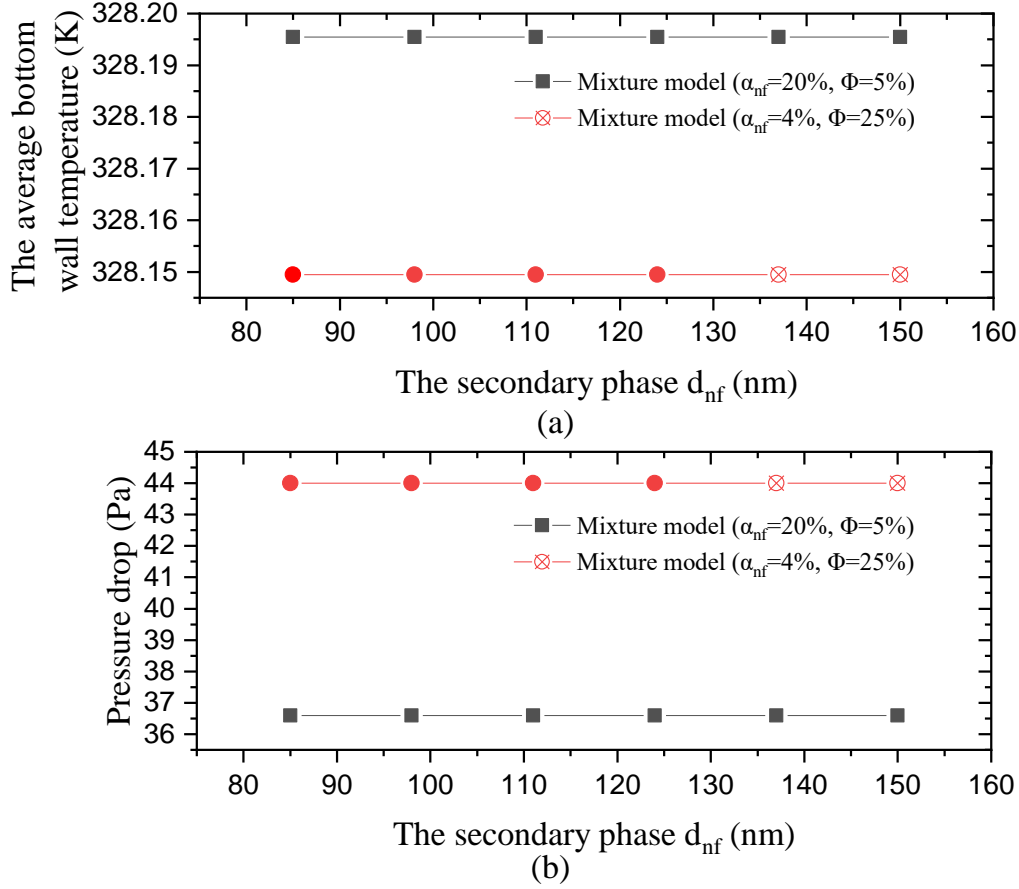
Figure 6.10 Variation of the minichannel (a) average bottom wall temperature and (b) inlet to outlet pressure drop with the phase two bubble diameter d_{nf}, over the range 85nm $\leq d_{nf} \leq$ 150nm. Two-phase mixture model with second phase volume fractions α_{nf} 20% and 4%.

6.3.4 The second law efficiency of the minichannel heat sink

Figure 6.11 displays the exergy destruction rate $\dot{E}_{xd}$ across the minichannel heat sink over the Reynolds number range 92 to 455 at a Al_2O_3 nanoparticle volume fraction $\phi = 1\%$. All models show a reduction in $\dot{E}_{xd}$ with increasing Reynolds number, which is due the reduction in the minichannel bottom surface temperature at increasing Reynolds numbers (Ali et al., 2021a, Ali et al., 2021b). In fact, reducing T decreases $\left(1 - \frac{T_r}{T}\right)$ in the dominant first term of equation (2.30) and hence it lowers $\dot{E}_{xd}$. The exergy inflow transported by the nanofluid is zero, since the dead state temperature T_r is equal to the inlet temperature T_{in}. The minimum exergy destruction rate $\dot{E}_{xd}$ is achieved at the highest Reynolds number, at which the minichannel average bottom surface temperature is lowest, owing to the average heat transfer coefficient being highest, as shown in Figure 6.7. The

$\dot{E}_{xd}$ predictions from the single-phase approach and from the two-phase mixture model with $(\alpha_{nf} \geq 2\%, \Phi \leq 50\%)$ essentially overlap, confirming the good agreement among the models in predicting the minichannel thermal performance reported in Figure 6.7. The two-phase mixture model with $(\alpha_{nf} = 1\%, \Phi = 100\%)$ produces predictions discordant with this data collapse. This indicates that the two-phase mixture model is improperly applied to a second phase made up solely of nanoparticles, as discussed in section 6.3.2. This agrees with the finding in Figure 6.7, where the heat transfer coefficient of the mixture model with $(\alpha_{nf} = 1\%, \Phi = 100\%)$ is reported as being well above that from all other models, as well as above the experimental measurements.
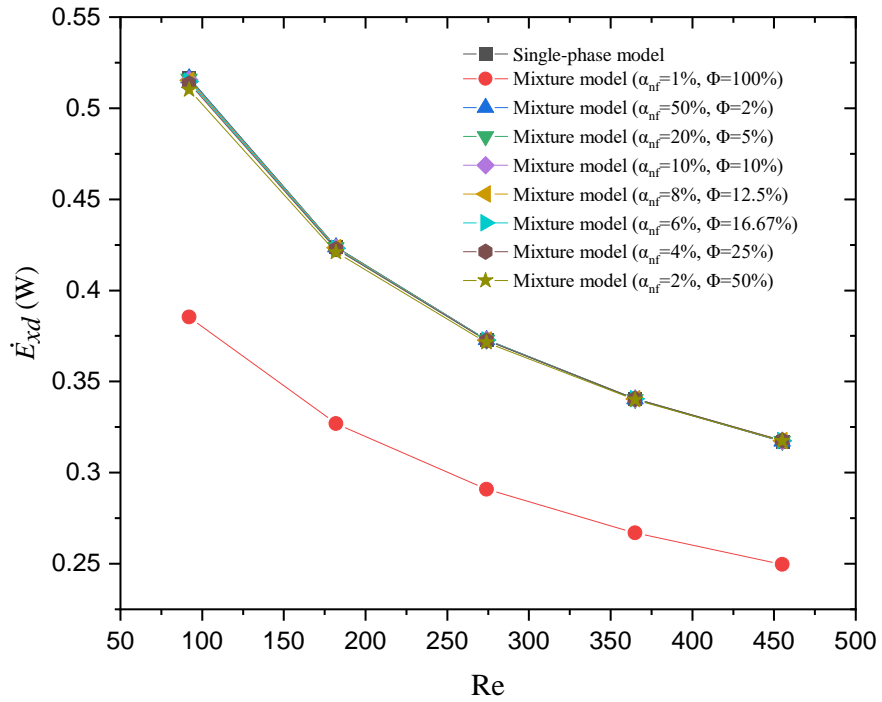
Figure 6.11 Variation of the exergy destruction rate $\dot{E}_{xd}$ in the minchannel with Reynolds number, over the range $92 \leq Re \leq 455$. Predictions from the single-phase approach and from the two-phase mixture model.

Figure 6.12 displays the rate of exergy expended $\dot{E}_x$ in the minichannel heat sink, predicted by the single-phase approach and by the two-phase mixture model, over the Reynolds number range 92 to 455, at a Al_2O_3 nanoparticle volume fraction $\phi = 1\%$. The only contribution of the rate of exergy expended $\dot{E}_x$ is the heat transfer through the heated base, since the dead state reference temperature T_r is equal to the inlet temperature T so that $\psi = 0$ across the inlet. Figure 6.12 shows the same decreasing trend in $\dot{E}_x$ with increasing Reynolds number as for $\dot{E}_{xd}$ in Figure 6.11. There is good agreement among the predictions from the single-phase approach and from the two-phase mixture model

with $(\alpha_{nf} \geq 2\%, \Phi \leq 50\%)$, which indicate that the lowest rate of exergy expended occurs at the highest Reynolds number. The two-phase mixture model with $(\alpha_{nf} = 1\%, \Phi = 100\%)$ gives lower exergy destruction rate predictions that are lower than the ones shown in the data collapse with $(\alpha_{nf} \geq 2\%, \Phi \leq 50\%)$. This supports the $(\alpha_{nf} = 1\%, \Phi = 100\%)$ combination not being an appropriate two-phase mixture model setting, as discussed in the context of Figure 6.7.
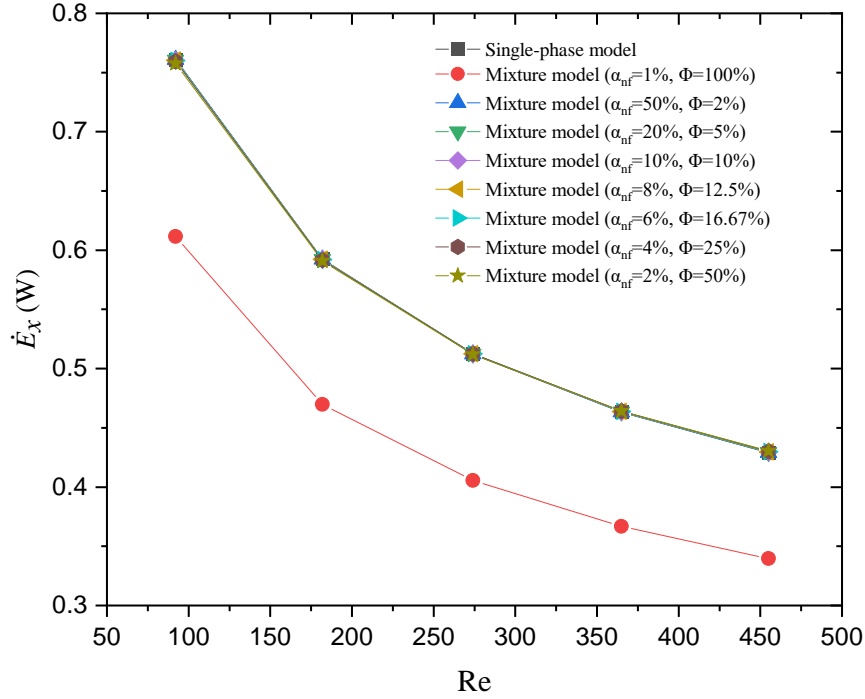
Figure 6.12 Variation of the rate of exergy expended $\dot{E}_x$ in the minchannel with the Reynolds number, over the range $92 \leq Re \leq 455$. Predictions from the single-phase approach and from the two-phase mixture model.

Figure 6.13 shows the second law efficiency η_{II} of the minchannel heat sink, estimated using the single-phase approach and the two-phase mixture model, at Reynolds numbers between 92 and 455, at a Al_2O_3 nanoparticle volume fraction $\phi = 1\%$. The second law efficiency is evaluated by combining $\dot{E}_{xd}$ and $\dot{E}_x$ in equation (2.33).

The main trend is a decrement in the second law efficiency with increasing Reynolds number. This trend differs from that reported in Ali et al. (2021a) for the flow through a rectangular microchannel at similar Reynolds numbers, which displayed a minimum and involved higher numerical values of second law efficiency. The cause of this trend change is unclear. One possible explanation is that the length scale difference between minichannels and microchannels causes a difference in the heat conduction

resistance across the thicker minichannel walls. This may cause the second law efficiency minimum to occur at a higher Reynolds number in a minichannel than in a microchannel.

The two-phase mixture model with $(\alpha_{nf} = 1\%, \Phi = 100\%)$ predicts a second law efficiency 15.15% higher than that from the single-phase approach at $Re = 93$ and 1.79% higher at $Re = 455$. Using $(\alpha_{nf} \geq 2\%, \Phi \leq 50\%)$ this discrepancy reduces to a maximum of 0.0314% and of 0.0115% at Reynolds numbers 92 and 455, respectively. This reaffirms the $(\alpha_{nf} = 1\%, \Phi = 100\%)$ combination not being an appropriate two-phase model setting.

Upon close inspection, Figure 6.13 shows that that two-phase mixture model predictions with $(\alpha_{nf} = 2\%, \Phi = 50\%)$ are second farthest from the single-phase approach prediction and that the two-phase mixture model η_{II} predictions display a monotonic and progressive approach to η_{II} predicted by the single-phase approach, with increasing α_{nf}. This behaviour is mainly driven by the flow exergy term in the definition of $\dot{E}_x$ and $\dot{E}_{xd}$, which includes the exergy change due to friction over the channel walls, which is reflected in the inlet to outlet pressure drop in Figure 6.8. As the contribution from the flow exergy term is relatively small compared to that generated by the heat flux through the minichannel base, its effect on η_{II} is minor, as shown in Figure 6.13.
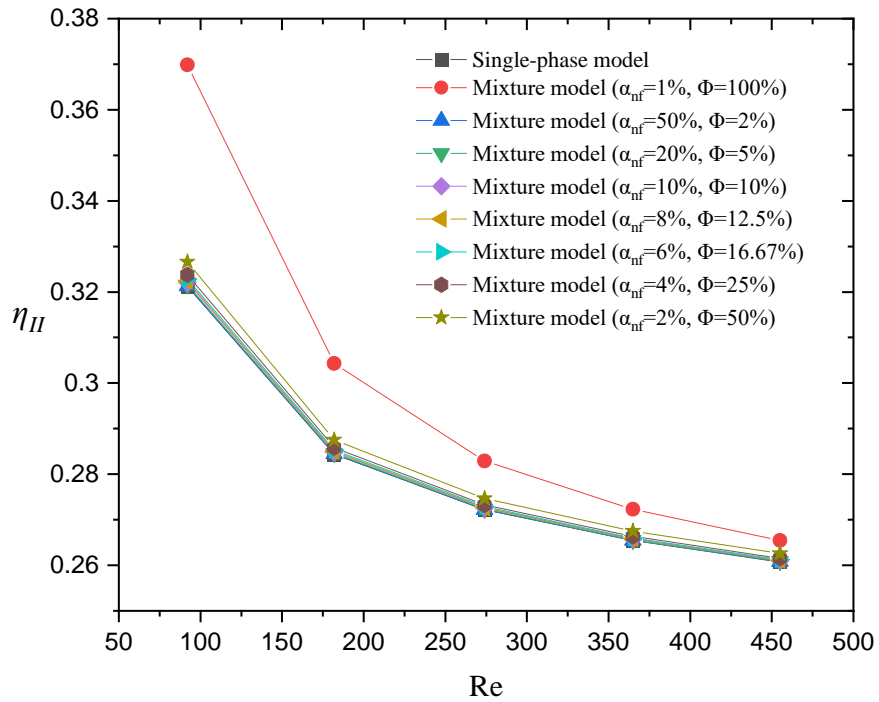
Figure 6.13 Variation of the minichannel second law efficiency η_{II} over the Reynolds number range 92 to 455. Predictions using the single-phase approach and the two-phase mixture model.

6.3.5 Thermal and hydraulic characteristics on a horizontal microscale backward-facing step

Figure 6.14 shows the velocity profile across the horizontal microscale backwards-facing step at the streamwise location where the channel undergoes the sudden enlargement, that is, at the step edge. These numerical predictions are obtained with the single-phase approach and with the two-phase mixture model. Different combinations of phase two volume fraction and of phase two Al_2O_3 nanoparticle volume fraction, as defined in Table 2.2, provide the same 1% Al_2O_3 nanoparticle volume fraction in the mixture. The results are compared to corresponding numerical predictions by Klazly and Bognar (2022) at the Reynolds number of 280.

The length to height ratio $L_u/h_u = 250$ is much greater than the entry length to height ratio of 3.41 of a laminar channel flow (Joshi and Vinoth, 2018). This establishes a fully developed laminar channel flow, with its characteristic parabolic velocity profile in x_2. The simulation is two-dimensional and therefore the flow is uniform spanwise. The predictions from all the combinations of phase two volume fraction in Table 2.2 as well as from the single-phase approach collapes on essentially a single, parabolic-shaped curve. The velocity profile is substantially symmetric about $x_2 = 0$, suggesting the absence of any significant flow stratification effect, due to the relatively small difference in density between the first and the second phases in the two-phase mixture model. The numerical results from Klazly and Bognar (2022) follow the same trend and their scatter about the parabolic-shaped data collapse from the current models is driven by the digitization process of the reference data from the article print.
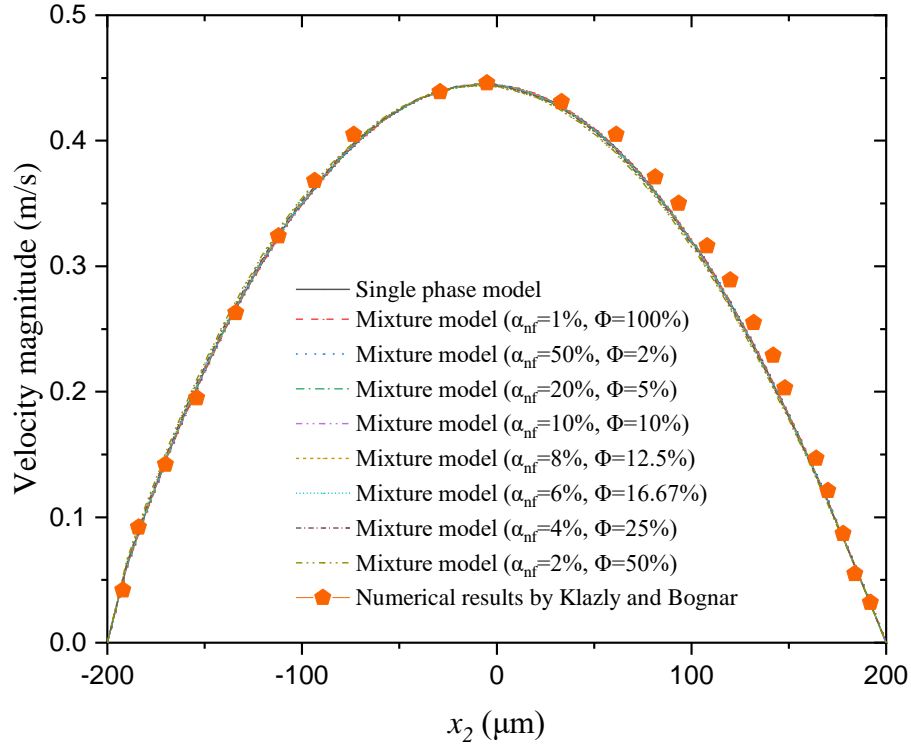
Figure 6.14 Velocity profile above the backwards facing step, at the location of the channel sudden enlargement.

As shown by the flow visualisations in Klazly and Bognar (2022), the flow separates at the backwards facing step edge, creating a laminar shear layer that reattaches on the floor, about six step heights downstream. The streamline connecting the separation point and the reattachment point defines a clockwise flow recirculation region, which is relatively segregated from the inlet cold coolant feed running over the top of the step. This creates a region of elevated temperature, in which the more modest wall-normal thermal gradient as well as the more modest convective heat transport away from the wall produces low local values of Nusselt number.

This effect is shown in Figure 6.15, where the predictions of the local Nusselt number are plotted along the heated bottom wall. The results are compared to the experiments by Kherbeet et al. (2014) and to numerical results by Klazly and Bognar (2022) at the same Reynolds number of 280 as in Figure 6.14. Just downstream of the backwards facing step face, which is located at $x_1 = 0.1$ m, the local value of the Nusselt number is relatively low and it increases in x_1 over the range from 0.1 m to 0.104 m. Just downstream of the reattachment pont, the cold flow from the top of the step meets the heated wall, creating both a strong wall-normal thermal gradient and the means for transporting heat away from the wall, by the increase in coolant specific internal energy.

128

This produes the observed local heat transfer maximum. Further downstream, the temperature increment of the coolant due to the heat that it has picked up reduces its temperature difference with the wall and therefore its ability to extract further heat. This produces a monotonic decay in the local Nusselt number all the way to the exit of the duct. Figure 6.15 hows good agreement between the single phase model and the mixture models with a second phase volume fraction greater or equal to 2%. These predictions are consistent with the reference measurements reported in Kherbeet et al. (2014). The mixture model prediction with a second phase volume fraction of 1%, that is, where the second phase is entirely made up of nanoparticles, over-predicts the local Nusselt number and is a clear outlier. Like with the rectangular minichannel, the microscale backwards facing step is inappropriately modelled by the two-phase mixture model in which the second phase is not a fluid.
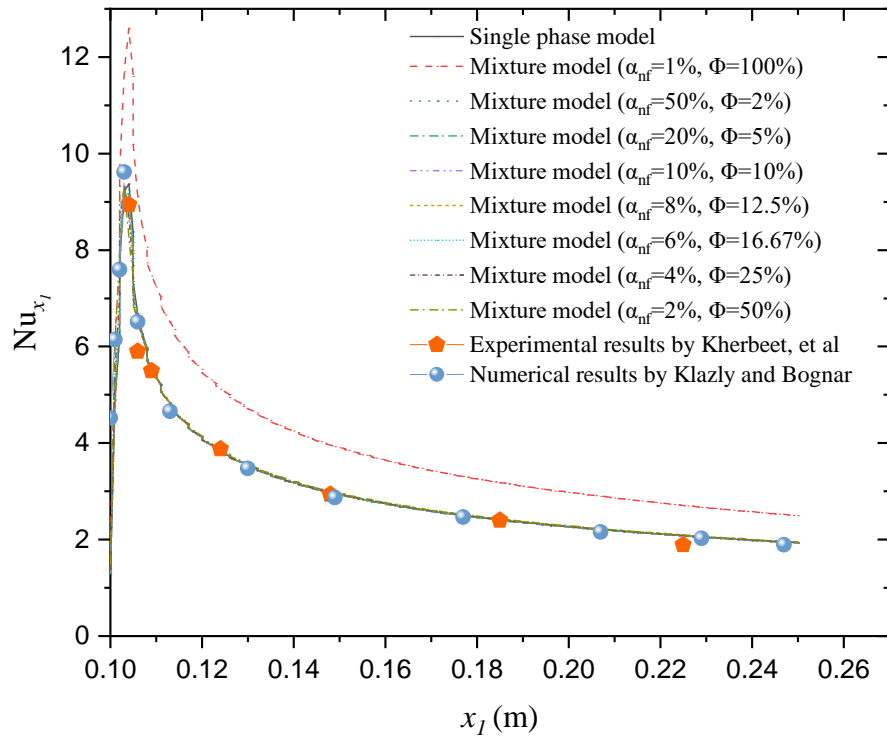
Figure 6.15 Local Nusselt number along the heated bottom wall of a microscale backward-facing step at $Re = 280$.

6.4 Conclusions

This work has identified, assessed, and solved the root cause of the research community's lack of confidence in two-phase mixture models for predicting the performance of a nanofluid cooled minichannel heat sink, compared to the more widely adopted and simpler single-phase approach.

It has done so by implementing both single-phase and two-phase mixture models for the forced convection in a minichannel heat sink of rectangular cross-section, cooled by water and Al_2O_3 nanoparticles, at a nanoparticle volume fraction of ϕ =1%, in the Reynolds number range 92 to 455. The key to a successful two-phase mixture model implementation is using water as one phase and, for the second phase, a Newtonian fluid of equivalent thermal and physical properties of a suspension of nanoparticles in water. The second phase nanoparticle volume fraction must be less than 100% to provide a physical fluid, rather than a solid, for the second phase. The same conclusion is arrived at by modelling the flow and heat transport through a microscale backwards facing step, with a uniformly heated bottom wall. The flow separation and recirculation near the step shows that, in the presence of greater flow complexity, the two-phase mixture model with a 100% phase two volume fraction of nanoparticles is still at variance with the other models. Specifically, it over-predicts the local Nusselt number peak by 35%.

Various combinations of second phase volume fraction α_{nf} and second phase nanoparticle volume fraction Φ were used in the two-phase mixture model to represent the same 1% Al_2O_3 nanoparticle water mixture. For all thermal and flow performance quantities considered, increasing the second phase volume fraction above 2% in the minichannel heat sink provided a monotonic and incremental approach to the predictions from the single-phase model. This clearly shows that the two-phase mixture model converges towards the single-phase predictions for a homogeneous nanofluid.

The minichannel mean heat transfer coefficient predictions and, to a good extent, the rates of exergy expended and destroyed, as well as the second law efficiency, were found to be relatively insensitive to the second phase volume fraction, within the range α_{nf} for which the model remains physically sound. The agreement with experiment in the mean heat transfer coefficient was within 2.5% and 1.76% at Re = 455 with the single-phase approach and with the two-phase mixture model $(\alpha_{nf} \geq 2\%, \Phi \geq 50\%)$, respectively. On the other hand, the minichannel friction factor and pressure drop display

variations with appreciable α_{nf} dependence. The agreement with experiment varies from -2% at $\alpha_{nf} = 4\%$ to 14.7% at $\alpha_{nf} = 50\%$. The latter is similar to the 15.4% agreement with experiment that is obtained using the single-phase approach.

These results, albeit limited in applicability by the minichannel simple geometry used in this study, have important practical implications for the progress of heat sink technology. It is shown that in the rectangular minichannel at the tested flow conditions, the lack of significant flow curvature to drive phase segregation develops a condition close to that of a homogeneous mixture. This is evidenced by the average heat transfer coefficient predicted by the two-phase mixture model being substantially invariant over a range of α_{nf} and Φ combinations. This provides an important performance feature to rectangular minichannel heat sinks required to work within tight temperature tolerances. As the current model resolves neither sedimentation nor agglomeration nor other direct particle-particle interaction, the lack of uniformity in the nanofluid due to these processes was not modelled. Therefore, heat sinks featuring such phenomena may well not have this performance feature.

Furthermore, this work shows that a well-dispersed, homogeneous nanofluid suspension provides the best choice for minimising the channel pressure loss and therefore the expended pumping power.

Finally, this paper has provided the protocol for using the two-phase mixture model within appropriate volume fraction bounds. This higher fidelity method, unconstrained by the uniform particle distribution assumption of the single-phase approach, can now be used with confidence to explore more complex minichannel geometries and resolve localised concentrations of nanoparticles, exploring their effect on the thermal and mass transport characteristics.

Chapter 7: Conclusions and directions for further work

7.1 Conclusions

Microchannel heat sinks have the ability to dissipate heat well, provide a nearly uniform heated wall temperature distribution and can have a low power consumption. This potential is not achieved in typical microchannel heat sinks with a parallel and straight layout, which can feature high power consumption, a large temperature gradient, and poor heated wall temperature uniformity. Therefore, the hydrothermal performance of conventional microchannel heat sinks was improved. It was possible to achieve this by shape and structural optimisations of the microchannel. Moreover, among other technologies, novel coolants with improved thermo-physical properties, which are referred to as nanofluids, were explored. Therefore, this work has provided an important contribution to disseminating advances to the state of the art in heat transfer and fluid mechanics, for applications of significant economic impact.

More specifically, this work investigated the optimum geometry and coolant composition in various microchannel heat sinks to enhance cooling using ANSYS FLUENT 19.5. This work used the conjugate heat transfer through both the fluid and solid zones of different microchannel heat sinks. Several twisted tapes and fins were carefully designed and inserted in the virtual microchannels to produce a range of channel geometries and, at the same time, produce significant changes in the through flow pattern.

Previous research documented the use of twisted tapes in large channels to improve the overall thermal performance by changing axial flow into swirl flow. Thus, twisted tapes were used in the current research to undertake additional studies on the thermo-hydraulic effects of inserting a single straight tape and a twisted tape in a circular microchannel heat sink under a constant heat flux of 100 W/m^2 running either water or nanofluid coolant. The coupled heat transfer through the silicon walls and the coolant, modelled as a single-phase fluid, was examined over the Reynolds number range $100 \leq Re \leq 350$. The microchannel heat sink with swirl flow and with the highest nanoparticle volume fraction concentration provided an average bottom wall temperature 10.5 K below that of the equivalent circular microchannel without tape running pure water at the same Reynolds number, but it generated a higher flow resistance than the micro-channel with no tape cooled by pure water. Using a straight tape also lowered the average bottom wall temperature by 3.35 K below that of the equivalent circular microchannel without a tape,

but to a less extent than with a twisted tape. This provided evidence of two processes concurring to the performance of the tape, which are heat conduction along the tape, which assists with heating the cold coolant inflow near the inlet, and enhanced heat convection by the coolant flow rotating about the microchannel axis, that adds an azimuthal velocity component and provides higher velocity magnitude on approach to the wall. Twisted tapes had a positive trade-off between the gains in cooling performance and in flow resistance. This makes these configurations attractive for designing more performing heat sinks for temperature limited or temperature sensitive micro-electronics.

Further numerical research on hydro-thermal performance-enhancing tape inserts was completed on microchannels featuring (i) radial gaps between the tape and the tube, (ii) tape twist with axial pitch distances of 0, L/2, or L/4, (iii) zero, one, or two 90-degree angular steps between consecutive tape segments, (iv) alternating clockwise and anti-clockwise consecutive twisted tape segments, and combinations of these features. The thermo-hydraulic performance of water-cooled LxL square-base silicon microchannel heat sinks was investigated over the Reynolds number range 100 to 500. Water at a constant inlet temperature of 298 K was modelled. Closing the radial gap between the tape and the cylindrical wall provided a better thermal and hydraulic performance of the heat sink. This gain comes from the heat conduction between the tape and the heat sink cylindrical inner wall. The absence of any tape radial gap also marginally increased the tape heat transfer surface area. Moreover, the alternating tape twist direction of feature (iv) provided the lowest bottom wall average temperature, 16.13 K below that with no tape, at the same Reynolds number of 500. This benefit comes from the tape segments with alternating directions that tend to produce flow separation over the leading edge of the downstream helix. This separation is seen to divert cooler flow running near the axis of the microchannel towards the heated cylindrical microchannel walls. This pitch reversal also radially pushes the streamlines from the axis of the microchannel towards the near-wall region more than by using only clockwise twisted tape segments. The process results in a more uniform coolant temperature. This predicted temperature drop is a significant enhancement to conditioning electronic components so they may be longer-lasting, use less energy, and have a reduced environmental impact.

The performance of microchannel heat sinks with non-circular cross-sections, primarily rectangular microchannel heat sinks, has been studied extensively, owing to the larger wetted area of a non-circular channel compared to that of a tube of the same cross-

section. For this reason, the hydraulic and thermal performance of rectangular microchannel heat sink configurations for high-performance electronic cooling applications was investigated by numerical modelling. Rectangular, twisted, and zig-zag fins were inserted into the plain rectangular duct to enhance the heat transfer rate. Water or nanofluid coolant supplied at 298 K, over the Reynolds number range 100 to 350 was investigated. The zig-zag fin and 3% Al_2O_3 nanofluid provided the highest thermal performance, with a 12.6 K lower average heated wall contact temperature than without the fin running pure water at the Reynolds number of 350. This enhancement is because of an increase in the microchannel internal surface area and a higher secondary flow, which helps the fluid exchange and therefore the heat transport between the warmer peripheral regions near the walls and the cooler centre of the microchannel. Twist in the microchannel fin decreased the microchannel pressure drop by 2% to 15% compared to a straight fin, possibly due to the more evenly distributed axial mass flux across the microchannel. Inserting the rectangular fin increased the wetted wall area, which produced a lower bottom wall average temperature, 6.44 K lower than without a fin. The main mechanism responsible for the enhancement is the increase in the microchannel internal surface area, leading to a lower temperature difference between the flow and the walls.

Various authors documented over-estimations of the heat transfer with the two-phase mixture model approach in contrast to the single-phase approach. Therefore, a further research was carried out to investigate, address, and solve this key shortcoming. This enabled reliable physically sound predictions of minichannel nanoflows, using the two-phase mixture model. This was achieved by applying the single-phase and the two-phase mixture model to a rectangular minichannel heat sink, cooled by a 1% volume suspension of Al_2O_3 nanoparticles in water, over the Reynolds number range 92 to 455. In the two-phase mixture model, the volume fraction α_{nf} of the second phase was varied between 2% and 50%. The second phase α_{nf} must be lower than 100% to provide a physical fluid rather than a solid. A two-phase mixture with a solid second phase ($\alpha_{nf} = 1\%, \Phi = 100\%$) broke the Newtonian fluid assumption within the model and made outlier predictions. The two-phase mixture with fluid second phase ($\alpha_{nf} \geq 2\%, \Phi \leq 50\%$) converged instead towards the single-phase thermal predictions. The minichannel friction factor exhibited appreciable variations with the second phase volume fraction α_{nf}. This has opened the way for using the two-phase mixture model with confidence to assess

and resolve uneven nanoparticle dispersion effects and increase the thermal and mass transport performance of minichannels.

7.2 Recommended future work

Heat transfer enhancement in microscale channels is one of the most highly investigated topics because of its wide applications. According to the literature review presented in chapter 1, various researchers have progressively improved the configuration of the geometry and of the coolant in various microchannel heat sinks to enhance cooling. This study extended the state of the art and the knowledge base to novel configurations, using innovative geometries in combination with nanofluids. Based on the outcomes of this study, the following recommendation are made for future work in this field:

- The present research should be followed by experimental work to validate the numerical predictions of the novel configurations.
- The study could be extended to develop an empirical correlation, or scaling law, to predict heat transfer enhancement of the nanofluid swirl flow.
- High pressure drop is a main limitation for the microchannel heat sinks, therefore future efforts could usefully focus towards developing heat sinks with a low pressure drop.
- The type of nanoparticles in the selected geometries could be extended using other materials (CuO, TiO_2 or SiO_2) and other working fluids (ethylene glycol or engine oil).
- The study could be extended to study the impact of the nanoparticles on certain flow regions experiencing some recirculation caused by the twisted tapes or fins. A specific interest is finding whether particle agglomeration or non-uniform particle concentration occurs and to what extent this impacts the overall heat transfer performance.
- Optimisation algorithms and neural networks could be used for evolving the design of microchannel configurations for specific applications.
- Phase change materials (PCMs) could be used to improve the thermal performance in the microchannel heat sink, since the temperature uniformity in conventional heat sinks is relatively poor.

- Thermoelectric cooling in heat sinks, using the Peltier effect, could be used in combination with one of the new configurations studied in this work, to provide additional cooling performance in microchannel heat sinks.

References

Abbassi, H. 2007. Entropy generation analysis in a uniformly heated microchannel heat sink. *Energy,* 32**,** 1932-1947.

Abbassi, H. & Aghanajafi, C. 2006. Evaluation of heat transfer augmentation in a nanofluid-cooled microchannel heat sink. *Journal of Fusion Energy,* 25**,** 187-196.

Abolarin, S. M., Everts, M. & Meyer, J. P. 2019. Heat transfer and pressure drop characteristics of alternating clockwise and counter clockwise twisted tape inserts in the transitional flow regime. *International Journal of Heat and Mass Transfer,* 133**,** 203-217.

Adham, A. M., Mohd-Ghazali, N. & Ahmad, R. 2012. Optimization of an ammonia-cooled rectangular microchannel heat sink using multi-objective non-dominated sorting genetic algorithm (NSGA2). *Heat and Mass Transfer,* 48**,** 1723-1733.

Adham, A. M., Mohd-Ghazali, N. & Ahmad, R. 2013. Thermal and hydrodynamic analysis of microchannel heat sinks: A review. *Renewable and Sustainable Energy Reviews,* 21**,** 614-622.

Ahmed, H. E., Kherbeet, A. S., Ahmed, M. I. & Salman, B. H. 2018. Heat transfer enhancement of micro-scale backward-facing step channel by using turbulators. *International Journal of Heat and Mass Transfer,* 126**,** 963-973.

Akbari, M., Galanis, N. & Behzadmehr, A. 2011. Comparative analysis of single and two-phase models for CFD studies of nanofluid heat transfer. *International Journal of Thermal Sciences,* 50**,** 1343-1354.

Akbari, M., Galanis, N. & Behzadmehr, A. 2012. Comparative assessment of single and two-phase models for numerical studies of nanofluid turbulent forced convection. *International Journal of Heat and Fluid Flow,* 37**,** 136-146.

Akbari, O. A., Afrouzi, H. H., Marzban, A., Toghraie, D., Malekzade, H. & Arabpour, A. 2017. Investigation of volume fraction of nanoparticles effect and aspect ratio of the twisted tape in the tube. *Journal of Thermal Analysis and Calorimetry,* 129**,** 1911-1922.

Akbari, O. A., Toghraie, D. & Karimipour, A. 2016. Numerical simulation of heat transfer and turbulent flow of water nanofluids copper oxide in rectangular microchannel with semi-attached rib. *Advances in Mechanical Engineering,* 8**,** 1-25.

Akbarinia, A. & Laur, R. 2009. Investigating the diameter of solid particles effects on a laminar nanofluid flow in a curved tube using a two phase approach. *International Journal of Heat and Fluid Flow,* 30**,** 706-714.

Al-Rashed, M. H., Dzido, G., Korpyś, M., Smołka, J. & Wójcik, J. 2016. Investigation on the CPU nanofluid cooling. *Microelectronics Reliability,* 63**,** 159-165.

Alam, T. & Kim, M.-H. 2018. A comprehensive review on single phase heat transfer enhancement techniques in heat exchanger applications. *Renewable and Sustainable Energy Reviews,* 81**,** 813-839.

Alfaryjat, A., Miron, L., Pop, H., Apostol, V., Stefanescu, M.-F. & Dobrovicescu, A. 2019. Experimental Investigation of Thermal and Pressure Performance in Computer Cooling Systems Using Different Types of Nanofluids. 9**,** 1231.

Alfaryjat, A., Mohammed, H., Adam, N. M., Ariffin, M. & Najafabadi, M. 2014. Influence of geometrical parameters of hexagonal, circular, and rhombus microchannel heat sinks on the thermohydraulic characteristics. *International Communications in Heat and Mass Transfer,* 52**,** 121-131.

Ali, A. M., Angelino, M. & Rona, A. 2021a. Numerical analysis on the thermal performance of microchannel heat sinks with Al_2O_3 nanofluid and various fins. *Applied Thermal Engineering,* 198**,** 117458.

Ali, A. M., Rona, A., Kadhim, H. T., Angelino, M. & Gao, S. 2021b. Thermo-hydraulic performance of a circular microchannel heat sink using swirl flow and nanofluid. *Applied Thermal Engineering,* 191.

Alipour, H., Karimipour, A., Safaei, M. R., Semiromi, D. T. & Akbari, O. A. 2017. Influence of T-semi attached rib on turbulent flow and heat transfer parameters of a silver-water nanofluid with different volume fractions in a three-dimensional trapezoidal microchannel. *Physica E: Low-Dimensional Systems and Nanostructures,* 88**,** 60-76.

137

Ambreen, T. & Kim, M.-H. 2017. Comparative assessment of numerical models for nanofluids' laminar forced convection in micro and mini channels. *International Journal of Heat and Mass Transfer,* 115**,** 513-523.

Ambreen, T. & Kim, M.-H. 2018a. Effect of fin shape on the thermal performance of nanofluid-cooled micro pin-fin heat sinks. *International Journal of Heat and Mass Transfer,* 126**,** 245-256.

Ambreen, T. & Kim, M.-H. 2018b. Effects of variable particle sizes on hydrothermal characteristics of nanofluids in a microchannel. *International Journal of Heat and Mass Transfer,* 120**,** 490-498.

Ambreen, T., Saleem, A. & Park, C. W. 2021. Homogeneous and Multiphase Analysis of Nanofluids Containing Nonspherical MWCNT and GNP Nanoparticles Considering the Influence of Interfacial Layering. *Nanomaterials,* 11**,** 277.

Angelino, M., Goldstein, R. J. & Gori, F. 2019. Lateral edge effects on heat/mass transfer on a finite width surface within a turbulent boundary layer. *International Journal of Heat and Mass Transfer,* 138**,** 32-40.

ANSYS 2017. 18.0 ANSYS Fluent theory guide 18.0.

ANSYS 2018. ANSYS Fluent tutorial guide 18.

Arani, A. A. A., Akbari, O. A., Safaei, M. R., Marzban, A., Alrashed, A. A., Ahmadi, G. R. & Nguyen, T. K. 2017. Heat transfer improvement of water/single-wall carbon nanotubes (SWCNT) nanofluid in a novel design of a truncated double-layered microchannel heat sink. *International Journal of Heat and Mass Transfer,* 113**,** 780-795.

Ashrafmansouri, S.-S. & Nasr Esfahany, M. 2014. Mass transfer in nanofluids: A review. *International Journal of Thermal Sciences,* 82**,** 84-99.

Awais, M. & Bhuiyan, A. A. 2018. Heat transfer enhancement using different types of vortex generators (VGs): A review on experimental and numerical activities. *Thermal Science and Engineering Progress,* 5**,** 524-545.

Bahiraei, M. 2016. Particle migration in nanofluids: A critical review. *International Journal of Thermal Sciences,* 109**,** 90-113.

Bahiraei, M. & Heshmatian, S. 2017. Efficacy of a novel liquid block working with a nanofluid containing graphene nanoplatelets decorated with silver nanoparticles compared with conventional CPU coolers. *Applied Thermal Engineering,* 127**,** 1233-1245.

Bahiraei, M., Heshmatian, S. & Keshavarzi, M. 2019a. A decision-making based method to optimize energy efficiency of ecofriendly nanofluid flow inside a new heat sink enhanced with flow distributor. *Powder Technology,* 342**,** 85-98.

Bahiraei, M., Jamshidmofid, M. & Goodarzi, M. 2019b. Efficacy of a hybrid nanofluid in a new microchannel heat sink equipped with both secondary channels and ribs. *Journal of Molecular Liquids,* 273**,** 88-98.

Bahiraei, M. & Mazaheri, N. 2021. A comprehensive analysis for second law attributes of spiral heat exchanger operating with nanofluid using two-phase mixture model: Exergy destruction minimization attitude. *Advanced Powder Technology,* 32**,** 211-224.

Bahiraei, M., Mazaheri, N. & Hassanzamani, S. M. 2019c. Efficacy of a new graphene–platinum nanofluid in tubes fitted with single and twin twisted tapes regarding counter and co-swirling flows for efficient use of energy. *International Journal of Mechanical Sciences,* 150**,** 290-303.

Bahiraei, M., Rahmani, R., Yaghoobi, A., Khodabandeh, E., Mashayekhi, R. & Amani, M. 2018. Recent research contributions concerning use of nanofluids in heat exchangers: a critical review. *Applied Thermal Engineering,* 133**,** 137-159.

Balaji, C., Hölling, M. & Herwig, H. 2007. Entropy generation minimization in turbulent mixed convection flows. *International Communications in Heat and Mass Transfer,* 34**,** 544-552.

Barba, A., Musi, B. & Spiga, M. 2006. Performance of a polymeric heat sink with circular microchannels. *Applied Thermal Engineering,* 26**,** 787-794.

Bazdidi-Tehrani, F., Khanmohamadi, S. M. & Vasefi, S. I. 2020. Evaluation of turbulent forced convection of non-Newtonian aqueous solution of CMC/CuO nanofluid in a tube with twisted tape inserts. *Advanced Powder Technology,* 31**,** 1100-1113.

138

Bejan, A. 1982. *Entropy generation through heat and fluid flow*, Wiley, New York.

Bejan, A. 1996. Entropy generation minimization: The new thermodynamics of finite-size devices and finite-time processes. *Journal of Applied Physics,* 79**,** 1191-1218.

Bejan, A. 2013. *Entropy generation minimization: The method of thermodynamic optimization of finite-size systems and finite-time processes*, CRC Press.

Bhandari, P. & Prajapati, Y. K. 2021. Thermal performance of open microchannel heat sink with variable pin fin height. *International Journal of Thermal Sciences,* 159**,** 106609.

Bhattacharya, P., Samanta, A. & Chakraborty, S. 2009. Numerical study of conjugate heat transfer in rectangular microchannel heat sink with Al_2O_3/H_2O nanofluid. *Heat and Mass Transfer,* 45**,** 1323-1333.

Bhuiya, M. M. K., Chowdhury, M. S. U., Saha, M. & Islam, M. T. 2013. Heat transfer and friction factor characteristics in turbulent flow through a tube fitted with perforated twisted tape inserts. *International Communications in Heat and Mass Transfer,* 46**,** 49-57.

Bianco, V., Chiacchio, F., Manca, O. & Nardini, S. 2009. Numerical investigation of nanofluids forced convection in circular tubes. *Applied Thermal Engineering,* 29**,** 3632-3642.

Buongiorno, J. 2005. Convective Transport in Nanofluids. *Journal of Heat Transfer,* 128**,** 240-250.

Cengel, Y. 2010a. Fluid Mechanics: Tata.

Cengel, Y. A. 2010b. *Fluid mechanics*, Tata McGraw-Hill Education.

Chai, L., Wang, L. & Bai, X. 2018. Thermohydraulic performance of microchannel heat sinks with triangular ribs on sidewalls – Part 1: Local fluid flow and heat transfer characteristics. *International Journal of Heat and Mass Transfer,* 127**,** 1124-1137.

Chai, L., Wang, L. & Bai, X. 2019. Thermohydraulic performance of microchannel heat sinks with triangular ribs on sidewalls – Part 2: Average fluid flow and heat transfer characteristics. *International Journal of Heat and Mass Transfer,* 128**,** 634-648.

Chai, L., Xia, G. D. & Wang, H. S. 2016. Laminar flow and heat transfer characteristics of interrupted microchannel heat sink with ribs in the transverse microchambers. *International Journal of Thermal Sciences,* 110**,** 1-11.

Chein, R. & Chuang, J. 2007. Experimental microchannel heat sink performance studies using nanofluids. *International Journal of Thermal Sciences,* 46**,** 57-66.

Chen, K. 2005. Second-law analysis and optimization of microchannel flows subjected to different thermal boundary conditions. *International Journal of Energy Research,* 29**,** 249-263.

Chen, Y. & Cheng, P. 2005. An experimental investigation on the thermal efficiency of fractal tree-like microchannel nets. *International Communications in Heat and Mass Transfer,* 32**,** 931-938.

Cheng, Y. 2007. Numerical simulation of stacked microchannel heat sink with mixing-enhanced passive structure. *International Communications in Heat and Mass Transfer,* 34**,** 295-303.

Choi, S. U. & Eastman, J. A. 1995. Enhancing thermal conductivity of fluids with nanoparticles. Argonne National Lab., IL (United States).

Choquette, S. F., Faghri, M., Charmchi, M. & Asako, Y. 1996. Optimum design of microchannel heat sinks. *American Society of Mechanical Engineers, Dynamic Systems Control Division DSC,* 59**,** 115.

Dai, Z., Zheng, Z., Fletcher, D. F. & Haynes, B. S. 2015. Experimental study of transient behaviour of laminar flow in zigzag semi-circular microchannels. *Experimental Thermal and Fluid Science,* 68**,** 644-651.

Deng, D., Wan, W., Tang, Y., Shao, H. & Huang, Y. 2015. Experimental and numerical study of thermal enhancement in reentrant copper microchannels. *International Journal of Heat and Mass Transfer,* 91**,** 656-670.

Deng, D., Zeng, L. & Sun, W. 2021. A review on flow boiling enhancement and fabrication of enhanced microchannels of microchannel heat sinks. *International Journal of Heat and Mass Transfer,* 175**,** 121332.

Duan, Z., Xie, G., Shen, H. & Wang, C. C. 2021. Thermal performance and entropy generation of single-layer and double-layer constructal Y-shaped bionic microchannel heat sinks. 45**,** 9449-9462.

Eastman, J. A., Phillpot, S., Choi, S. & Keblinski, P. 2004. Thermal transport in nanofluids. *Annual Review of Materials Research,* 34**,** 219-246.

Eiamsa-ard, S. 2010. Study on thermal and fluid flow characteristics in turbulent channel flows with multiple twisted tape vortex generators. *International Communications in Heat and Mass Transfer,* 37**,** 644-651.

Eiamsa-Ard, S., Nanan, K., Wongcharee, K., Yongsiri, K. & Thianpong, C. 2015. Thermohydraulic Performance of Heat Exchanger Tube Equipped with Single-, Double-, and Triple-Helical Twisted Tapes. *Chemical Engineering Communications,* 202**,** 606-615.

Eiamsa-ard, S. & Promvonge, P. 2010. Performance assessment in a heat exchanger tube with alternate clockwise and counter-clockwise twisted-tape inserts. *International Journal of Heat and Mass Transfer,* 53**,** 1364-1372.

Eiamsa-ard, S., Thianpong, C., Eiamsa-ard, P. & Promvonge, P. 2010. Thermal characteristics in a heat exchanger tube fitted with dual twisted tape elements in tandem. *International Communications in Heat and Mass Transfer,* 37**,** 39-46.

Esmaeilnejad, A., Aminfar, H. & Neistanak, M. S. 2014. Numerical investigation of forced convection heat transfer through microchannels with non-Newtonian nanofluids. *International Journal of Thermal Sciences,* 75**,** 76-86.

Gamrat, G., Favre-Marinet, M. & Asendrych, D. 2005. Conduction and entrance effects on laminar liquid flow and heat transfer in rectangular microchannels. *International Journal of Heat and Mass Transfer,* 48**,** 2943-2954.

Ghani, I. A., Kamaruzaman, N. & Sidik, N. A. C. 2017a. Heat transfer augmentation in a microchannel heat sink with sinusoidal cavities and rectangular ribs. *International Journal of Heat and Mass Transfer,* 108**,** 1969-1981.

Ghani, I. A., Sidik, N. A. C., Mamat, R., Najafi, G., Ken, T. L., Asako, Y. & Japar, W. M. A. A. 2017b. Heat transfer enhancement in microchannel heat sink using hybrid technique of ribs and secondary channels. *International Journal of Heat and Mass Transfer,* 114**,** 640-655.

Ghasemi, S. E., Ranjbar, A. & Hosseini, M. 2017. Numerical study on effect of CuO-water nanofluid on cooling performance of two different cross-sectional heat sinks. *Advanced Powder Technology,* 28**,** 1495-1504.

Giles, M. B. 1997. Stability analysis of numerical interface conditions in fluid–structure thermal analysis. *International journal for numerical methods in fluids,* 25**,** 421-436.

Gunnasegaran, P., Mohammed, H., Shuaib, N. & Saidur, R. 2010. The effect of geometrical parameters on heat transfer characteristics of microchannels heat sink with different shapes. *International Communications in Heat and Mass Transfer,* 37**,** 1078-1086.

Guo, H.-J., Ye, W.-B., Hong, Y., Wu, S.-Y. & Peng, D.-Q. 2018. Entropy-based thermal hydraulic performances for microchannel heat sinks combined with ribs and cavities. *Computational Thermal Sciences: An International Journal,* 10**,** 67-87.

Guo, J., Fan, A., Zhang, X. & Liu, W. 2011. A numerical study on heat transfer and friction factor characteristics of laminar flow in a circular tube fitted with center-cleared twisted tape. *International Journal of Thermal Sciences,* 50**,** 1263-1270.

Haddad, O., Abuzaid, M. & Al-Nimr, M. 2004. Entropy generation due to laminar incompressible forced convection flow through parallel-plates microchannel. *Entropy,* 6**,** 413-426.

Haghshenas Fard, M., Esfahany, M. N. & Talaie, M. R. 2010. Numerical study of convective heat transfer of nanofluids in a circular tube two-phase model versus single-phase model. *International Communications in Heat and Mass Transfer,* 37**,** 91-97.

Halliday, D., Resnick, R. & Walker, J. 2013. *Fundamentals of physics*, John Wiley & Sons.

Harley, J. C., Huang, Y., Bau, H. H. & Zemel, J. N. 1995. Gas flow in micro-channels. *Journal of Fluid Mechanics,* 284**,** 257-274.

Hashemi, S. M. H., Fazeli, S. A., Zirakzadeh, H. & Ashjaee, M. 2012. Study of heat transfer enhancement in a nanofluid-cooled miniature heat sink. *International Communications in Heat and Mass Transfer,* 39**,** 877-884.

He, Y., Liu, L., Li, P. & Ma, L. 2018. Experimental study on heat transfer enhancement characteristics of tube with cross hollow twisted tape inserts. *Applied Thermal Engineering,* 131**,** 743-749.

Hosseinnejad, R., Hosseini, M. & Farhadi, M. 2019. Turbulent heat transfer in tubular heat exchangers with twisted tape. *Journal of Thermal Analysis and Calorimetry,* 135**,** 1863-1869.

Hung, T.-C. & Yan, W.-M. 2012a. Effects of tapered-channel design on thermal performance of microchannel heat sink. *International Communications in Heat and Mass Transfer,* 39**,** 1342-1347.

Hung, T.-C. & Yan, W.-M. 2012b. Enhancement of thermal performance in double-layered microchannel heat sink with nanofluids. *International Journal of Heat and Mass Transfer,* 55**,** 3225-3238.

Hung, T.-C., Yan, W.-M. & Li, W.-P. 2012. Analysis of heat transfer characteristics of double-layered microchannel heat sink. *International Journal of Heat and Mass Transfer,* 55**,** 3090-3099.

Hussien, A. A., Abdullah, M. Z. & Al-Nimr, M. d. A. 2016. Single-phase heat transfer enhancement in micro/minichannels using nanofluids: Theory and applications. *Applied Energy,* 164**,** 733-755.

Ibrahim, M., Saleem, S., Chu, Y.-M., Ullah, M. & Heidarshenas, B. 2021. An investigation of the exergy and first and second laws by two-phase numerical simulation of various nanopowders with different diameter on the performance of zigzag-wall micro-heat sink (ZZW-MHS). *Journal of Thermal Analysis and Calorimetry,* 145**,** 1611-1621.

Irandoost, S. M., Maleki, A., Safdari, S. M. & Tlili, I. 2020. Numerical investigation of forced convective heat transfer and performance evaluation criterion of Al_2O_3/Water nanofluid flow inside an axisymmetric microchannel. *Symmetry,* 12.

Jang, S. P. & Choi, S. U. S. 2006. Cooling performance of a microchannel heat sink with nanofluids. *Applied Thermal Engineering,* 26**,** 2457-2463.

Jing, D. & He, L. 2019. Numerical studies on the hydraulic and thermal performances of microchannels with different cross-sectional shapes. *International Journal of Heat and Mass Transfer,* 143**,** 118604.

Jing, D., Song, J. & Sui, Y. 2020. Hydraulic and thermal performances of laminar flow in fractal treelike branching microchannel network with wall velocity slip. *Fractals,* 28**,** 2050022.

Joshi, Y. & Vinoth, B. R. 2018. Entry Lengths of Laminar Pipe and Channel Flows. *Journal of Fluids Engineering,* 140.

Kakaç, S. & Pramuanjaroenkij, A. 2009. Review of convective heat transfer enhancement with nanofluids. *International Journal of Heat and Mass Transfer,* 52**,** 3187-3196.

Kalteh, M., Abbassi, A., Saffar-Avval, M., Frijns, A., Darhuber, A. & Harting, J. 2012. Experimental and numerical investigation of nanofluid forced convection inside a wide microchannel heat sink. *Applied Thermal Engineering,* 36**,** 260-268.

Kamyar, A., Saidur, R. & Hasanuzzaman, M. 2012. Application of Computational Fluid Dynamics (CFD) for nanofluids. *International Journal of Heat and Mass Transfer,* 55**,** 4104-4115.

Kandlikar, S. G. & Bapat, A. V. 2007. Evaluation of Jet Impingement, Spray and Microchannel Chip Cooling Options for High Heat Flux Removal. *Heat Transfer Engineering,* 28**,** 911-923.

Kandlikar, S. G. & Grande, W. J. 2003. Evolution of microchannel flow passages-thermohydraulic performance and fabrication technology. *Heat Transfer Engineering,* 24**,** 3-17.

Khaleduzzaman, S. S., Sohel, M. R., Mahbubul, I. M., Saidur, R. & Selvaraj, J. 2016. Exergy and entropy generation analysis of TiO_2–water nanofluid flow through the water block as an electronics device. *International Journal of Heat and Mass Transfer,* 101**,** 104-111.

Khan, W. A., Yovanovich, M. M. & Culham, J. R. Optimization of microchannel heat sinks using entropy generation minimization method. Twenty-second annual IEEE semiconductor thermal measurement and management symposium, 14-16 March 2006 2006. 78-86.

Kherbeet, A. S., Mohammed, H. A., Salman, B. H., Ahmed, H. E. & Alawi, O. A. 2014. Experimental and numerical study of nanofluid flow and heat transfer over microscale backward-facing step. *International Journal of Heat and Mass Transfer,* 79**,** 858-867.

Khodabandeh, E., Rozati, S. A., Joshaghani, M., Akbari, O. A., Akbari, S. & Toghraie, D. 2019. Thermal performance improvement in water nanofluid/GNP–SDBS in novel design of double-layer microchannel heat sink with sinusoidal cavities and rectangular ribs. *Journal of Thermal Analysis and Calorimetry,* 136**,** 1333-1345.

Khoshvaght-Aliabadi, M. & Feizabadi, A. 2020. Performance intensification of tubular heat exchangers using compound twisted-tape and twisted-tube. *Chemical Engineering and Processing - Process Intensification,* 148**,** 107799.

Klazly, M. & Bognar, G. 2022. Heat transfer enhancement for nanofluid flows over a microscale backward-facing step. *Alexandria Engineering Journal,* 61**,** 8161-8176.

Kleiner, M. B., Kuhn, S. A. & Haberger, K. 1995. High performance forced air cooling scheme employing microchannel heat exchangers. *IEEE Transactions on Components, Packaging, and Manufacturing Technology: Part A,* 18**,** 795-804.

Koo, J. & Kleinstreuer, C. 2005. Laminar nanofluid flow in microheat-sinks. *International Journal of Heat and Mass Transfer,* 48**,** 2652-2661.

Korasikha, N. R., Sharma, T. K., Rao, G. A. P. & Murthy, K. M. 2021. Recent advancements in thermal performance enhancement in microchannel heatsinks for electronic cooling application. *Heat Transfer-Design, Experimentation and Applications.* IntechOpen.

Korpyś, M., Dzido, G. & Wójcik, J. Experimental and CFD investigation of commercial PC heat sink performance using water and nanofluids. 14th European conference on mixing Warszawa, 2012. 13.

Koşar, A. 2010. Effect of substrate thickness and material on heat transfer in microchannel heat sinks. *International Journal of Thermal Sciences,* 49**,** 635-642.

Kumar, N. & Puranik, B. P. 2017. Numerical study of convective heat transfer with nanofluids in turbulent flow using a Lagrangian-Eulerian approach. *Applied Thermal Engineering,* 111**,** 1674-1681.

Kumar, V. & Sarkar, J. 2019. Numerical and experimental investigations on heat transfer and pressure drop characteristics of Al_2O_3-TiO_2 hybrid nanofluid in minichannel heat sink with different mixture ratio. *Powder Technology,* 345**,** 717-727.

Kurowski, L., Chmiel-Kurowska, K. & Thulliea, J. 2009. Numerical simulation of heat transfer in nanofluids. *In:* Jeżowski, J. & Thullie, J. (eds.) *Computer Aided Chemical Engineering.* Elsevier.

Lakshminarayanan, V. & Sriraam, N. The effect of temperature on the reliability of electronic components. 2014 IEEE International Conference on Electronics, Computing and Communication Technologies (CONECCT), 6-7 Jan. 2014 2014. 1-6.

Li, C., Guo, H.-J., Ye, W.-B., Hong, Y. & Huang, S.-M. 2019. Thermohydraulic characteristics of microchannel heat sinks combined with ribs and cavities: Effects of geometric parameter and heat flux. *Heat Transfer Research,* 50**,** 89-105.

Li, P., Guo, D. & Huang, X. 2020. Heat transfer enhancement, entropy generation and temperature uniformity analyses of shark-skin bionic modified microchannel heat sink. *International Journal of Heat and Mass Transfer,* 146**,** 118846.

Li, Y., Xia, G., Ma, D., Jia, Y. & Wang, J. 2016. Characteristics of laminar flow and heat transfer in microchannel heat sink with triangular cavities and rectangular ribs. *International Journal of Heat and Mass Transfer,* 98**,** 17-28.

Liu, W., Liu, P., Dong, Z. M., Yang, K. & Liu, Z. C. 2019. A study on the multi-field synergy principle of convective heat and mass transfer enhancement. *International Journal of Heat and Mass Transfer,* 134**,** 722-734.

Liu, W., Liu, P., Wang, J. B., Zheng, N. B. & Liu, Z. C. 2018a. Exergy destruction minimization: A principle to convective heat transfer enhancement. *International Journal of Heat and Mass Transfer,* 122**,** 11-21.

Liu, X., Li, C., Cao, X., Yan, C. & Ding, M. 2018b. Numerical analysis on enhanced performance of new coaxial cross twisted tapes for laminar convective heat transfer. *International Journal of Heat and Mass Transfer,* 121**,** 1125-1136.

Lotfi, R., Saboohi, Y. & Rashidi, A. M. 2010. Numerical study of forced convective heat transfer of Nanofluids: Comparison of different approaches. *International Communications in Heat and Mass Transfer,* 37**,** 74-78.

Lu, G. & Zhai, X. 2019. Analysis on heat transfer and pressure drop of a microchannel heat sink with dimples and vortex generators. *International Journal of Thermal Sciences,* 145**,** 105986.

Manglik, R. M. & Bergles, A. E. 2003. Swirl flow heat transfer and pressure drop with twisted-tape inserts. *In:* Hartnett, J. P., Irvine, T. F., Cho, Y. I. & Greene, G. A. (eds.) *Advances in Heat Transfer.* Elsevier.

Manjrekar, O. N. & Dudukovic, M. P. 2019. Identification of flow regime in a bubble column reactor with a combination of optical probe data and machine learning technique. *Chemical Engineering Science: X,* 2**,** 100023.

Mashayekhi, R., Khodabandeh, E., Akbari, O. A., Toghraie, D., Bahiraei, M. & Gholami, M. 2018. CFD analysis of thermal and hydrodynamic characteristics of hybrid nanofluid in a new designed sinusoidal double-layered microchannel heat sink. *Journal of Thermal Analysis and Calorimetry,* 134**,** 2305-2315.

Mehendale, S. S., Jacobi, A. M. & Shah, R. K. 2000. Fluid flow and heat transfer at micro- and meso-scales with application to heat exchanger design. *Applied Mechanics Reviews,* 53**,** 175-193.

Mirmasoumi, S. & Behzadmehr, A. 2008. Effect of nanoparticles mean diameter on mixed convection heat transfer of a nanofluid in a horizontal tube. *International Journal of Heat and Fluid Flow,* 29**,** 557-566.

Mohammed Adham, A., Mohd-Ghazali, N. & Ahmad, R. 2013. Thermal and hydrodynamic analysis of microchannel heat sinks: A review. *Renewable and Sustainable Energy Reviews,* 21**,** 614-622.

Mohammed, H. A., Gunnasegaran, P. & Shuaib, N. H. 2011a. Influence of various base nanofluids and substrate materials on heat transfer in trapezoidal microchannel heat sinks. *International Communications in Heat and Mass Transfer,* 38**,** 194-201.

Mohammed, H. A., Gunnasegaran, P. & Shuaib, N. H. 2011b. Numerical simulation of heat transfer enhancement in wavy microchannel heat sink. *International Communications in Heat and Mass Transfer,* 38**,** 63-68.

Mohd-Ghazali, N., Estellé, P., Halelfadl, S., Maré, T., Siong, T. C. & Abidin, U. 2019. Thermal and hydrodynamic performance of a microchannel heat sink with carbon nanotube nanofluids. *Journal of Thermal Analysis and Calorimetry***,** 1-9.

Mojarrad, M. S., Keshavarz, A. & Shokouhi, A. 2013. Nanofluids thermal behavior analysis using a new dispersion model along with single-phase. *Heat and Mass Transfer,* 49**,** 1333-1343.

Mondal, M., Misra, R. P. & De, S. 2014. Combined electroosmotic and pressure driven flow in a microchannel at high zeta potential and overlapping electrical double layer. *International Journal of Thermal Sciences,* 86**,** 48-59.

Moraveji, M. K. & Ardehali, R. M. 2013. CFD modeling (comparing single and two-phase approaches) on thermal performance of Al_2O_3/water nanofluid in mini-channel heat sink. *International Communications in Heat and Mass Transfer,* 44**,** 157-164.

Murali Krishna, V., Sandeep Kumar, M., Mahesh, O. & Senthil Kumar, P. 2021. Numerical investigation of heat transfer and pressure drop for cooling of microchannel heat sink using MWCNT-CuO-Water hybrid nanofluid with different mixture ratio. *Materials Today: Proceedings,* 42**,** 969-974.

Naphon, P. & Nakharintr, L. 2015. Numerical Investigation of Laminar Heat Transfer of Nanofluid-Cooled Mini-Rectangular Fin Heat Sinks. *Journal of Engineering Physics and Thermophysics,* 88**,** 666-675.

Narendran, G., Gnanasekaran, N. & Perumal, D. A. 2020. Thermodynamic irreversibility and conjugate effects of integrated microchannel cooling device using TiO 2 nanofluid. *Heat and Mass Transfer,* 56**,** 489-505.

Narrein, K., Sivasankaran, S. & Ganesan, P. 2015. Two-Phase Analysis of A Helical Microchannel Heat Sink Using Nanofluids. *Numerical Heat Transfer, Part A: Applications,* 68**,** 1266-1279.

Naumann, Z. & Schiller, L. 1935. A drag coefficient correlation. *Zeitschrift des Vereins Deutscher Ingenieure,* 77**,** 393.

Nebbati, R. & Kadja, M. 2015. Study of forced convection of a nanofluid used as a heat carrier in a microchannel heat sink. *Energy Procedia,* 74**,** 633-642.

Pak, B. C. & Cho, Y. I. 1998. Hydrodynamic and heat transfer study of dispersed fluids with submicron metallic oxide particles. *Experimental Heat Transfer,* 11**,** 151-170.

Peng, X., Peterson, G. & Wang, B. 1994a. Heat transfer characteristics of water flowing through microchannels. *Experimental Heat Transfer An International Journal,* 7**,** 265-283.

Peng, X. F., Peterson, G. P. & Wang, B. X. 1994b. Heat transfer characteristics of water flowing through microchannels. *Experimental Heat Transfer,* 7**,** 265-283.

Phillips, R. J. 1990. Microchannel Heat Sinks. *The Lincoln Laboratory Journal,* 1**,** 31-48.

Ponnada, S., Subrahmanyam, T. & Naidu, S. V. 2019. A comparative study on the thermal performance of water in a circular tube with twisted tapes, perforated twisted tapes and perforated twisted tapes with alternate axis. *International Journal of Thermal Sciences,* 136**,** 530-538.

Radenac, E., Gressier, J. & Millan, P. 2014. Methodology of numerical coupling for transient conjugate heat transfer. *Computers & Fluids,* 100**,** 95-107.

Rahimi-Gorji, M., Pourmehran, O., Hatami, M. & Ganji, D. 2015. Statistical optimization of microchannel heat sink (MCHS) geometry cooled by different nanofluids using RSM analysis. *The European Physical Journal Plus,* 130.

Rashidi, S., Akar, S., Bovand, M. & Ellahi, R. 2018. Volume of fluid model to simulate the nanofluid flow and entropy generation in a single slope solar still. *Renewable Energy,* 115**,** 400-410.

Rogers, G. F. C. & Mayhew, Y. R. 1995. *Thermodynamic and transport properties of fluids*, John Wiley & Sons.

Saba, F., Ahmed, N., Khan, U., Waheed, A., Rafiq, M. & Mohyud-Din, S. T. 2018. Thermophysical analysis of water based ($Cu–Al_2O_3$) hybrid nanofluid in an asymmetric channel with dilating/squeezing walls considering different shapes of nanoparticles. *Applied Sciences,* 8.

Sabbaghzadeh, J. & Ebrahimi, S. 2007. Effective thermal conductivity of nanofluids containing cylindrical nanoparticles. *International Journal of Nanoscience,* 6**,** 45-49.

Sadique, H., Murtaza, Q. & Samsher 2022. Heat transfer augmentation in microchannel heat sink using secondary flows: A review. *International Journal of Heat and Mass Transfer,* 194**,** 123063.

Sahini, M., Chowdhury, U., Siddarth, A., Pradip, T., Agonafer, D., Zeigham, R., Metcalf, J. & Branton, S. Comparative study of high ambient inlet temperature effects on the performance of air vs. liquid cooled IT equipment. 2017 16th IEEE Intersociety Conference on Thermal and Thermomechanical Phenomena in Electronic Systems (ITherm), 2017. IEEE, 544-550.

Saidur, R., Leong, K. & Mohammad, H. 2011. A review on applications and challenges of nanofluids. *Renewable and sustainable energy reviews,* 15**,** 1646-1668.

Saini, A., Kaur, H., Sharma, S. & Gangacharyulu, D. 2016. Nanofluids: a review preparation, stability, properties and applications. *International Journal of Engineering Research and Technology,* 5**,** 11-16.

Sakanova, A., Keian, C. C. & Zhao, J. 2015. Performance improvements of microchannel heat sink using wavy channel and nanofluids. *International Journal of Heat and Mass Transfer,* 89**,** 59-74.

Santra, A. K., Sen, S. & Chakraborty, N. 2009. Study of heat transfer due to laminar flow of copper–water nanofluid through two isothermally heated parallel plates. *International Journal of Thermal Sciences,* 48**,** 391-400.

Sarlak, A., Ahmadpour, A. & Hajmohammadi, M. 2019. Thermal design improvement of a double-layered microchannel heat sink by using multi-walled carbon nanotube (MWCNT) nanofluids with non-Newtonian viscosity. *Applied Thermal Engineering,* 147**,** 205-215.

Seyf, H. R. & Keshavarz, M. S. 2011. Thermal and hydraulic performance of counterflow microchannel heat exchangers with and without nanofluids. *Journal of Heat Transfer,* 133.

Sharma, C. S., Tiwari, M. K., Michel, B. & Poulikakos, D. 2013. Thermofluidics and energetics of a manifold microchannel heat sink for electronics with recovered hot water as working fluid. *International Journal of Heat and Mass Transfer,* 58**,** 135-151.

Sheikhalipour, T. & Abbassi, A. 2016. Numerical investigation of nanofluid heat transfer inside trapezoidal microchannels using a novel dispersion model. *Advanced Powder Technology,* 27**,** 1464-1472.

Shi, X., Li, S., Wei, Y. & Gao, J. 2018. Numerical investigation of laminar convective heat transfer and pressure drop of water-based Al_2O_3 nanofluids in a microchannel. *International Communications in Heat and Mass Transfer,* 90**,** 111-120.

Sidik, N. A. C., Muhamad, M. N. A. W., Japar, W. M. A. A. & Rasid, Z. A. 2017. An overview of passive techniques for heat transfer augmentation in microchannel heat sink. *International Communications in Heat and Mass Transfer,* 88**,** 74-83.

Sidik, N. A. C., Yazid, M. N. A. W. M., Samion, S., Musa, M. N. & Mamat, R. 2016. Latest development on computational approaches for nanofluid flow modeling: Navier–Stokes based multiphase models. *International Communications in Heat and Mass Transfer,* 74**,** 114-124.

Silva, R., Garcia, F. A. P., Faia, P. M. & Rasteiro, M. G. 2015. Evaluating the Performance of the Mixture Model Coupled with High and Low Reynolds Turbulence Closures in the Numerical Description of Concentrated Solid-Liquid Flows of Settling Particles. *The Journal of Computational Multiphase Flows,* 7**,** 241-257.

Singh, V., Chamoli, S., Kumar, M. & Kumar, A. 2016. Heat transfer and fluid flow characteristics of heat exchanger tube with multiple twisted tapes and solid rings inserts. *Chemical Engineering and Processing: Process Intensification,* 102**,** 156-168.

Srivastava, P., Patel, R. I. & Dewan, A. 2021. A study on thermal characteristics of double-layered microchannel heat sink: Effects of bifurcation and flow configuration. *International Journal of Thermal Sciences,* 162.

Steinke, M. E. & Kandlikar, S. G. 2004. Review of single-phase heat transfer enhancement techniques for application in microchannels, minichannels and microdevices. *International Journal of Heat Technology,* 22**,** 3-11.

Steinke, M. E. & Kandlikar, S. G. 2006. Single-phase liquid friction factors in microchannels. *International Journal of Thermal Sciences,* 45**,** 1073-1083.

Sui, Y., Teo, C. J., Lee, P. S., Chew, Y. T. & Shu, C. 2010. Fluid flow and heat transfer in wavy microchannels. *International Journal of Heat and Mass Transfer,* 53**,** 2760-2772.

Sundar, L. S. & Sharma, K. 2010. Turbulent heat transfer and friction factor of Al2O3 nanofluid in circular tube with twisted tape inserts. *International Journal of Heat and Mass Transfer,* 53**,** 1409-1416.

Taliaferro, M. E., Angelino, M., Gori, F. & Goldstein, R. J. 2016. Local heat transfer on a finite width surface with laminar boundary layer flow. *Applied Thermal Engineering,* 101**,** 686-692.

Thomas, J., Srivatsa, P. V. S. S., Krishnan, S. R. & Baby, R. 2016. Thermal Performance Evaluation of a Phase Change Material Based Heat Sink: A Numerical Study. *Procedia Technology,* 25**,** 1182-1190.

Toghraie, D., Abdollah, M. M. D., Pourfattah, F., Akbari, O. A. & Ruhani, B. 2018. Numerical investigation of flow and heat transfer characteristics in smooth, sinusoidal and zigzag-shaped microchannel with and without nanofluid. *Journal of Thermal Analysis and Calorimetry,* 131**,** 1757-1766.

Tullius, J. F., Vajtai, R. & Bayazitoglu, Y. 2011. A review of cooling in microchannels. *Heat Transfer Engineering,* 32**,** 527-541.

Tunc, G. & Bayazitoglu, Y. 2002. Heat transfer in rectangular microchannels. *International Journal of Heat and Mass Transfer,* 45**,** 765-773.

Tusar, M., Ahmed, K., Bhuiya, M., Bhowmik, P., Rasul, M. & Ashwath, N. 2019. CFD study of heat transfer enhancement and fluid flow characteristics of laminar flow through tube with helical screw tape insert. *Energy Procedia,* 160**,** 699-706.

Vajjha, R. S., Das, D. K. & Kulkarni, D. P. 2010. Development of new correlations for convective heat transfer and friction factor in turbulent regime for nanofluids. *International Journal of Heat and Mass Transfer,* 53**,** 4607-4618.

Varun, Garg, M. O., Nautiyal, H., Khurana, S. & Shukla, M. K. 2016. Heat transfer augmentation using twisted tape inserts: A review. *Renewable and Sustainable Energy Reviews,* 63**,** 193-225.

Viceconti, M., Bellingeri, L., Cristofolini, L. & Toni, A. 1998. A comparative study on different methods of automatic mesh generation of human femurs. *Medical Engineering and Physics,* 20**,** 1-10.

Wang, G., Chen, T., Tian, M. & Ding, G. 2020. Fluid and heat transfer characteristics of microchannel heat sink with truncated rib on sidewall. *International Journal of Heat and Mass Transfer,* 148.

Wang, H., Chen, Z. & Gao, J. 2016. Influence of geometric parameters on flow and heat transfer performance of micro-channel heat sinks. *Applied Thermal Engineering,* 107**,** 870-879.

Wang, Z.-H., Wang, X.-D., Yan, W.-M., Duan, Y.-Y., Lee, D.-J. & Xu, J.-L. 2011. Multi-parameters optimization for microchannel heat sink using inverse problem method. *International Journal of Heat and Mass Transfer,* 54**,** 2811-2819.

Webb, R. L., Kim, N. J. T. & Francis, N. 2005. Enhanced heat transfer.

Wei, X. & Joshi, Y. 2003. Optimization study of stacked micro-channel heat sinks for micro-electronic cooling. *IEEE transactions on components and packaging technologies,* 26**,** 55-61.

Wongcharee, K. & Eiamsa-ard, S. 2012. Heat transfer enhancement by using CuO/water nanofluid in corrugated tube equipped with twisted tape. *International Communications in Heat and Mass Transfer,* 39**,** 251-257.

Wu, J. M. & Tao, W. Q. 2008. Numerical study on laminar convection heat transfer in a rectangular channel with longitudinal vortex generator. Part A: Verification of field synergy principle. *International Journal of Heat and Mass Transfer,* 51**,** 1179-1191.

Xia, G., Zhai, Y. & Cui, Z. 2013. Characteristics of entropy generation and heat transfer in a microchannel with fan-shaped reentrant cavities and internal ribs. *Science China Technological Sciences,* 56**,** 1629-1635.

Xie, G., Shen, H. & Wang, C.-C. 2015. Parametric study on thermal performance of microchannel heat sinks with internal vertical Y-shaped bifurcations. *International Journal of Heat and Mass Transfer,* 90**,** 948-958.

Xuan, Y. & Roetzel, W. 2000. Conceptions for heat transfer correlation of nanofluids. *International Journal of Heat and Mass Transfer,* 43**,** 3701-3707.

Yadav, R. & Padalkar, A. 2012. CFD analysis for heat transfer enhancement inside a circular tube with half-length upstream and half-length downstream twisted tape. *Journal of Thermodynamics,* 2012.

Yan, W.-T., Li, C. & Ye, W.-B. 2019. Numerical investigation of hydrodynamic and heat transfer performances of nanofluids in a fractal microchannel heat sink. *Heat Transfer-Asian Research,* 48**,** 2329-2349.

Yan, W.-T., Li, C., Ye, W.-B., Hong, Y. & Huang, S.-M. 2020. The effect of aspect ratio on hydraulic and heat transfer characteristics in a fractal microchannel. *International Journal of Fluid Mechanics Research,* 47**,** 71-84.

Yang, Y.-T., Tang, H.-W. & Ding, W.-P. 2016. Optimization design of micro-channel heat sink using nanofluid by numerical simulation coupled with genetic algorithm. *International Communications in Heat and Mass Transfer,* 72**,** 29-38.

Zhai, Y. L., Xia, G. D., Liu, X. F. & Li, Y. F. 2015. Exergy analysis and performance evaluation of flow and heat transfer in different micro heat sinks with complex structure. *International Journal of Heat and Mass Transfer,* 84**,** 293-303.

Zhimin, W. & Fah, C. K. The optimum thermal design of microchannel heat sinks. Proceedings of the 1997 1st Electronic Packaging Technology Conference (Cat. No.97TH8307), 10-10 Oct. 1997 1997. 123-129.

Zhuan, R. & Wang, W. 2013. Boiling heat transfer characteristics in a microchannel array heat sink with low mass flow rate. *Applied Thermal Engineering,* 51**,** 65-74.